A comparison of power harvesting techniques and related energy storage issues

by

Justin R. Farmer

Thesis Submitted to the Faculty of the
Virginia Polytechnic Institute and State University
in partial fulfillment of the requirements for the degree of

Master of Science

in

Mechanical Engineering

Dr. Daniel J. Inman, Chair
Dr. Donald J. Leo
Dr. Nakhiah Goulborne

May 15, 2007

Blacksburg, Virginia

Keywords: Power harvesting, piezoelectric, thermoelectric, active fiber composites

Copyright 2007, Justin R. Farmer

A comparison of power harvesting techniques and related energy storage issues

Justin R. Farmer

Abstract

Power harvesting, energy harvesting, power scavenging, and energy scavenging are four terms commonly used to describe the process of extracting useful electrical energy from other ambient energy sources using special materials called transducers that have the ability to convert one form of energy into another. While the words power and energy have vastly different definitions, the terms "power harvesting" and "energy harvesting" are used interchangeably throughout much of the literature to describe the same process of extracting electrical energy from ambient sources. Even though most of the energy coupling materials currently available have been around for decades, their use for the specific purpose of power harvesting has not been thoroughly examined until recently, when the power requirements of many electronic devices has reduced drastically.

The overall objective of this research is to typify the power source characteristics of various transducer devices in order to find some basic way to compare the relative energy densities of each type of device and, where possible, the comparative energy densities within subcategories of harvesting techniques. Included in this research is also a comparison of power storage techniques, which is often neglected in other literature sources.

An initial analysis of power storage devices explores the background of secondary (rechargeable) batteries and supercapacitors, the advantages and disadvantages of each, as well as the promising characteristics of recent supercapacitor technology developments. Also explored is research into the effectiveness of piezoelectric energy

harvesting for the purpose of battery charging, with particular focus on the current output of piezoelectric harvesters.

The first objective involved presenting and verifying a model for a cantilever piezoelectric bimorph. Next, an investigation into new active fiber composite materials and macro fiber composite devices utilizing the d_{31} coefficient is performed in comparison to a monolithic piezoelectric bimorph. The information gathered here was used to design a two bimorph device termed the mobile energy harvester (MEH). Worn by a human being at the waste level, the MEH harvests energy from each footfall during walking or running.

The next objective involved characterizing small temperature gradient (less than 200 ^{o}C) thermoelectric generators (TEGs). Four TEGs were linked in series and joined with a specially made aluminum base and fin heat sink. This device was then mounted to the exhaust system of an automobile and proved capable of recharging both an 80 and a 300 milliamp-hour battery. A switching circuit concept to step up the output voltage is also presented. However, the circuit proves somewhat difficult to implement, so an alternative DC/DC device is proposed as a possible solution. With the advent of highly efficient, low voltage DC to DC converters, it is shown that their high current, low voltage output can be converted to a higher voltage source that is suitable for many electronic and recharging applications.

As extensive literature exists on the capabilities of photovoltaic and electromagnetic energy harvesting, no original experimentation is presented. Instead, only a brief overview of the pertinent technological advances is provided in this document for the purpose of comparison to piezoelectric and thermoelectric energy harvesting. The main research focus, as described above, is dedicated to designing and performing original experiments to characterize cutting edge piezoelectric and thermoelectric transducer materials. To conclude and unify the document, the final section compares the power harvesting techniques with one another and introduces methods of combining them to produce a hybrid, multiple energy domain harvesting device. A piezoelectric-electromagnetic harvesting combination device is presented and scrutinized, revealing that such a device could improve the amount of energy extracted from a single harvesting unit.

The research presented here not only expands on the present understanding of these materials, but also proposes a new method of creating a hybrid power harvesting device utilizing two of the energy coupling domains, electromechanical and piezoelectric. The goal is to maximize the harvested energy by tapping into as many ambient sources as are available and practical.

Acknowledgments

First and foremost, this thesis would not be possible without the kindness and generosity of my advisor, Dr. Daniel J. Inman. He was very patient with me and allowed me to pursue my own theories through my experiments.

I would also like to thank Dr. Donald Leo and Dr. Nakhiah Goulbourne for agreeing to serve on my committee and analyze my findings.

A special thanks goes out to my family and friends, especially my mother and father, Bill and Rita Farmer. They have shown me the virtue of endurance in the face of extreme adversity. My father delayed his first bone marrow transplant in order to see me graduate with my bachelor's degree. I would also like to thank my brother Billy for making me look like the "good" son by comparison.

Also, I extend my gratitude to David Neal for showing me the meaning of perseverance and for teaching me the ideology that "if it doesn't work yet, you haven't spent enough money on it."

I would also like to thank all of the rest of my CIMSS colleagues. I would list them all and all that they have done for me, but that document would be longer than this thesis.

A special thanks for the support of the AFOSR MURI: Energy Harvesting and Storage System for Future AF Vehicles, grant number AFOSR F 9550-06-1-0326 monitored by Dr. B. Lee for helping to fund this research. Also, a special thanks to the National Science Foundation and the Goodson Professorship Endowment for helping to fund this research as well.

This thesis is also dedicated to all of those lives lost in the terrible tragedy that occurred at Virginia Tech on April 16th, 2007.

Table of Contents

1 Chapter 1 - Introduction 1

1.1 History of Power Harvesting 1

1.1.1 History of Piezoelectric Theory 1

1.1.2 History of Thermoelectric Theory 2

1.1.3 History of Photovoltaic Theory 3

1.1.4 History of Electromagnetic Theory 4

1.2 Literature Review 5

1.2.1 Vibration based harvesting 5

1.2.2 Thermal based harvesting 9

1.2.3 Solar based harvesting 11

2 Chapter 2 – Energy Harvesting Circuitry and Storage Devices .. 13

2.1 Energy Harvesting Electronic Circuitry 13

2.2 Current Battery Technology for Energy Storage 17

2.2.1 Basic Battery Theory 17

2.2.2 Rechargeable Nickel Metal Hydride 17

2.2.3 Rechargeable Lithium-based 18

2.2.4 Rechargeable Thin Film Lithium Ion 19

2.3 Current Capacitor Technology for Energy Storage 20

2.3.1 Electrolytic capacitors 20

2.3.2 Supercapacitors 21

2.4 Comparison of Energy Storage Methods 23

2.4.1 Batteries versus Supercapacitors - Energy versus Power Density 23

2.4.2 Batteries versus Supercapacitors - Piezoelectric Energy Storage 25

3 Chapter 3 - Piezoelectric Generators 31

3.1 Electrical Modeling of Piezoelectric Materials 31

3.2 Piezo Systems Bimorph Modeling and Characterization 32

3.2.1 Bimorph Modeling 32

3.2.2 Experimental Verification 36
3.2.3 Power Generation Setup and Bimorph Characterization 40
3.3 Active Fiber Composite Bimorph Modeling and Characterization 44
3.3.1 Battery Charging using Active Fiber Composite Bimorph 45
3.3.2 Active Fiber Composite and Piezo Systems Comparison 48
3.4 Macro Fiber Composite Harvesting 50
3.5 Multiple Bimorph Harvesting System 54
3.5.1 Mobile Harvesting - Motivation 55
3.5.2 Mobile Energy Harvester Theory and Construction 56
3.5.3 Battery Recharging Experimentation 58
3.5.4 Capacitor Charging Experimentation 60
3.5.5 Conclusions and Future Work 64

4 Chapter 4 – Thermoelectric Generators 65
4.1 Electrical Modeling of Thermoelectric Materials 65
4.2 Battery Recharging Using Ambient Thermal Gradients from Automotive Exhaust 66
4.2.1 Thermoelectric Generator Device Characterization 67
4.2.2 Automotive Harvesting Experimentation 69
4.3 Innovative Charging Circuit Using Electronic Switches 72
4.4 Low Power DC/DC Converter for Thermoelectric Charging of Lithium Ion Batteries 74
4.5 Switching Circuit versus DC/DC Converter Comparison 78

5 Chapter 5 – Hybrid Generator Concept 79
5.1 Electrical Modeling of Photovoltaic Materials 79
5.2 Electrical Modeling of Electromagnetic Generator 80
5.3 Comparison of Harvesting Techniques 81
5.4 Piezoelectric and Electromagnetic Hybrid Generator 82

6 Chapter 6 – Conclusions 85
6.1 Brief Summary of Thesis 85
6.2 Contributions 87

6.3 Future Work 89

7 Bibliography 91

8 Vita 101

List of Figures

Figure 2.1.1. Simple model of a piezoelectric generator. 14
Figure 2.1.2. Voltage output after signal is sent through a full bridge diode rectifier. 14
Figure 2.1.3. Additional capacitor to produce an almost-DC voltage output. 15
Figure 2.1.4. Plot of time to charge a capacitor to 5 volts as a function of capacitance and current. 16
Figure 2.3.1. Schematic of realistic capacitor model incorporating ESR. 21
Figure 2.3.2. Plot of voltage of each capacitor with no load (overlapped). 22
Figure 2.4.1. Discharge curves of two capacitors and a battery across an 80 ohm resistor. 24
Figure 2.4.2. Charge curves for capacitors and a battery from ambient vibration energy. 26
Figure 2.4.3. Discharge curves of capacitors and a battery across a 462 ohm load. 27
Figure 2.4.4. Plot of 20 mAh NiMH battery charging curves. 28
Figure 2.4.5. Reference plot of discharge curve across 150 ohm resistor. 29
Figure 3.1.1. Model of piezoceramic as a sinusoidal voltage source in series with 32
Figure 3.2.1. Cantilever beam with added tip mass. 33
Figure 3.2.2. Layers representing a piezoelectric bimorph. 34
Figure 3.2.3. Tip mass effect on natural frequency of a cantilever configuration. 36
Figure 3.2.4. Photograph of test setup for Piezo Systems bimorph experiments. 37
Figure 3.2.5. Plot of voltage decay of open circuit piezoelectric configuration. 38
Figure 3.2.6. Plot of tip displacement measured by laser vibrometer. 38
Figure 3.2.7. Photograph of multiple bimorph testing setup and equipment. 41
Figure 3.2.8. Photograph of test setup with Kistler teardrop accelerometer secured to the base. 42
Figure 3.2.9. Plot of peak to peak voltage as a function of base acceleration. 42
Figure 3.2.10. Plot of power curves for a 4.7 and 10 μF capacitor and various resistor values. 44

Figure 3.3.1. Photograph of bimorph sample in its protective plastic case. 45
Figure 3.3.2. Photograph of AFC attached to the shaker, vibrating at its first natural frequency. 46
Figure 3.3.3. Voltage, current, and power output from Siglab sine sweep testing. 47
Figure 3.3.4. Plot of a 40 mAh and an 80 mAh battery 48
Figure 3.3.5. Photograph of test mount for AFC and PS monolithic bimorphs. 49
Figure 3.3.6. Capacitor voltage plots for AFC and PS bimorphs for various input frequencies. 50
Figure 3.4.1. Photograph of MFC bimorph constructed in the laboratory. 51
Figure 3.4.2. Power curves for monolithic and macro fiber composite bimorphs versus resistance. 52
Figure 3.4.3. Photograph of AFC, PS, and MFC bimorphs mounted to an electrodynamic shaker. 53
Figure 3.4.4. Plots of energy stored in 100 μF capacitors using AFC, MFC, and PS bimorphs at three different input frequencies. 54
Figure 3.5.1. Photographs of experimental MEH unit and test subject. 58
Figure 3.5.2. Photograph of Li-ion battery next to a dime for size comparison. 58
Figure 3.5.3. Charge and discharge curves for each battery during experimentation. 59
Figure 3.5.4. Diagram of experimental setup for mobile energy harvester. 61
Figure 3.5.5. Plots of voltage and stored energy, respectively, for six different capacitors. 62
Figure 3.5.6. Plots of rate of energy storage (power) in various capacitor sizes versus time. 62
Figure 3.5.7. Plots of voltage decay after charging source has been removed. 63
Figure 4.1.1. Electrical equivalent model of a thermoelectric generator device. 65
Figure 4.1.2. Schematic of ideal Peltier device (adapted from [64].) 66
Figure 4.2.1. Photograph of automobile and mounting location of TEG device. 67
Figure 4.2.2. Plot of ΔT on left y-axis and plot of TEG voltage on right y-axis versus time. 68
Figure 4.2.3. Plot of TEG output voltage as a function of ΔT. 69

Figure 4.2.4. AutoCAD drawing of the thermoelectric generator device, including heat sink and aluminum piece to adapt to vehicle exhaust system. 70
Figure 4.2.5. Plot of the TEG voltage, current, and power output versus time 71
Figure 4.2.6. Voltage versus time for 80 and 300 mAh NiMH batteries charged using TEG device. 72
Figure 4.3.1. Electrical Schematic of switching circuit. 73
Figure 4.3.2. Photograph of switching circuit. 74
Figure 4.4.1. Photograph of LM2621 evaluation board. 75
Figure 4.4.2. Plot of input and output voltages of DC/DC converter test board. 76
Figure 4.4.3. Plot of input and output voltages of DC/DC converter and ΔT of TEG device. 77
Figure 4.4.4. Plot of capacitor voltage and ΔT for charging using the TEG 77
Figure 5.1.1. Electrical model of a solar cell as a current source in parallel with a diode 80
Figure 5.2.1. Electrical Schematic of electromagnetic generator attached to a load. 81
Figure 5.4.1. Photograph of electromagnetic-piezoelectric harvester hybrid test setup. 83
Figure 5.4.2. Plot of power output versus electromagnetic load resistance for both harvesting techniques. 84

List of Tables

Table 2.4.1. Summary of discharge characteristics. 26
Table 3.2.1. Properties of Piezo Systems, Inc. T226-A4-503X bimorph. 35
Table 3.2.2. First resonant frequency for normalized tip mass values. 36
Table 3.2.3. Experimental values obtained for no tip mass and a 4.8 gram tip mass. 39
Table 3.2.4. Summary of calculated variables for bimorph testing. 40
Table 3.5.1. Capacitance values used for MEH testing. 60
Table 5.3.1. Comparison of power density based on experimentation. 81

Nomenclature

A	=	surface area
B	=	magnetic flux density
b	=	distance, Chapter 3.2
c	=	damping
C	=	capacitance
C	=	battery capacity
D	=	distance, Chapter 2
D	=	electric displacement, Chapter 3
E	=	electric field, Chapter 3.1
E	=	modulus of elasticity, Chapter 3.2
ESR	=	equivalent series resistance
F	=	Faraday constant, Chapter 2
F	=	force
f_r	=	first natural frequency
i or I	=	current, Chapter 2
I	=	moment of inertia, Chapter 3.2
j	=	imaginary component
J	=	current density
k	=	spring constant
l or L	=	length, Chapter 3.2
L	=	coil length, Chapter 5
M	=	mass
n	=	integer number
P	=	power
R	=	resistance
S	=	strain, Chapter 3
t	=	time, Chapter 2
t	=	thickness, Chapter 3.2
T	=	period, Chapter 2
T	=	mechanical stress, Chapter 3
v or V	=	voltage
w	=	width
x	=	position
y or Y	=	position, Chapter 5
z or Z	=	position, Chapter 5
Z	=	impedance

α = Seebeck coefficient
δ = logarithmic decrement
ε = dielectric constant
ε_o = permittivity of free space
ε_r = relative permittivity
η = ratio, Chapter 3.2
μ = chemical potential, Chapter 2
ρ = density, Chapter 3
ρ = electrical resistivity, Chapter 4
ω = frequency
ζ = damping ratio
θ = phase
ϕ = transformation factor

Subscript

b = beam, Chapter 3.2
c = piezoceramic, Chapter 3.2
e = electrical, Chapter 5
L = load
Li = lithium
m = mechanical, Chapter 5
r = ripple, Chapter 2
sc = short circuit
sh = shim
T = total
TEG = thermoelectric generator

Chapter 1 - Introduction

1.1 History of Power Harvesting

1.1.1 History of Piezoelectric Theory

In 1880, Pierre and Jacques Curie successfully predicted and proved experimentally that certain crystals, most notably Rochelle salt and quartz, would exhibit a surface charge when subject to mechanical stress. This phenomenon was given the name *piezoelectricity*, which is derived from the Greek *piezo*, meaning "to press or squeeze". Specifically, this application is termed the direct piezoelectric effect. One year later, the converse piezoelectric effect, by which certain materials deform when subjected to an electric field, was deduced mathematically by Lippmann and soon confirmed experimentally by the Curie brothers [75].

Outside of France, other prominent physicist such at Rontgen, Kundt, Voigt, and Riecke soon began their own investigations into piezoelectricity. However, it was not until over 30 years later that Langevin came up with the idea of echo sounding using the converse piezoelectric effect in 1924, bringing piezoelectric materials out of the realm of scientific curiosity. Soon after World War I, the direct piezoelectric began to be exploited for sensor and transducer applications. In Japan, Okichi et al 1925 was the first to succeed in measuring the cylinder pressure in an internal combustion engine with a quartz pressure sensor. In 1927, he published the first force measurements made with quartz force sensors [31]. In America, Cady, first attracted by the attempts to generate ultrasound waves, dedicated his entire life to the study of piezoelectricity, publishing all his results in 1964 and earning the title "father of modern piezoelectricity" [31]. Europe and USA in the 1940s after World War I and Japan and China in the 1970s began manufacturing piezoelectric sensors, and the piezoelectric measuring principle quickly gained popularity in practical applications worldwide [31]. The most recent developments of piezoelectric theory over the past decade as they relate to power harvesting are presented in the following literature review section.

1.1.2 History of Thermoelectric Theory

In 1826, Thomas Johann Seebeck first observed the thermoelectricity phenomenon. He found that a current would flow in a closed circuit made of two dissimilar metals when they are maintained at different temperatures [11]. For the following three decades, the basic thermoelectric effects were explored and understood macroscopically, and their applicability to thermometry, power generation, and refrigeration was recognized [55].

In the 1930s and the following decades, a microscopic understanding of thermoelectricity led to the development of more sophisticated materials, many of which are still in use today. Additionally, the figure of merit of these materials began to steadily increase, though the advancements began to wane by the 1970s [55]. Beginning in the early 1970s, a need for a low power, long-lasting battery sparked interest in thermoelectric materials for power harvesting in the commercial sector. Radioactive materials were utilized as a heat source and generators were developed by arranging thermocouples in a monolithic structure for useful power generation [64]. Most notably, this method was used for power generation for remote deep space applications.

Once again, beginning around 1990, a combination of factors such as an interest in cooling electronics and environmental concerns involving refrigerants led to renewed interest in alternative refrigeration technologies. Thermoelectric cooling, a well established technology, saw new research and advancements thanks to the renewed interest [55]. Research has focused on making smaller, more efficient and more powerful thermoelectric generators. The most recent developments pertaining to thermoelectric power harvesting are saved for the literature review section.

1.1.3 History of Photovoltaic Theory

In 1839, as he was experimenting with an electrolytic cell composed of two metal electrodes, Edmund Becquerel discovered the photovoltaic effect [48]. In 1876, William Adams and Richard Day found that a sample of selenium contacted by two heated platinum contact could produce a photo current. The first large area solar cell was constructed by Charles Fritts in 1894 who coated a layer of selenium with a thin layer of gold [19].

While the photovoltaic effect was first observed by Edmund Becquerel, it was not until the development of the quantum theory of light and solid state physics in the early 1900s that it became fully comprehensible [48]. In 1914, Goldman and Brodsky related the photovoltaic effect to the existence of a barrier to current flow at one of the semiconductor-metal interfaces. During the 1930s, researchers such as Walter Shottky, Neville Mott, and others developed the theory of metal-semiconductor barrier layers [52].

In 1954, Chapin, Fuller, and Pearson reported the first silicon solar cell with a 6% efficiency, six times greater than any previous devices. High production costs of such cells limited their use to space applications, where issues of reliability and low weight made such expense justifiable. Simultaneously, in 1954, cadmium sulfide p-n junctions were introduced that also demonstrated a 6% efficiency. Furthermore, theoretical calculations showed that such materials would ultimately yield higher efficiencies than their silicon counterparts, stimulating investigation into p-n junction devices of gallium arsenide, indium phosphide, and cadmium telluride. Despite such evidence, silicon still remains the foremost photovoltaic material, benefiting from advances of silicon technologies funded by the microelectronics industry research [52].

Coinciding with the deregulation of electricity markets in the early 1990s, the interest in photovoltaics expanded and pricing has come down to a competitive level for remote power supply systems [52]. As of 1996, photovoltaics had become a $131 million dollar market [48].

1.1.4 History of Electromagnetic Theory

In 1820, Hans Oersted was performing a demonstration on the heating effects of electric current and noticed that a nearby compass needle deflected when current was flowing through his circuit. He had no explanation for the phenomenon, but continued to experiment with it [50].

The natural question following this discovery was whether electricity could be produced from magnetism. Joseph Henry and Michael Faraday independently discovered this principle, known as electromagnetic induction, in 1831 [50]. In August of 1831, Faraday discovered experimentally that a changing magnetic field would induce an electric field. In October of the same year, he invented the first direct-current generator consisting of a copper plate rotating between magnetic poles [29]. His findings on electromagnetism are presented in three volumes published between 1839 and 1855 entitled *Experimental Researches on Electricity* [50].

Between 1864 and 1873, heavily influenced by Faraday's work, James Clerk Maxwell built on Faraday's findings and derived a series of mathematical equations to explain Faraday's lines of force and the natural behavior of electric and magnetic fields. In 1888, Heinrich Hertz experimentally verified Maxwell's work and laid the groundwork for the transmission of radio waves [50]. In 1905, Albert Einstein analyzed the photoelectric effect phenomena and put forth the theory that light might be made up of vast amounts of packets of electromagnetic radiation in discrete units. Additionally, he theorizes that there was a particular constant c, representing the speed of light, faster than which no particle or wave could travel.

While much research has been performed in the hundred years since these discoveries, summarizing all of these accomplishments would be a daunting task and exceeds the scope of the proposed research. The basic foundations summarized in this section are sufficient to provide an understanding of the electromagnetic phenomena and the methods available to exploit it for energy harvesting purposes.

1.2 Literature Review

While there are four main methods for energy harvesting (piezoelectric, thermoelectric, photovoltaic, electromagnetic), the literature review is divided into three main sections to reflect the source of the ambient energy: vibration, thermal, and solar.

Over the past decade, the amount of literature published on the topic of energy harvesting has increased drastically due to renewed interest in alternative energy sources. Therefore, only the literature that is relevant to the research performed in this thesis is presented in an effort to limit the scope of the literature search.

1.2.1 Vibration based harvesting

Hausler and Stein (1984) presented one of the earliest documented experiments of power harvesting using piezoelectric materials involved a PVDF film inserted into the rib cage of a mongrel dog. The concept was to use this power for medical applications, and it was predicted that the device could generate power on the order of 1 mW. However, a mechanical simulation of the dog's ribs provided only 20 μW, and the actual experiment only provided 17 μW at a peak voltage of 18 V [35].

Schmidt et al. (1992) investigated the feasibility of using PVDF film in compression to harvest power from a windmill. A piezoelectric approach was developed because the large high-speed rotor used for conventional generators poses a serious safety problem to people nearby. He predicted an output on the order of 100 watts per cubic centimeter, but the material costs still outweigh the perceived benefits and his proposed device has yet to be constructed [66].

Starner et al. (1996) revisited the idea of harvesting energy from a living creature, specifically a human being. He performed some theoretical calculations on the amount of power that might be generated from a device that harvested power from body heat, respiration, or blood pressure. His conclusion was that harvesting energy from human walking would be the most practical and least intrusive method [75].

Williams and Yates (1996) derived the equations of motion for a nonspecific generator that consisted of a seismic mass on a spring and a damper. The power output

was derived from the energy that could be dissipated through the damper by converting mechanical to electrical energy. Based on the derived equations, the power output of such a generator is proportional to the cube of the vibration frequency and that the deflection of the seismic mass should be as large as possible. The proposed harvesting system utilized an electromagnetic harvesting scheme. For a very small (5 mm x 5 mm x 1 mm) generator, they predicted 1 μW at an excitation frequency of 70 Hz and 0.1 mW at 330 Hz [87].

Umeda et al (1996) proposed using a piezoelectric transducer to transform mechanical impact energy of a falling steel ball into electric energy. The equivalent model led to the conclusions that an optimum value existed for the load resistance, and that most of the mechanical impact energy would be transferred to the steel ball after the bounce as kinetic energy [82].

The following year, Umeda et al (1997) presented the results of a prototype generator based on the concept of their earlier work. The effects of the size of the storage capacitor were examined. Under high initial voltage conditions where the capacitor was pre-charged to a voltage higher than 5V, a maximum efficiency of 35% was achieved with efficiency of over 25% for each capacitance tested [83].

In 1998, Kimura obtained a patent for a piezo-electricity generation device without an external power supply that accumulated electric charge after rectifying the AC voltage generated. The source of voltage was specified to be at least one free-vibrating piezo-electric plate [41].

Kymissis et al (1998) researched the concept of using PDVF and piezoceramics as well as rotary magnetic generators to harvest energy inside of a shoe. The PZT and PVDF integrated smoothly with a running sneaker, but the magnetic generator was too bulky and obtrusive for practical use. Overall, his group measured roughly 1 milliJoule (mJ) per step for a PVDF and 2 mJ per step for a PZT unimorph device [43].

Goldfarb and Jones (1999) investigated the efficiency of generating power with piezoceramics, specifically a PZT stack. They determined that the maximum efficiency point was several orders of magnitude smaller than the structural resonance of the stack. Additionally, the stack had poor efficiency because most of the power generated was absorbed back into other layers of the structure [32].

Jansen and Stevels (1999) looked at the possibility of human power being a viable alternative to batteries for portable consumer products. Citing the decreasing power consumption of portable electronic devices, they examine the various forms of human activities and processes such as pushing a button or squeezing a hand to generate enough electrical energy to replace batteries in some applications. The benefits of such technology to the environment in contrast to batteries are also mentioned [38].

Allen and Smits (2000) looked at harvesting energy using the Karman vortex behind a bluff body from induced oscillations of a piezoelectric membrane. Four different membranes or "eels" were tested in the vortex street, and their behavior was successfully predicted by derived models. However, since this was only a feasibility study, no actual numbers were presented in terms of the amount of energy that could be harvested [9].

Ramsay and Clark (2001) investigated the feasibility of using piezoelectric material as a power supply for an *in vivo* MEMS application. A square PZT-5A thin plate was driven by a fluctuating pressure source designed to simulate blood pressure. The conclusion was that, with an effective surface area of 1 cm^2, a piezoelectric generator may be able to power a μW device continuously and a mW device intermittently [58].

Elvin et al (2001) researched a strain sensor that could simultaneously for power harvesting and sensing. For verification, a PVDF film was attached to a beam for a four-point bending test. The power generated was enough to broadcast a wireless signal 2 meters in a laboratory setting. The response of the sensor turned out to be dependent on both the frequency and the applied load, though the sensor successfully measured as low as 60 με [28].

Meninger et al (2001) proposed the use of a MEMS-scale variable capacitor transducer to convert mechanical vibrations into electrical energy for low power electronics. Two possible methods of harvesting are discussed, the first being a voltage constrained cycle and the second being a charge constrained cycle. From basic calculations, it is evident that the voltage constrained case can extract more energy. A MEMS scale device designed to vibrate at 2520 Hz is predicted to generate 8.6 μW of power [49].

Sterken (2002) analyzed a similar method of charge transportation between two parallel capacitors as a means of converting mechanical to electrical energy. Using a MEMS-based device, the author claims 100 μW of electrical power from a device displacement of only 20 μm operating at 1200 Hz [79].

Ottman et al (2002) presented a method of optimizing the energy harvested from a vibrating piezoelectric device using a step-down DC-DC converter. The authors derived and confirmed that, as the magnitude of the excitation increases, the optimal duty cycle is essentially constant. At lower excitations, the circuit was designed to bypass the step-down converter circuitry and charge the battery directly using the rectified piezoelectric signal. An optimal duty cycle of 2.8% for their step-down converter was derived and they were able to harvest energy at levels 325% higher than the rate of direct charging of a battery. The maximum amount of energy harvested was claimed to be 30.66 mW [57].

Sodano et al (2003) investigated the possibility of using piezoelectric generators to recharge nickel metal hydride batteries. Two types of harvesters, a monolithic piezoelectric (PZT) and a Macro Fiber Composite (MFC), were used for the experiment. While the MFC is much more flexible than the PZT, the use of interdigitated electrodes in the MFC limits the amount of current produced, and hence hinders its capabilities as a power harvesting device for charging batteries, except when relatively large disturbances are available. The PZT, however, was able to charge 40 mAh and 80 mAh batteries within two hours. It was also shown that charging a battery by vibrating the PZT at resonance typically took less time than by using a random input signal to the PZT [72].

As stated previously, the amount of research in this field, especially vibration based energy harvesting, has increased exponentially over the past several years. For a more comprehensive summary of the literature published on energy harvesting between 1984 and 2003, the reader is referred to the review article published by Sodano et al [67]. Furthermore, for literature published between 2003 to the present, the reader is referred to the paper by Anton and Sodano (2007), who performed a very extensive literature review of research published in the past few years [10].

1.2.2 Thermal based harvesting

Kiely et al (1991) utilized silicon integrated circuit technology to fabricate a thermoelectric generator consisting of heavily implanted polycrystalline thermoelements on a quartz substrate. The generator had improved substrate qualities which allowed for better operation than previous designs. Additionally, the production costs of the device were lower than previous generators [40].

Wu et al (1996) proposed the concept of a waste-heat thermoelectric generator. Wu presented a realistic waste-heat thermoelectric generator model that accounted for both internal and external irreversibility effects. External irreversibility was attributable to temperature differences between the hot and cold junctions and the heat source and sink. Internal irreversibility was attributable to Joulean loss and heat conduction. The conclusion was that the economic competitiveness of such a technology in the commercial market depended on development of new thermoelectric materials and power module designs [88].

Stordeur et al (1997) developed a low power thermoelectric generator capable of generating tens of microwatts of power out of a device that had previously generated nanowatts out of the same device size. The device was based on thin film thermoelectric materials, consisted of 2250 thermocouples, and operated in temperatures ranging from room to not higher than 120 ^{o}C [80].

Damaschke (1997) analyzed the need for a self starting dc-dc converter that was optimized for very-low-input voltages below 300 mV, such as those provided by thermoelectric generators. Such a device would be capable of operating from a TEG supply at temperature differences of 20 ^{o}C and smaller and provide a stabilized output voltage of 5 volts. The main difficulty was in devising a starter circuit to provide enough voltage to initialize the converter. This special circuit would cease to receive power once the DC/DC converter was operating. A prototype was constructed and connected to a bismuth telluride TEG power supply with $\Delta T = 20\ ^{o}C$. The device provides a reasonably stable output voltage of 5 volts for up to a 131-mW load, which was 76% of the maximum available power and an excellent result for such low power levels [18].

A few years later, Stark and Stordeur (1999) presented findings on new thin film micro thermoelectric devices based on bismuth telluride. They suggested that the power input could be increased by using present technology to decrease the substrate thickness and raising the film thickness. Additionally, the technology and materials allowed for the production of a high-sensitivity infrared sensor [74].

Zhang et al (2001) proposed and constructed a micromachined TEG with a built in catalytic combustion chamber. Measuring only 2 mm x 8 mm x 0.5 mm, the combustion chamber ignited hydrogen and air and provided output power of up to ~1 μW per thermocouple. Polysilicon-Pt thermopiles were used to withstand high combustion temperatures of up to 964 ^{o}C. If slight geometric modifications were performed with temperature differences of ~800K provided by the combustion chamber, the proposed power output could be up to 10 μW per thermocouple could be achieved [90].

Douseki et al (2003) combined a specially designed DC-DC converter and a thermoelectric generator module to broadcast a short-range wireless signal. The DC-DC converter was unique in that is used a switched-capacitor design to handle power supplied by the thermoelectric generator of either polarity to produce an always positive power output. The device is shown to operate from either the heat source of a warm hand or the heat sink provided by a vessel of cold water [23].

Nolas et al (2006) investigated the recent development in bulk thermoelectric materials. Special materials such as skutterudites, clathrates, Half-Heusler intermetallic alloys, and several others are investigated for their low thermal conductivity properties. The authors emphasize the need for a better understanding of thermal transport in such materials to improve thermoelectric performance. The conclusion is that the phonon-glass/electron-crystal approach, although not a novel one continues to rank highest in terms of high performance thermoelectric materials [54].

Yang and Caillat (2006) looked at thermoelectric waste-heat recovery devices for use in the automotive industry. The motivation for the research was that only 25% of the combustion energy is actually used in an automobile, while up to 40% is lost to exhaust gases as waste. They begin by analyzing the existing technology called radioisotope thermoelectric generators that had been designed in earlier decades for space vehicle applications. Specifically, the areas of device degradation over time and optimization of

the figure of merit of thermoelectric devices within the specified operating temperature range are considered. The proposed benefits to automotive thermoelectric generation include eliminating secondary loads from the engine drive train and solid state, reliable and reversible air conditioning systems free from refrigerants. Challenges to such technology include difficulty of integrating with existing automotive electrical power systems and optimal operation over a broad range of temperatures [13].

Sodano et al (2007) proposed a novel approach to thermal harvesting using a small greenhouse device to capture thermal energy from solar radiation. The greenhouse was used in conjunction with a solar concentrator and a black body heat sink to harvest energy to recharge small nickel metal hydride batteries. The device was capable of recharging an 80 mAh and a 300 mAh nickel metal hydride battery in under 4 and 18 minutes, respectively. The study demonstrated that with relatively small thermal gradients and only conductive heat transfer, a thermoelectric generator can be used for energy harvesting applications [71].

1.2.3 Solar based harvesting

Lee et al (1995) designed a hydrogenated amorphous silicon solar sell array as an on-board power source for electrostatic MEMS. From an array area of 1 cm^2, they were able to produce 150 V open circuit and 2.8 μA short circuit under standard solar cell test light intensity conditions. The device claims to be useful for any small device requiring voltages from tens to 100 V with currents in the nA to μA range [45].

Catchpole and Green (2002) discussed the need of a third-generation of high efficiency solar cells with energy conversion efficiencies of double or triple the targeted 15-20%. While second generation devices were presently being researched, their material costs were predicted to dominate, and the efficiency of conventional solar cells was only 40.7%. Approaches such as tandem cells, hot carrier, multiple level approaches, thermophotovoltaics and thermophotonics are suggested with high theoretical efficiencies of up to 86.8% efficiency [15].

Voigt et al (2003) evaluate two protocols to perform solar-aware routing in wireless sensors. The goal is to increase efficiency and reduce overall battery consumption. With 64 nodes, solar-aware routing was 15.1% better than shortest-path routing, while with 96 nodes, the improvement was only 12.1%. The results demonstrated that their first protocol was more suitable for small networks, while the second protocol was more suitable for larger networks. Future work includes conducting real live experiments once the hardware and sensor boards were ready [84].

Chou et al (2004) proposed a source-tracking power management system to maximize the panel's total energy output by load matching. As the internal resistance of a solar cell is not constant, Chou first varies the load resistance and measures the source voltage at different light intensities to characterize the cell. Knowing the ambient sunlight intensity, the designed system uses a light sensor to dynamically adjust the load to match the maximum power available. The results show that over 132% of useable power can be reclaimed using such strategies [16].

Raghunathan et al (2005) investigated the challenges of solar energy harvesting designs for wireless systems. While solar harvesting has the highest power density of all harvesting techniques, it is highly dependent upon the intensity and duration of the energy source available. Energy storage techniques are also discusses, with the tradeoffs of each type analyzed in comparison to the others. A specially built device called a Heliomote was examined and designed to perform specific energy storage, power routing, and harvesting aware algorithms which provide self-sustained near-perpetual operation from two solar cells and two NiMH batteries [59].

Chapter 2 – Energy Harvesting Circuitry and Storage Devices

2.1 Energy Harvesting Electronic Circuitry

This section presents the electronic components involved in capturing the energy harvested by various transducers. Specifically, piezoelectric harvesting is of greatest interest, and therefore will be used as the foundation of understanding the electronic circuitry involved in energy harvesting. Only passive circuitry is discussed in this section. While active components are an area of ongoing research, they are not presented here. The energy required to operate such components is greater than that which can be supplied by power harvesting alone.

In its very simplest form, a piezoelectric or electromagnetic generator is modeled as an AC voltage source as shown in Figure 2.1.1. However, this output is not useful for most electronic applications. The generator is first connected to a full bridge rectifier, which consists of four standard diodes connected in such a way that the voltage reaching the load is always positive, as shown in the graph in Figure 2.1.2. Thermoelectric and photovoltaic generators typically do not require such rectification, since their output is fairly DC or at least always positive.

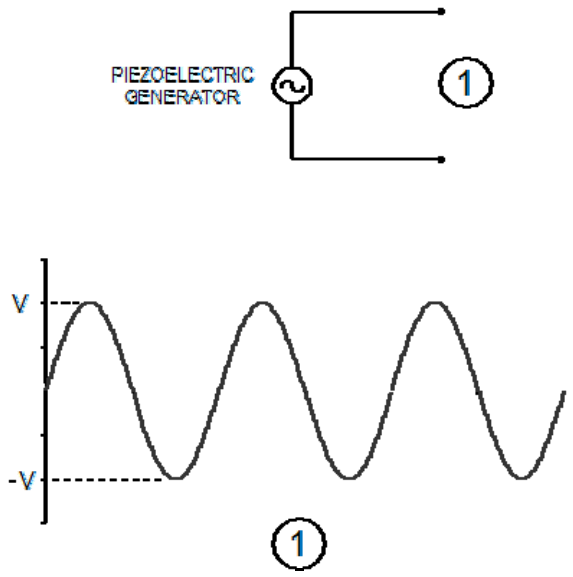

Figure 2.1.1. Simple model of a piezoelectric generator.

In the ideal-diode model, the device acts as a perfect conductor with no voltage drop in the forward direction and acts as an open circuit in the reverse direction. For a real diode, the output voltage is less than the input voltage due to a drop across the diode, typically 0.7 V for silicon diodes at room temperature [34].

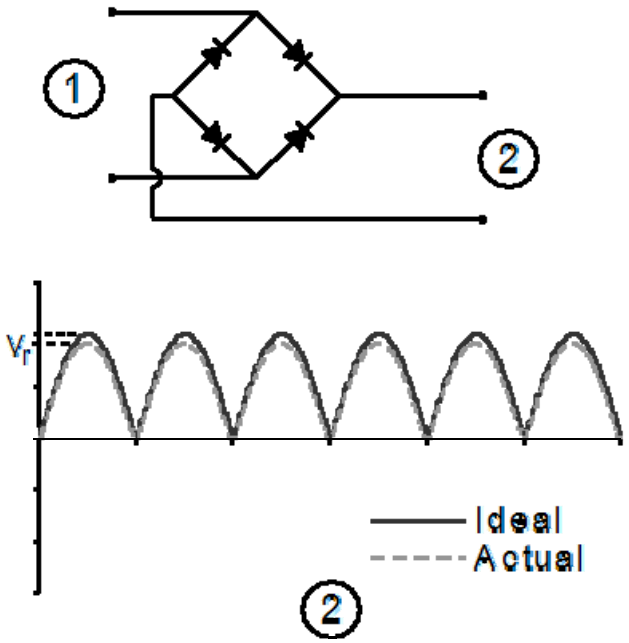

Figure 2.1.2. Voltage output after signal is sent through a full bridge diode rectifier.

In order to provide a relatively stable voltage for electronics, a capacitor is added to the output terminals of the bridge rectifier. If it is small enough, the capacitor is charged up to the first peak of the voltage input. The relationship between the current and voltage in a capacitor can be given by

$$i(t) = C\frac{dv(t)}{dt} \qquad \textbf{2.1.1}$$

so the current is related to the change in voltage and the storage capacity of a capacitor [60].

Once the input voltage drops below the voltage stored in the capacitor, the capacitor slowly discharges until the next peak of the input. As a general rule, the size of the capacitor required to smooth the voltage is

$$C = \frac{I_L T}{2V_r} \qquad \textbf{2.1.2}$$

where I_L is the average load current, T is the period of the bridge input voltage, and V_r is the peak-to-peak ripple voltage [34].

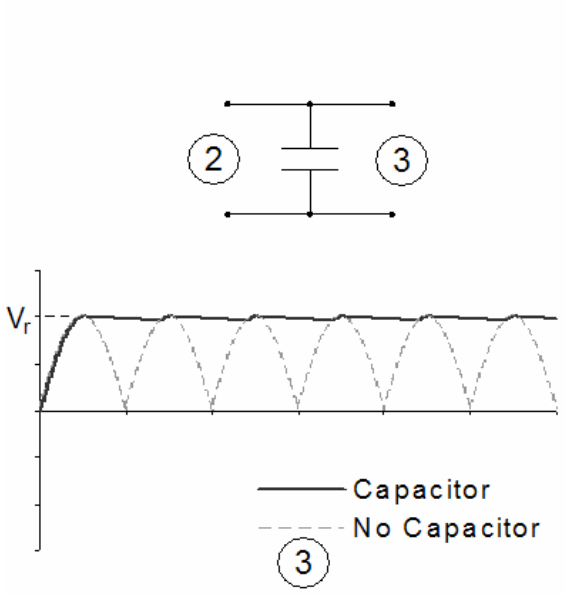

Figure 2.1.3. Additional capacitor to produce an almost-DC voltage output.

The size of the capacitor is typically sized to supply DC to the load. However, because the current that can be delivered from the PZT is very small, the charge must first be built up on a capacitor or stored in a rechargeable battery before it can be used. If we rearrange the first equation and make the assumption that the current input I is steady DC and that the initial voltage on a capacitor is zero, then the time Δt to charge a capacitor to a specified final voltage V_F becomes

$$\Delta t = \frac{CV_F}{I} \qquad \textbf{2.1.3}$$

Figure 2.1.4 shows the time to charge a capacitor up to 5 volts as a function of the current input and capacitance. While the steady current assumption is somewhat unlikely, it provides an idea of the sensitivity of the charge time in relation to the amount of current available.

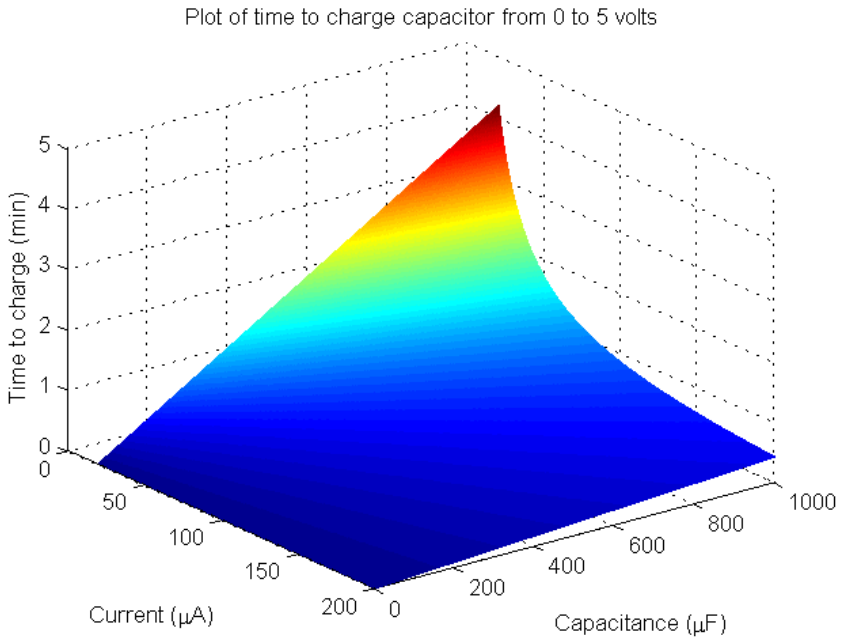

Figure 2.1.4. Plot of time to charge a capacitor to 5 volts as a function of capacitance and current.

The following sections of this chapter outline the various storage devices available for energy harvesting.

2.2 Current Battery Technology for Energy Storage

2.2.1 Basic Battery Theory

A battery is composed of two electrodes, a positive cathode and a negative anode, with a porous separator sandwiched between the two. In terms of battery charging, the speed of charge is usually determined by the milliamp hour (mAh) capacity of the battery. For example, if a source is rated at 400 milliamps, charging a 400 mAh battery would take 400/400 = 1 hour (C), while charging a 200 mAh battery would take 200/400 = 0.5 hours (0.5C). In all actuality however, charging a battery actually requires at least 1.5*C to fully replenish [17]. To avoid confusion, the notation for capacitance is an italicized *C* and the notation for the capacity of a battery is C.

While battery technology still trails the progress made in electronics and computing, new battery chemistries and improved manufacturing techniques have led to smaller, more reliable batteries for handheld electronics. At the time of publication of this article, almost every small, portable electronic device is powered by some kind of rechargeable battery of the nickel metal hydride or lithium ion/polymer variety. When a wall outlet or a car adapter is readily available, the efficiency of charging a battery is rarely considered. However, as the demand increases for wireless sensors that can be deployed and remain operable indefinitely, the efficiency of battery charging becomes crucial. In some cases, the possibility of other energy storage devices such as a capacitor must be considered, which will be discussed later.

2.2.2 Rechargeable Nickel Metal Hydride

Nickel metal hydride (NiMH) batteries use hydrogen, absorbed in a metal alloy, as the active negative material as opposed to cadmium used in nickel cadmium (NiCd) batteries [47]. For the most part, NiMH batteries have virtually replaced nickel cadmium (NiCd) batteries in rechargeable applications. This is attributed to the fact that NiMH batteries are not potentially harmful to the environment like their NiCd cousin. In

addition, NiMH do not exhibit signs of the so-called "memory effect" associated with the NiCd variety. The most common charging method for NiMH batteries is a constant-current charge, but with the current limited to avoid too great of an increase of battery temperature or to avoid exceeding the rate of the oxygen-recombination reaction [47].

While nickel metal hydride batteries are readily available, their use in storing such relatively small amounts of harvested energy is questionable as they are notorious for their extremely high discharge rate. In general, a nickel-based battery will discharge 10% to 15% of its capacity in the first 24 hours after charge, after which the discharge rate is an additional 10% to 15% per month. In comparison, the li-ion self-discharge is approximately 5% in the first 24 hours and 1% to 2% thereafter [20].

2.2.3 Rechargeable Lithium-based

At the time of publication of this document, the nickel metal battery is being replaced at a rapid rate by lithium ion batteries, which have an even greater specific energy and energy density [47]. In addition, lithium ion cells have a much higher discharge voltage of 3.6 volts, have a much lower self-discharge rate than that of NiCd and NiMH, and do not exhibit any memory effects [51].

Rechargeable lithium ion batteries utilize a reversible insertion and extraction of lithium ions into and from a lithium insertion compound during the discharging and charging cycle [51]. The open-circuit voltage V_{oc} of a lithium cell is calculated from

$$V_{oc} = \frac{\mu_{Li(c)} - \mu_{Li(a)}}{F} \qquad \textbf{2.2.1}$$

where F is the Faraday constant and $\mu_{Li(c)}$ and $\mu_{Li(a)}$ are the lithium chemical potentials of the cathode and anode, respectively. The nominal open-circuit voltage of most commercially available lithium ion rechargeable cells is 3.7 volts.

The capacity losses associated with the lithium's side reactions inside the cell are increasing with the depth of discharge per cycle. Some secondary lithium cells reach many cycles, but only under very shallow discharge conditions [39]. Therefore, while most lithium based secondary batteries claim between 500 and 1000 charge cycles of theoretical life, the actual life of the battery is typically much less than the upper limit.

For safety reasons, the maximum charge and discharge current for a lithium ion battery is limited to 1 C, though some newer chemistries allow up to a 20C charge or discharge rate. One fundamental issue concerning lithium technology is the fact that lithium metal's melting point is 180 ^{o}C. The liquid metal is highly reactive in contrast to the solid state. Upon reaching this melting point, the lithium tends to react with the cathode material and the components of the electrolyte, delivering a high amount of thermal energy [39]. For commercial and military aerospace applications, such an event could mean disaster or destruction in high altitude or outer space missions.

In comparison to nickel metal hydride batteries, lithium ion charging requires additional circuitry to ensure that the cell is neither overcharged nor overdischarged. Overcharging can be dangerous as described previously, and both conditions can reduce the overall life of the battery. Despite the dangers, lithium ion is still the portable rechargeable battery of choice because of its relatively high specific energy and energy density.

2.2.4 Rechargeable Thin Film Lithium Ion

Thin film batteries have existed for a little over a decade, with significant research being focused on the specific lithium ion chemistry and the thickness of cathode and anode layers. Performance variation from cell to cell is a major issue, attributable to film deposition and high temperature crystallization [25].

As of 2005, batteries fabricated using a crystalline $LiCoO_2$ cathode consistently provided maximum power levels up to 30 mW/cm^2 with negligible self-discharge and rapid charge rates with a relatively long cycle life. Cathodes composed of $LiMn_2O_4$ have also shown similar promising results, but repeatability is still an issue and further research needs to be performed [24].

As recently as 2006, Infinite Power Solutions ® began commercial manufacture of a 4.0V, 0.7 mAh thin film lithium ion battery that measured 1 in x 1 in x 0.0043 in. which performs similar to a super capacitor without the leakage current and with superior energy density. The electrolyte is disclosed as LiPON (Lithium phosphorus oxynitride)

and the cathode material is $LiCoO_2$ (Lithium Cobalt Oxide), though most of the other materials are proprietary. The battery claims to be capable of employing energy harvesting methods to recharge, as well as a superior operating life of greater than 10,000 charging cycles [4].

2.3 Current Capacitor Technology for Energy Storage

2.3.1 Electrolytic capacitors

An electrical capacitor consists of three essential parts, two of them being metal plates which are separated and insulated by the third part, the dielectric. The dielectric can be in a solid, liquid, or gaseous form or possibly a combination of these forms [21].

Capacitance is calculated using

$$C = \varepsilon_o \varepsilon_r \frac{A}{D} \qquad \textbf{2.3.1}$$

where ε_o is the permittivity of free space, ε_r is the relative permittivity of the insulating material between the electrodes, A is the surface area of each electrode and D is the distance between the electrodes [33].

The electrolytic capacitor differs from the conventional types of electrical capacitors in that instead of using two metal plates, only one of the conducting surfaces is metal. The other conducting surface is composed of a chemical compound or electrolyte [21]. The dielectric used in construction of the capacitor is a very thin film of oxide of the metal which constitutes the one metallic plate used in the structure [21]. For an aluminum electrolytic capacitor, the formation of the oxide film is achieved by introducing the metal into a suitable electrolyte and passing an electric current through it, whereby oxygen is evolved at the positive pole which oxidizes the surface of the aluminum [21].

A typical electrolytic capacitor is in the range of one up to several thousand or ten thousand microfarads. For most small electronic applications that utilize energy harvesting, this is too small of a capacitance to store enough energy. Several capacitors could theoretically be connected in parallel to increase the capacitance, but the size of

such a device would be impractical. Therefore, supercapacitors are often considered instead of electrolytic capacitors.

2.3.2 Supercapacitors

Supercapacitors, also referred to as ultracapacitors or electrochemical double layer capacitors, are different from the conventional electrostatic and electrolytic capacitors because they contain an electrolyte which enables the electrostatic charge to also be stored in the form of ions [75]. They are governed by the same fundamental equations as conventional capacitors, but utilize higher surface area electrodes and thinner dielectrics to achieve greater capacitances [33]. Since these devices store energy using ionic capacitance as well as by surface redox reactions, their classification lies closer to a conventional battery than its conventional capacitor relatives.

There continues to be confusion in the literature as the two surnames (super- and ultra-) are often used interchangeably and have vague definitions when used. Since in all actuality both words refer to the same device, the generic name 'electrochemical capacitor' has been proposed to refer to such devices [75]. However, for convenience, this type of device will still be referred to as a supercapacitor throughout this document.

A model of an actual capacitor must include an equivalent series resistance (ESR) to account for internal losses. A schematic of an actual capacitor is shown. Depending upon the application, the ESR can have a big impact on the voltage fluctuation across the capacitor during charging, as well as the current leakage rate out of the capacitor over extended periods of inactivity.

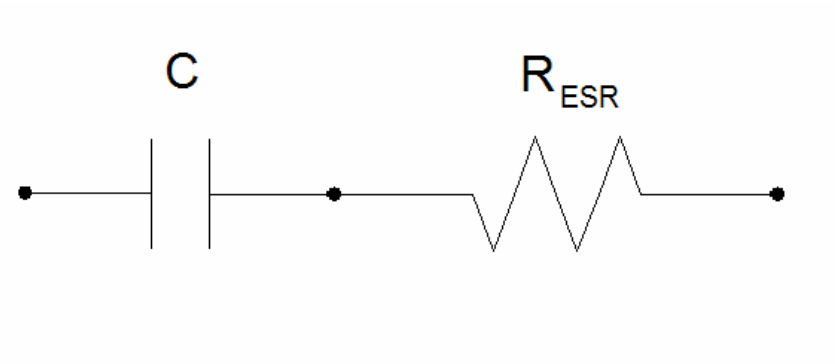

Figure 2.3.1. Schematic of realistic capacitor model incorporating ESR.

To demonstrate the impact of ESR on storage properties, a quick experiment was performed in a laboratory setting. The first capacitor tested was an Elna brand supercapacitor rated at 0.22 farads and 5.5 volts, with a reported equivalent series resistance of 75 Ω. This particular Elna capacitor falls within the definition of a supercapacitor since it uses an electric double layer storage technique. The second capacitor was a Cap-XX GS 211D supercapacitor rated at 0.3 farads and 4.5 volts, with an equivalent series resistance of 34mΩ. As a general rule of thumb, the equivalent series resistance decreases as the capacity of the supercapacitor increases. Figure 2.3.2 shows the voltage charging profile of each capacitor. The output of an electromagnetic generator was sent through a full bridge rectifier and then fed directly to the terminals of the capacitor. The graph is cut off because the ReadyDAQ data acquisition system used to record this data is not capable of measuring voltages above 5 volts.

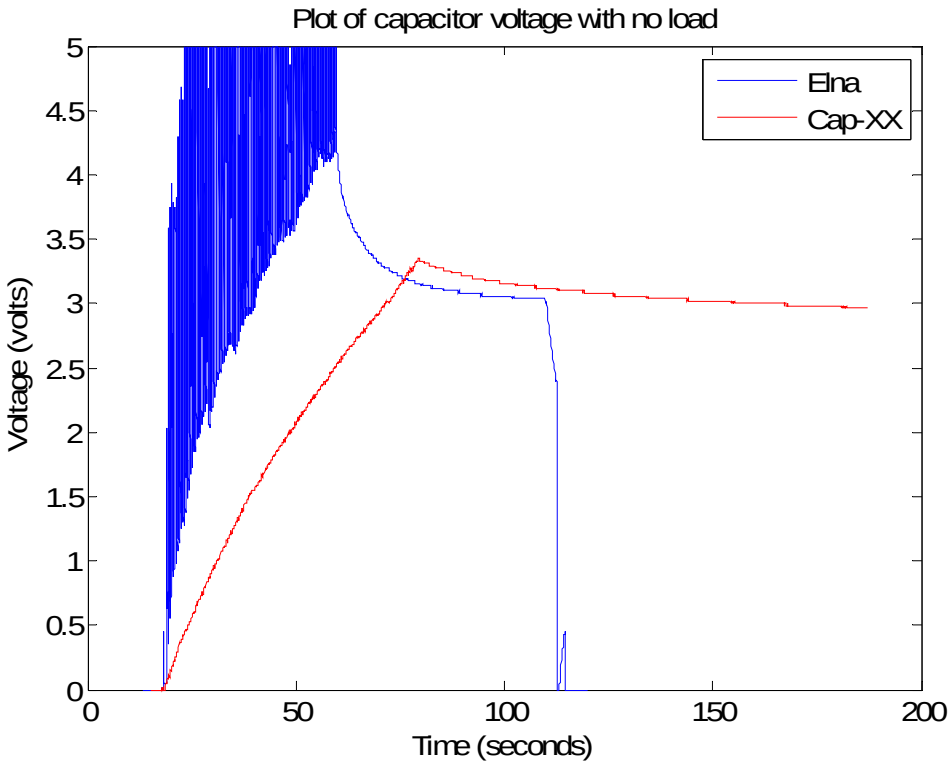

Figure 2.3.2. Plot of voltage of each capacitor with no load (overlapped).

The purpose of the previous experiment is to demonstrate the effects of ESR on both the ramp up and the leakage voltages of a supercapacitor. The results of the ESR on the voltage can be seen in the ramp up charging profile for each device. The Cap-XX experiences virtually no voltage spikes, while the Elna sees a spike as much as 3 volts higher than its nominal charge. The effect of higher ESR can also be seen by comparing the leakage of both capacitors in Figure 2.3.2. The Cap-XX supercapacitor has a very small leakage in comparison to the rapid decay seen by the Elna foil capacitor. However, because of its lower cost and ease of integration into printed circuit board designs, the Elna is more commonly used in commercial applications.

The maximum power P_{max} for a capacitor is given by:

$$P_{\max} = \frac{V^2}{4 \times ESR} \qquad \textbf{2.3.2}$$

where *ESR* is the equivalent series resistance of the capacitor. This is based upon a matched impedance, when $R = ESR$. By keeping the ESR small, supercapacitors are able to achieve relatively high power densities. However, despite greater capacitances than conventional capacitors, supercapacitors cannot yet match the energy densities of mid to high-end batteries [33].

2.4 Comparison of Energy Storage Methods

2.4.1 Batteries versus Supercapacitors - Energy versus Power Density

To compare the various energy storage devices, the terms energy density and power density must be used. Batteries have a high energy density but a low power density. Conversely, supercapacitors have a relatively high power density, but low energy density when compared to batteries. This means that capacitors cannot store as much energy, but the rate of energy transfer out of capacitors is much greater than that of a battery.

Figure 2.4.1 demonstrates the relative energy density of capacitors and batteries. Note that the horizontal axis is in logarithmic units. The inherent assumption is that if the 80 ohm resistor were a small scale electronic device, it would be capable of operation as

long as the supply voltage was greater than 1 volt. A fully charged nickel metal-hydride battery can sustain a useable voltage of greater than 1 volt for several orders of magnitude longer than a 1.0 Farad and a 0.3 F supercapacitor.

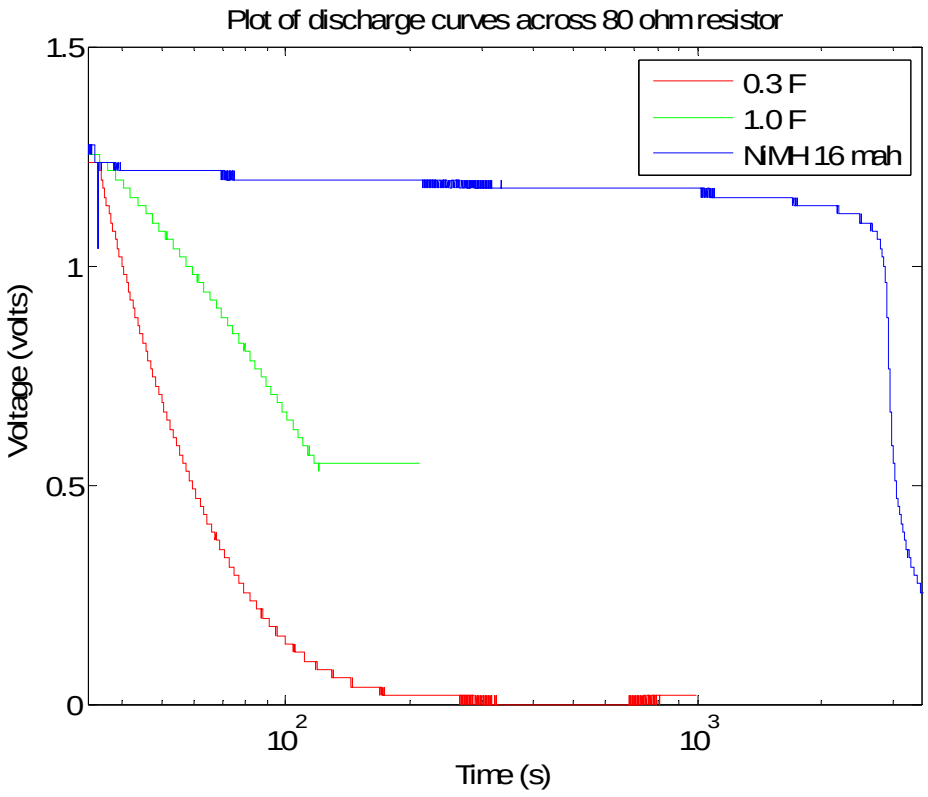

Figure 2.4.1. Discharge curves of two capacitors and a battery across an 80 ohm resistor.

The most recent development in supercapacitors is employing electrochemical energy storage similar to methods used in batteries. One of the most common types of supercapacitor is known as the electrochemical double layer capacitor, or EDLC. Because no transfer of charge between the electrolyte and the electrode occurs, the charge storage in EDLCs is highly reversible, accounting for their stable performance characteristics for as many as 10^6 cycles. In contrast, the cycle life of electrochemical batteries is generally limited to a maximum of 10^3 cycles [33].

For all electrochemical energy storage systems, including batteries as well as capacitors, self-discharge is an intrinsic property, occurring at a higher rate for supercapacitors [33]. Therefore, if ambient energy is only available for a small portion of

the day, a supercapacitor may have too high a self-discharge rate to be useful for wireless applications. On the other hand, if multiple sources of ambient energy are harvested, supercapacitors might be more desirable for energy storage.

2.4.2 Batteries versus Supercapacitors - Piezoelectric Energy Storage

Since piezoelectric based energy harvesting is of special interest, this chapter section is devoted into the analysis of the storage devices previously discussed for this specific type of harvesting. For this experiment, a Mide® QP45N actuator was used as a harvesting device, driven at a frequency of 25.0 Hertz. Though the base acceleration was not measured, the output of the function generator was set to output the highest possible voltage of 10 volts and the vibration of the cantilever was very noticeable.

The signal was first sent through a full bridge rectifier and then fed directly to a supercapacitor or to a battery. A brand new 20 milliamp-hour nickel metal hydride battery, a 1.0 Farad, 2.5 volt backup capacitor, and a 0.3 Farad, 4.5 volt supercapacitor were used to store the harvested energy. Each device was completely discharged using a 462Ω resistor and then charged under the given conditions for 100 minutes (1.667 hours). The charge curves are shown in Figure 2.4.2.

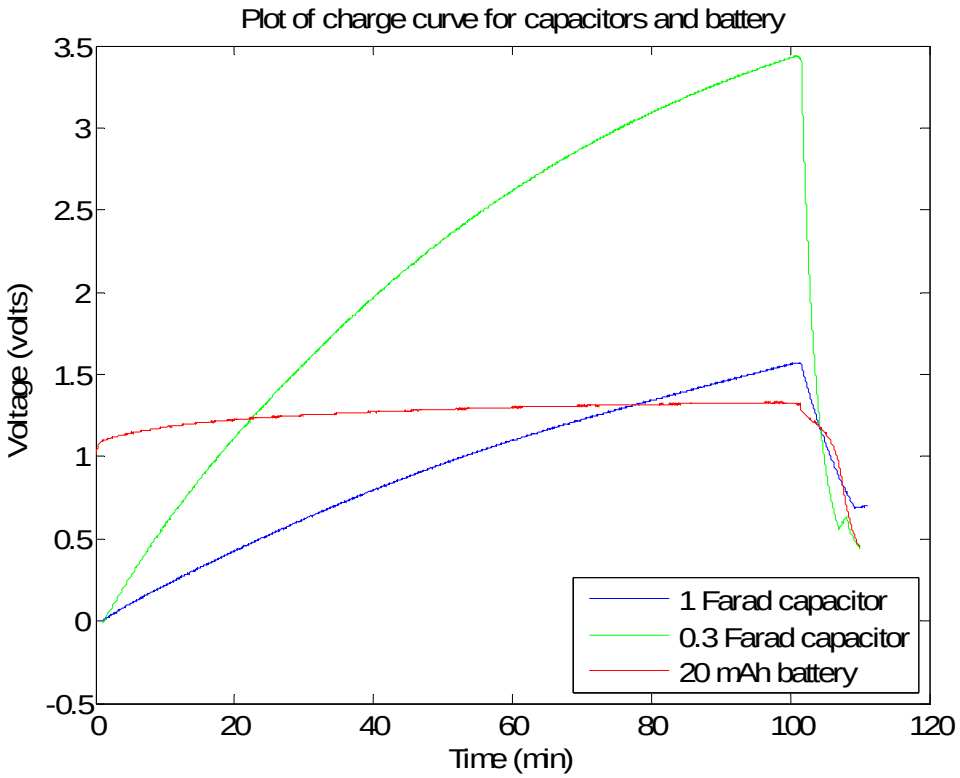

Figure 2.4.2. Charge curves for capacitors and a battery from ambient vibration energy.

As in an earlier experiment, the assumption is made that a voltage of greater than 1 volt is useful. Based upon this assumption, the battery and the 1.0 Farad and 0.3 Farad supercapacitors regained a certain amount of useable time to power a 462 ohm load as shown in Table 2.4.1. Overall, of the three devices tested, the battery supplied a useful amount of power to the load for the longest amount of time, as can be seen in Figure 2.4.3. Theoretically, a fully charged 1.2 volt NiMH battery rated at 20 mAh capacity should power a 462 ohm resistor for 7.7 hours when fully charged. According to this, the NiMH battery was only recharged to 1.3 % capacity.

Table 2.4.1. Summary of discharge characteristics.

	20 mAh battery	**1 Farad**	**0.3 Farad**
Maximum voltage attained	1.33 volts	1.572 volts	3.438 volts
Discharge time to 1 volt	5.25 minutes	4.27 minutes	3.30 minutes

According to Sodano et al [68], a nickel metal hydride battery is assumed to be charged to 90% capacity when the voltage of the cell reaches 1.2 volts. If this criterion was used for the 20 mAh battery, it would have been considered charged once it crossed 1.2 volts, which was 14 minutes into the experiment. The results from the previous experiment do not agree with this assumption, prompting further investigation.

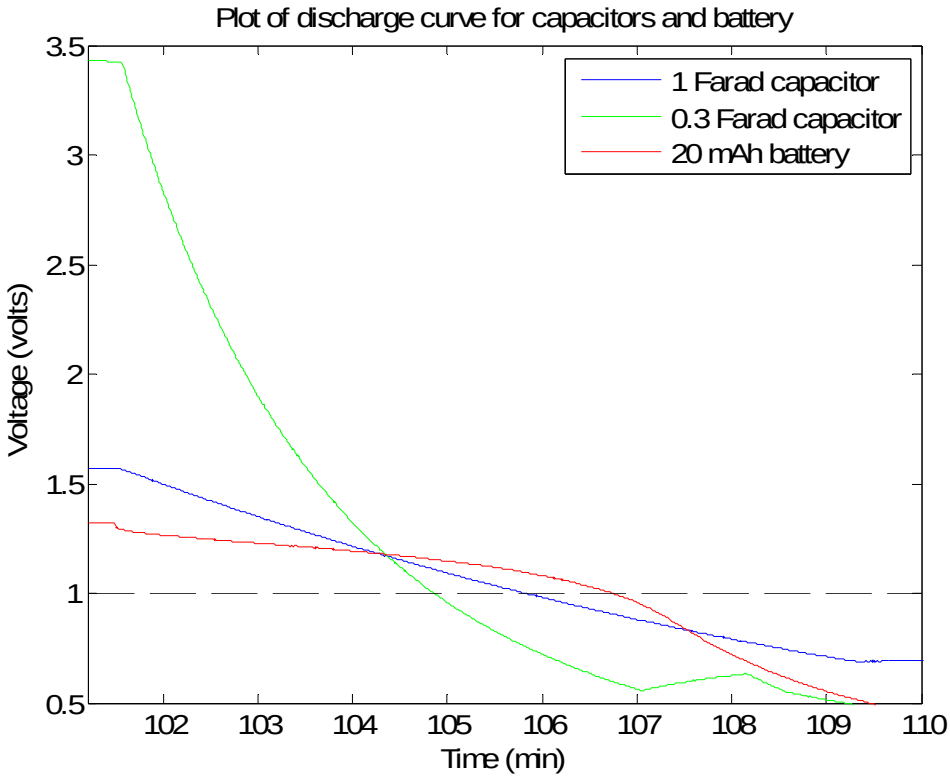

Figure 2.4.3. Discharge curves of capacitors and a battery across a 462 ohm load.

Figure 2.4.4 shows the charge curves for a 20 milliamp-hour nickel metal hydride battery using three different bimorph devices and a reference curve for a non-charging scenario. The first device is a QuickPack 45N, the second is an active fiber composite, and the third is an off the shelf actuator from Piezo Systems, Inc. Each bimorph was driven at its first resonant frequency, at the maximum 10 volt output of the function

generator. For each case, the battery is charged for at least 40 minutes and clearly attains a voltage across its terminals greater than the 1.2 volt threshold. The sharp drop at the end of each plot at times equal to 2260, 2339, and 2900 seconds, respectively, is when a 150 ohm resistor was connected to the terminals of the battery. From this plummet, we see that the battery was not charged at all.

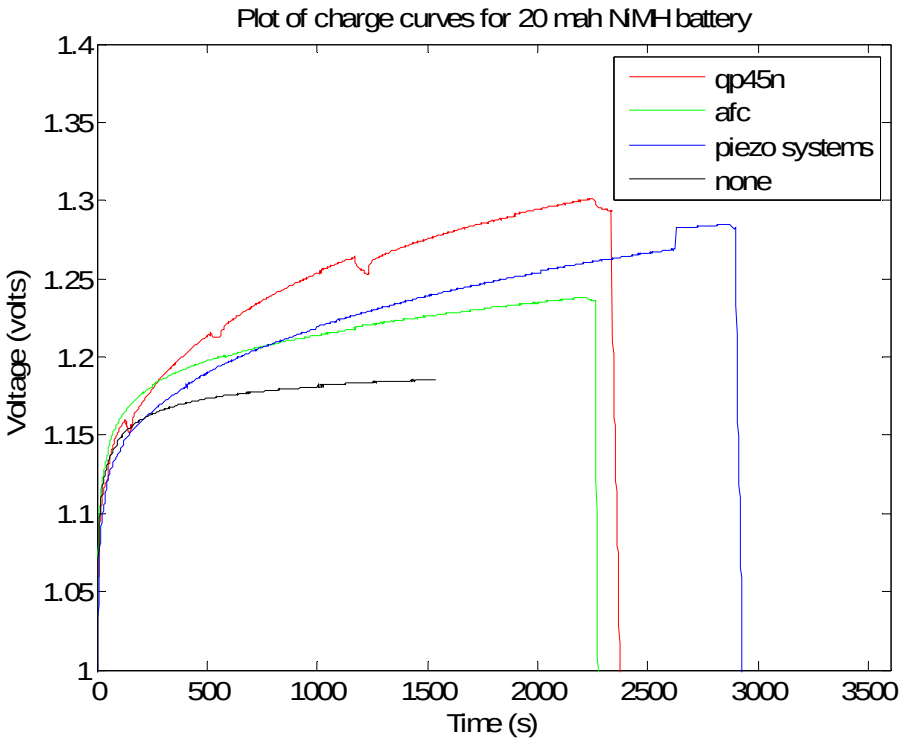

Figure 2.4.4. Plot of 20 mAh NiMH battery charging curves.

If any of the batteries in Figure 2.4.4 had been charged even partially, the discharge curve would look like that seen in Figure 2.4.5, which is provided as a reference. Additionally, Figure 2.4.5 shows that when the load resistance is removed and no charging system is connected, the battery will still rebound to 1.2 volts, unless it has been excessively discharged by leaving a load attached for an extended amount of time.

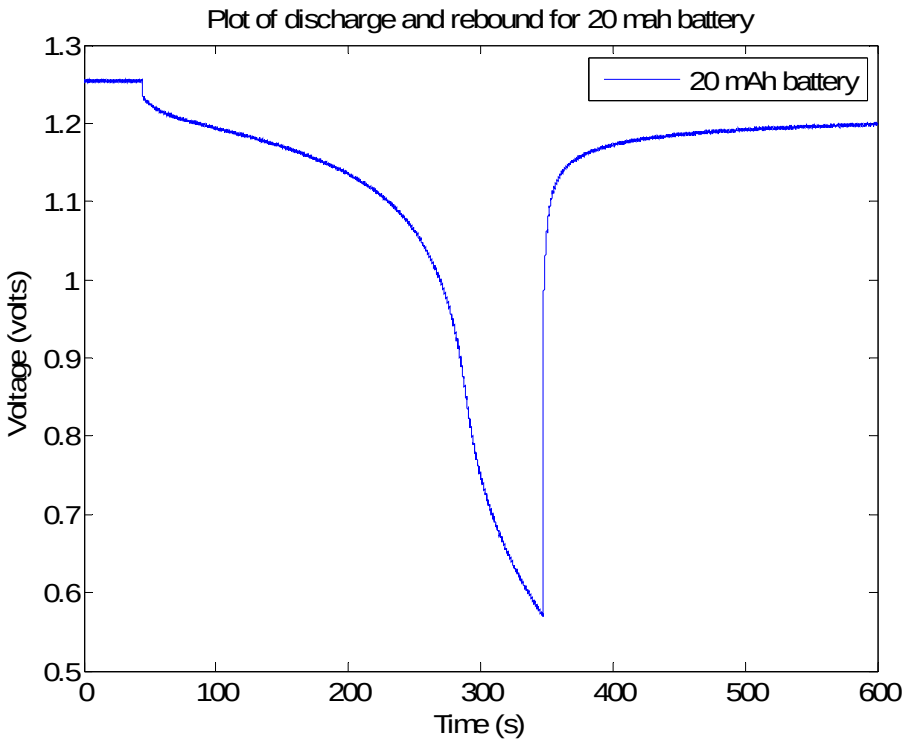

Figure 2.4.5. Reference plot of discharge curve across 150 ohm resistor.

The most reasonable explanation seems to be that there is not enough current output to recharge a battery. In an earlier paper, Sodano et al [69] used a QP40N actuator to harvest energy, very similar to the QP45N used in the present experiment. In the best case, the maximum current that Sodano was able to generate had an amplitude of 0.345 mA at a frequency of 30 Hertz and a load resistance of 100 Ω. While a NiMH button battery has a much smaller internal resistance of a few ohms, this current at this vibration frequency gives us some idea of what is available for charging.

Assuming that a steady DC current of 0.345 mA is available at a suitable voltage level of 1.5 volts, based upon a formula used to calculate battery charging times [3], the time required to recharge a 20 mAh battery becomes

$$Time = \frac{Capacity}{Current} = \frac{20mAh}{0.345mA} = 57.97 \ \ hours \qquad \textbf{2.4.1}$$

This is an idealized estimate, since the current input is clearly not a steady DC current, and the charging efficiency for a nickel metal hydride battery would be closer to 66%, not

the 100% assumed in this case. Additionally, it is generally accepted that a maintenance charge of 0.025 C (C/40) is adequate to counter self-discharge within NiMH hydride batteries [6]. Based upon this value, at least 0.500 *mA* would be required to keep the battery "topped off", so the battery would still be losing capacity due to internal losses in the previous scenario.

However, this number still gives an idea of the extreme length of time it would require to charge even the smallest NiMH battery. Based upon the previous calculation, a NiMH battery charged for 1.66 hours as described previously should regain 2.88% of its capacity. Not accounting for charging inefficiencies and internal losses, this value seems in close agreement with the 1.3% capacity regained in the first experiment. Alternatively, a lithium ion rechargeable battery has a much lower self-discharge rate and come in sizes as small as 3.0 V, 7 mAh capacity, so small piezoelectric devices could still be used to charge small lithium ion batteries, as will be shown in Chapter 3.

Chapter 3 - Piezoelectric Generators

3.1 Electrical Modeling of Piezoelectric Materials

From the IEEE Standards on Piezoelectricity [36], the direct and converse piezoelectric effects, respectively, are

$$\{D\} = [e]^T \{S\} + [\alpha^S]\{E\}$$
$$\{T\} = [c^E]\{S\} - [e]\{E\} \qquad \textbf{3.1.1}$$

where

{D} = Electric Displacement vector

{T} = Stress vector

[e] = Dielectric permittivity matrix

$[c^E]$ = Matrix of elastic coefficients at constant electric field strength

{S} = Strain vector

$[\alpha^S]$ = Dielectric matrix at constant mechanical strain

{E} = Electric Field vector

For energy harvesting purposes, the direct piezoelectric effect is utilized. Unlike a typical electrical power source, a vibrating piezoelectric device differs in that its internal impedance is capacitive rather than inductive [46]. A piezoceramic patch is most often modeled as an AC voltage source in series with a capacitor and a resistor, as shown in Figure 3.1.1. For even simpler models where the device is not being operated near resonance, the resistance is typically neglected.

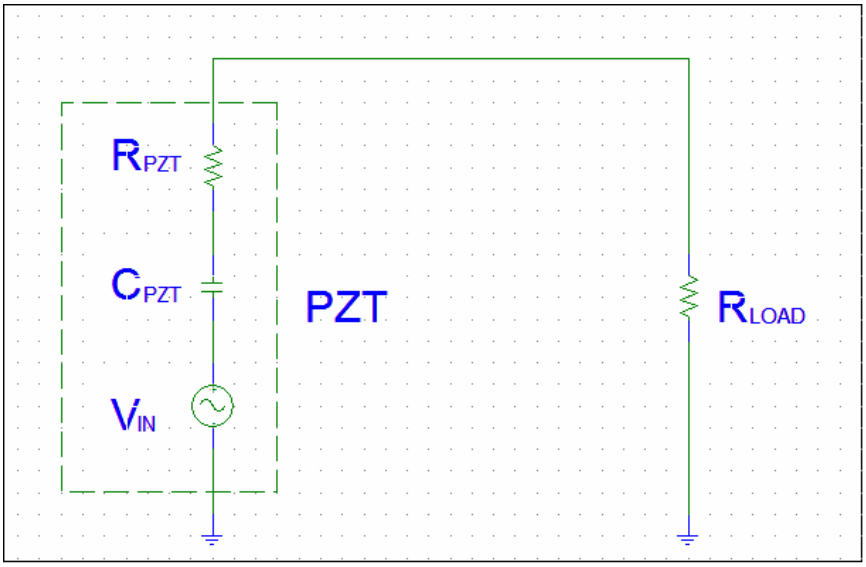

Figure 3.1.1. Model of piezoceramic as a sinusoidal voltage source in series with a capacitor and a resistor.

Piezoelectric materials act like a high voltage, low current power source when used for energy harvesting. The open circuit voltage can be found using

$$V_{OC} = -\frac{dt}{\varepsilon}T \qquad \textbf{3.1.2}$$

where d is the piezoelectric strain coefficient, t is the thickness of the piezoelectric material, T is the mechanical stress, and ε is the dielectric constant of the piezoelectric material. Since this voltage output is most commonly AC in nature, it must be sent through a rectifier circuit before it can be useful, as described in Chapter 2.

3.2 Piezo Systems Bimorph Modeling and Characterization

3.2.1 Bimorph Modeling

For power harvesting, the typical configuration of a power harvesting device is a bimorph, which consists of a thin metal substrate sandwiched between two piezoceramic patches. Most often, the bimorph is mounted in a cantilever configuration with a tip mass added to increase strain and to lower the natural frequency of the vibrating beam. The exact size of the mass attached to the tip can also be specified so that the bimorph

operates within the range of an ambient driving frequency base excitation. Figure 3.2.1 is a graphical representation of the simplest model for such a device. The first natural frequency of a slender cantilever beam with a concentrated end mass as given by Blevins is [12]

$$\omega_n = \sqrt{\frac{3EI}{L^3\left(M_b + 0.24M\right)}} \qquad \textbf{3.2.1}$$

where E is the modulus of elasticity, I is the moment of inertia, L is the length of the beam, M is the mass of the beam, and M_b is the concentrated bulk end mass. In reality, when an electromagnetic shaker is used to simulate the excitation and for many of the harvesting applications, the left end of the beam cannot be modeled as fixed but rather as another very large vibrating mass. Improved models are being developed by Erturk and Inman [30] to better modeled the left side of the beam. However, to simplify the equations in this section, the left end is assumed to have a fixed boundary condition.

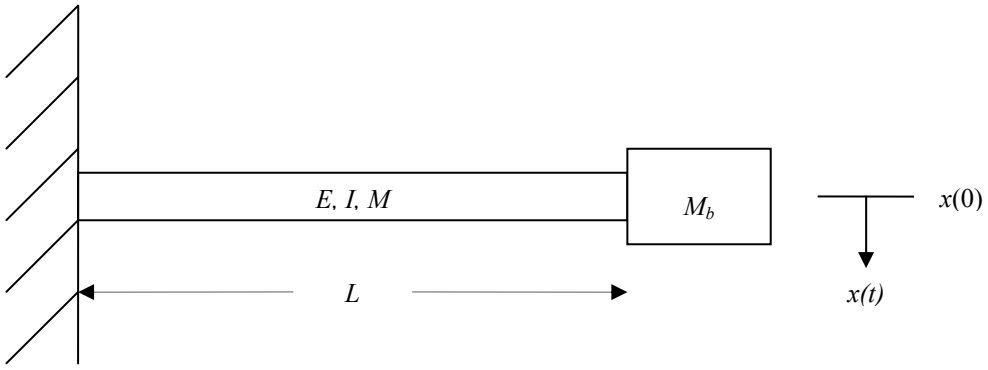

Figure 3.2.1. Cantilever beam with added tip mass.

A piezoelectric bimorph is more complicated than this simple cantilever beam model in that it consists of a metal shim layer sandwiched between two piezoceramic layers. Therefore, an equivalent Young's modulus and moment of inertia must be calculated in order to determine the first natural frequency. For the purposes of these calculations, the thickness of the bonding layers is neglected. Figure 3.2.2 is a cross section of such a bimorph device.

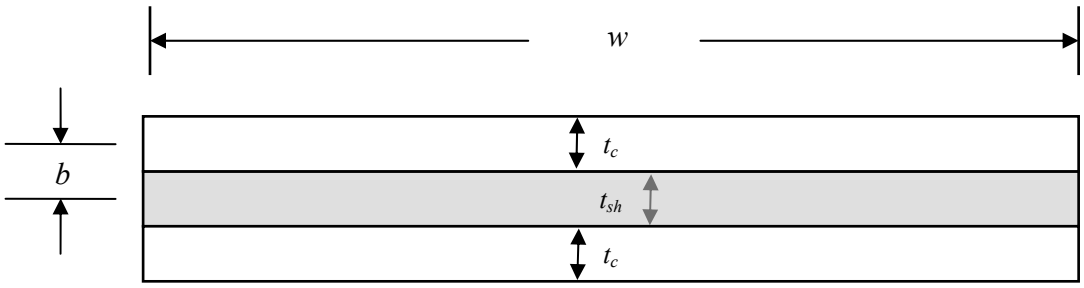

w = width of the beam

t_c = thickness of an individual piezoelectric ceramic layer

b = distance from the center of the shim to the center of the piezo layers

t_{sh} = thickness of the center shim,

Figure 3.2.2. **Layers representing a piezoelectric bimorph.**

The ultimate goal is to use a device such as the Piezo Systems, Inc. T226-A4-503X bimorph in a cantilever configuration with a tip mass to tune the first natural frequency to a desired value. Previous experimentation has been performed by duToit et al [26], but further investigation was performed in the lab to validate the proposed model. Some of the values obtained by duToit et al [26] are used for calculations here. According to the equations provided by Roundy, the effective moment of inertia is [63]

$$I = 2\left[\frac{wt_c^3}{12} + wt_c b^2\right] + \frac{\eta_s wt_{sh}^3}{12} \qquad \textbf{3.2.2}$$

where η_s = ratio of Young's modulus for piezo to Young's modulus for shim. The values required to calculate the effective moment of inertia are provided in Table 3.2.1, leading to an effective moment of inertia I of 8.29e^{-13} m^4. The equivalent Young's modulus can be calculated using [63]

$$E_{equiv} = \frac{2t_c E_c + t_{sh} E_{sh}}{2t_c + t_{sh}} = 73\ GPa \qquad \textbf{3.2.3}$$

Table 3.2.1. Properties of Piezo Systems, Inc. T226-A4-503X bimorph.

Beam width, w	31.75	mm
Beam length, L	55.0	mm
Piezo layer thickness, t_c	270	μm
Shim layer thickness, t_{sh}	140	μm
Distance from shim layer center to piezo layer center, b	205	μm
Young's modulus for piezo layer, E_c	66	GPa
Young's modulus for shim layer, E_{sh}	100	GPa
Ratio of Young's modulus for piezo to Young's modulus for shim, η_s	0.66	
Piezoceramic density, ρ_p	7800	kg/m^3
Shim layer density, ρ_s	7165	kg/m^3

The only remaining undefined variable is the bulk tip mass, M_b. Performing a parametric study, we can predict how the natural frequency should change as a function of the tip mass. Figure 3.2.3 plots the predicted first natural frequency as a function of the normalized tip mass, and Table 3.2.2 shows the predicted first natural frequency for several normalized tip mass values. With no tip mass added, the model predicts a first natural frequency of 112.49 Hz. The graph shows that the ratio of the tip mass to the device mass can greatly influence the first natural frequency when the tip mass to beam mass ratio is less than 2.

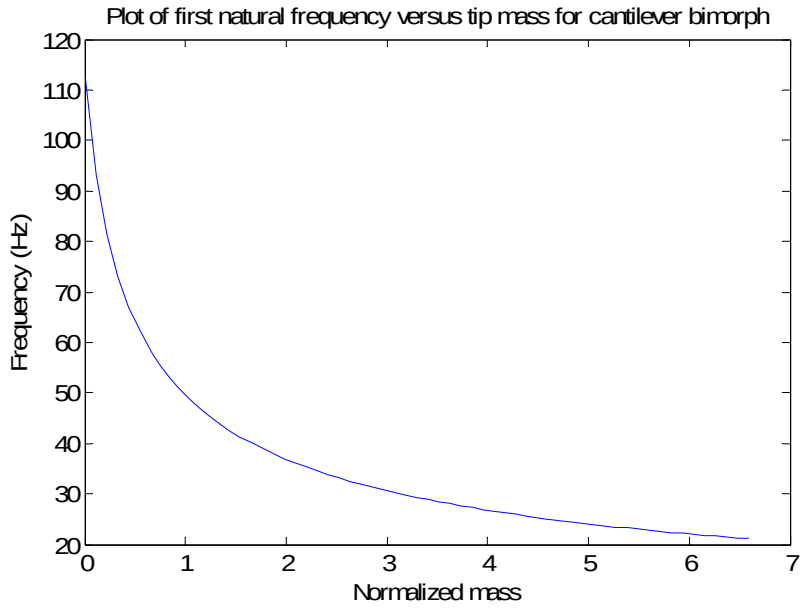

Figure 3.2.3. Tip mass effect on natural frequency of a cantilever configuration.

Table 3.2.2. First resonant frequency for normalized tip mass values.

Normalized tip mass	First Natural Frequency (Hz)
0	112.49
1	49.50
2	36.83
3	30.62
4	26.76
5	24.07
6	22.06

To validate the simple model used for these predictions, a second model from another literature source is used for verification. Adapted from Wang and Cross [85], the first natural frequency of a cantilever bimorph with no tip mass is

$$f_r = \frac{3.52t}{4\pi L^2}\sqrt{\frac{E_c}{3\rho_c}}\left[\frac{1+3(1+2B)^2+4AB^3}{4(1+B)^2(BC+1)}\right]^{1/2} \qquad \textbf{3.2.4}$$

Where $A = E_{sh} / E_c$, $B = t_{sh} / 2t_c$, $t = t_{sh} + 2t_c$, and $C = \rho_{sh} / \rho_c$. Based upon this calculation, the fundamental resonance frequency should be 106.89 Hz, which is very close to our previously predicted value of 112.48 Hz.

This section develops two simple model of a cantilever bimorph to predict the first natural frequency. The following section outlines the process used to validate these models experimentally.

3.2.2 Experimental Verification

Figure 3.2.4 is a photograph of the experimental setup and equipment. The equipment used for testing include a large concrete test stand, a Polytec laser vibrometer, and a dSpace data acquisition system (not in photograph) for measuring the output from a T226-A4-503X bimorph from Piezo Systems, Inc. The two variables recorded were the tip displacement and the open circuit piezoelectric voltage. The displacement of the tip was recorded by the laser vibrometer as backup for the piezoelectric data, but was not

utilized for these calculations. However, it will be used in later chapters for predicting the theoretical power output of a hybrid piezoelectric and electromagnetic harvester.

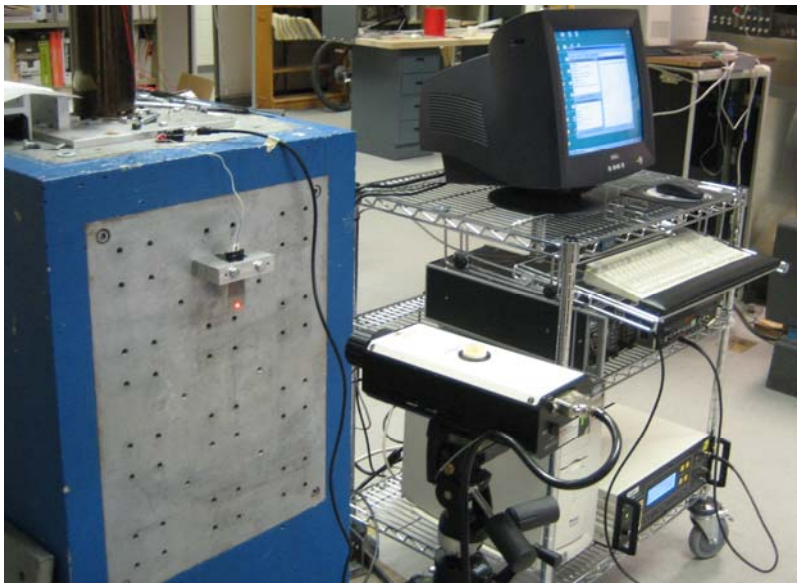

Figure 3.2.4. Photograph of test setup for Piezo Systems bimorph experiments.

It was initially proposed to use a Kistler impulse hammer to provide an initial disturbance to the bimorph. However, due to space issues, the impact hammer was unable to be used during testing. Therefore, the tip of a mechanical pencil was used to "flick" the tip of the cantilevered bimorph in the center to provide the initial disturbance.

Figure 3.2.5 is the open circuit voltage output of the piezoelectric bimorph after the initial disturbance for a case of no tip mass and a small 4.8 gram metal tip mass which was attached to the end of the bimorph using cyanoacrylate. Figure 3.2.6 is a plot of the tip displacement measured simultaneously by the laser vibrometer. A small piece of reflective tape of negligible mass was attached to the tip of the bimorph to reflect the laser beam.

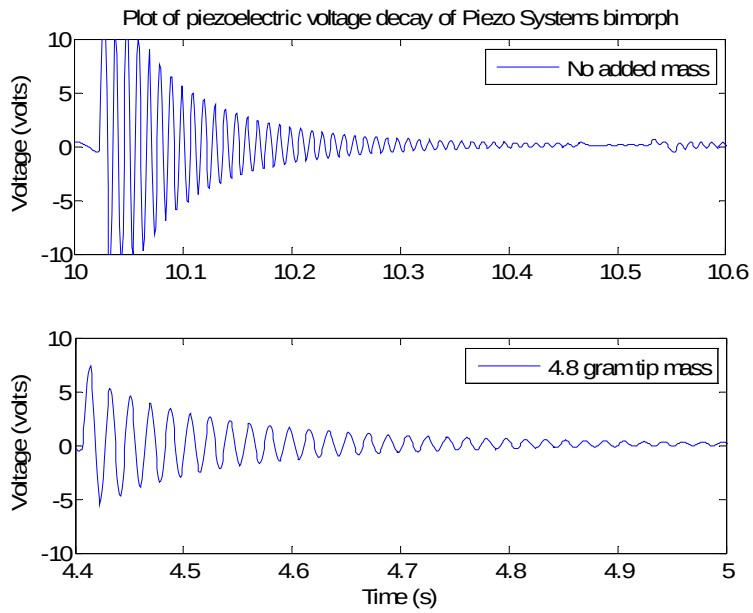

Figure 3.2.5. Plot of voltage decay of open circuit piezoelectric configuration.

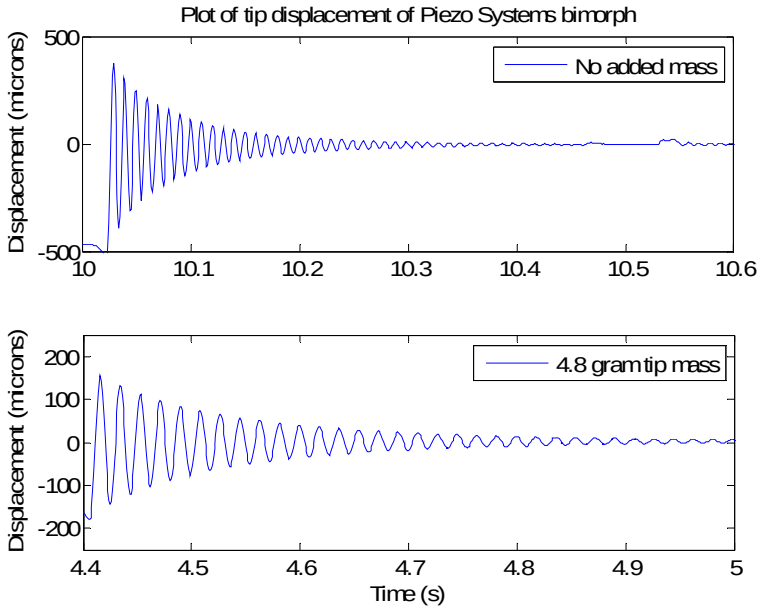

Figure 3.2.6. Plot of tip displacement measured by laser vibrometer.

In order to determine the mechanical damping ratio, the logarithmic decrement method is used. As defined by Inman [37], logarithmic decrement, denoted by δ, can be calculated from the experimental data using

$$\delta = \frac{1}{n} \ln \frac{x(t)}{x(t+nT)} \qquad \textbf{3.2.5}$$

where *n* is any integer number of successive positive peaks. Table 3.2.3 is a summary of the positive voltage peaks and the corresponding time for no added tip mass and a 4.8 gram tip mass. With these voltage values, the logarithmic decrement can be calculated from peak to peak. Averaging the δ values obtained, the damping ratio can be determined using

$$\zeta = \frac{\delta}{\sqrt{4\pi^2 + \delta^2}} \qquad \textbf{3.2.6}$$

Next, to determine the undamped natural frequency of the device, we can relate it to the damped natural frequency, ω_d, of the device using the relationship

$$\omega_n = \frac{\omega_d}{\sqrt{1-\zeta^2}} \qquad \textbf{3.2.7}$$

Table 3.2.3. Experimental values obtained for no tip mass and a 4.8 gram tip mass.

No mass added	
Time	Voltage
10.0682	9.1573
10.0784	7.8470
10.0885	6.7701
10.0985	5.8888
10.1086	5.1567
10.1186	4.5217
10.1286	3.9814
10.1386	3.5278
10.1486	3.1400
10.1585	2.8052
10.1685	2.5045
10.1784	2.2537

4.8 gram tip mass	
Time	Voltage
4.4138	7.346
4.4322	5.314
4.4507	4.6232
4.4694	3.9775
4.4877	3.4114
4.5059	3.0042
4.5244	2.6498
4.5427	2.3285
4.5609	2.0777
4.5792	1.8574
4.5975	1.6585
4.6156	1.4931
4.6339	1.3435

Table 3.2.4 provides a summary of the calculated variables of interest. Comparing to the analytical results, our models predict the first natural frequency of a bimorph with no tip mass with less than 12 % and 7 % error, respectively. Also, referring to the previous parametric study, the model predicts that a 4.8 gram tip mass should reduce the first natural frequency to 63.0 Hz, which is within a 14 % error margin to the experimental value.

Table 3.2.4. Summary of calculated variables for bimorph testing.

	No tip mass	4.8 gram tip mass
ζ_{mech}	0.0209	0.0229
ω_d (Hertz)	99.825	54.585
ω_n (Hertz)	99.847	54.599

The models developed in the previous section are shown to accurately predict the first natural frequency of the bimorph, even with an additional tip mass. The following section builds upon this information to examine the power generation capabilities of two bimorphs.

3.2.3 Power Generation Setup and Bimorph Characterization

The setup consisted of a Hewlett Packard 3314A function generator, two Ling Dynamic Systems shakers, two Piezo Systems, Inc. bimorphs, and a dSpace unit used for recording voltages. Because the direct output of the function generator sufficiently generated the desired acceleration vibrations, no amplifier was used. Special care was taken to construct two nearly identical shaker mounts for the bimorph devices, and to ensure that the clamped length of each bimorph was 55.0 mm, similar to the boundary conditions described by du Toit et al [26]. The wires attached to the bimorph are all the same length, and the BNC cables leading to the dSpace computer are very close to the same length. A special box, seen in the bottom right corner of Figure 3.2.7, was

constructed using two six-position switches that allowed for the switching between thirty six possible resistor combinations very rapidly to reduce the overall testing time.

The original intent of constructing two identical shaker mounts and bimorphs was to ultimately test the effects of unequal and out of phase vibrations when the two bimorphs were wired together. Some preliminary results were obtained, but are not presented.

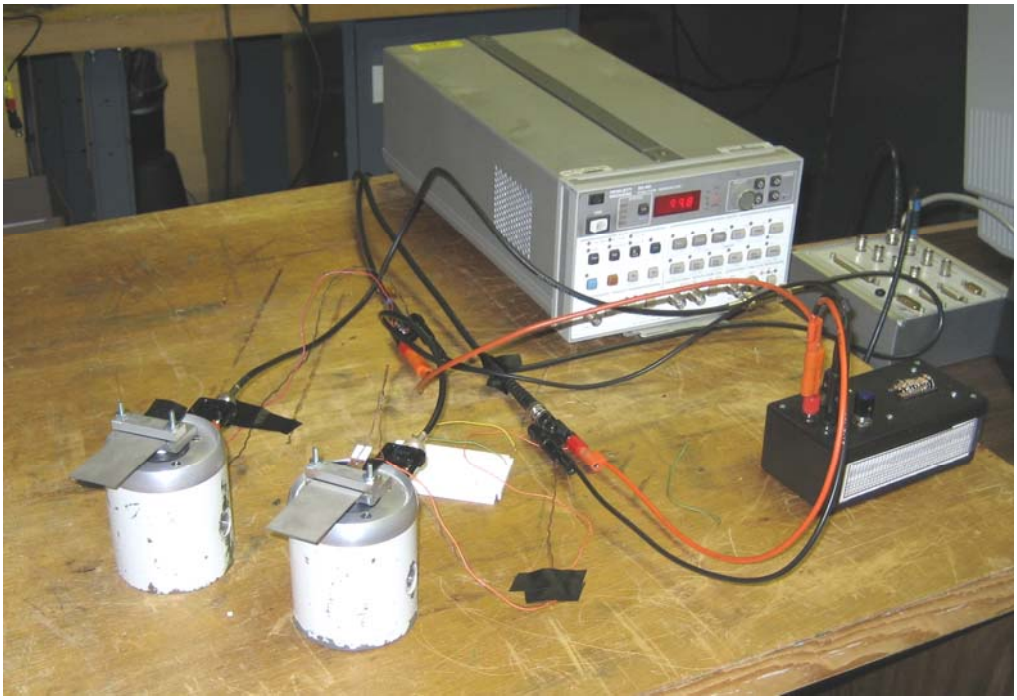

Figure 3.2.7. Photograph of multiple bimorph testing setup and equipment.

Based upon previous results, the function generator was set to output a sine wave of a particular voltage at 99.8 Hertz, corresponding to the experimental first natural frequency of the bimorph device. Some errors may arise due to the fact that the mass at the shaker end has not been properly modeled and the bimorph cannot truly be considered a cantilevered beam with a fixed base in this configuration.

To first study the device, a characterization of the open circuit voltage as a function of the input acceleration was performed. Figure 3.2.8 is a photograph of the experimental setup with a Kistler teardrop accelerometer affixed to the top of the shaker to measure the input acceleration of the first bimorph. The voltage on the function

generator was increased from 1 to 10 volts in one volt increments, and the corresponding piezoelectric open circuit voltage and the peak to peak acceleration values were recorded. The process was again repeated on the second bimorph, and the results were recorded and plotted alongside the first test results in Figure 3.2.9.

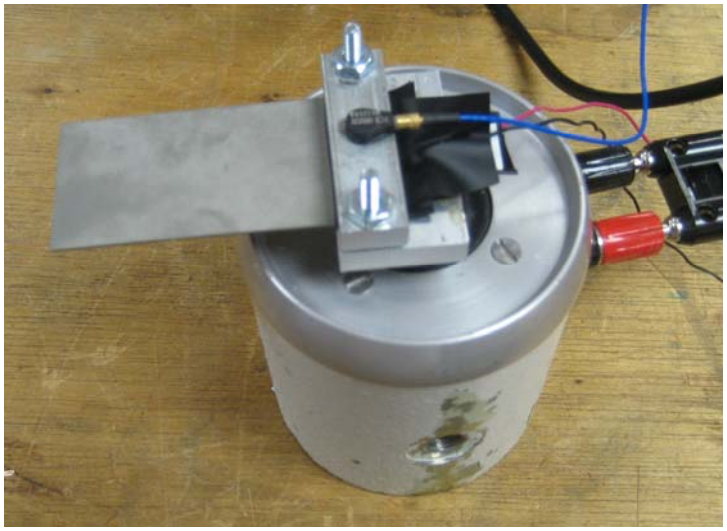

Figure 3.2.8. Photograph of test setup with Kistler teardrop accelerometer secured to the base.

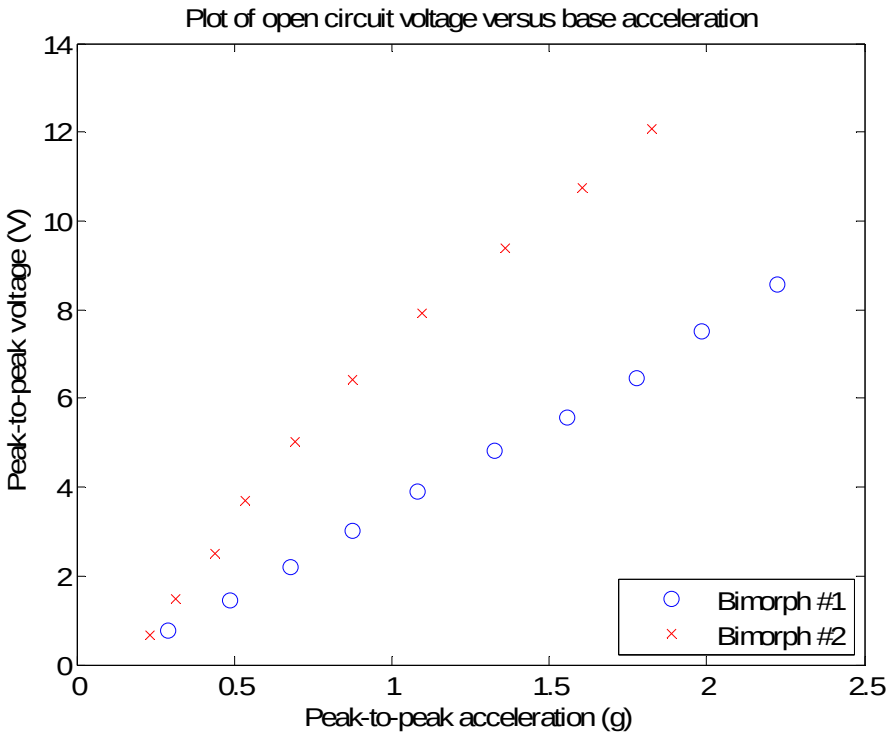

Figure 3.2.9. Plot of peak to peak voltage as a function of base acceleration.

Comparing these results to duToit et al [26], both bimorphs used in this experiment appear to have a higher open circuit voltage than the ones tested in their research. One possible explanation is that the clamping condition of the bolts used to secure the device to the base was not controlled as they were in their experiments. This would also explain the discrepancy between these two bimorphs during laboratory testing.

Once the open circuit voltage of each device had been characterized, the next step was to measure the power generation capabilities. A small capacitor was added in parallel with the resistor in order to smooth the delivered voltage, making the voltage easier to discern. The power was calculated using

$$P = \frac{V_{del}^2}{R} \qquad \textbf{3.2.8}$$

where V_{del} is the voltage delivered to the resistor and R is the resistance value.

Figure 3.2.10 demonstrates the power harvesting curves using the T226-A4-503X bimorphs from Piezo Systems, Inc. It is important to note that the power measured was of a rectified signal, not the direct output of the bimorph. This is a more accurate depiction of the useful power output of these devices for wireless and other electronic applications.

The acceleration input was not directly measured, but based on open circuit measurements in comparison to Figure 3.2.9, it is estimated to be about 0.75 g's peak to peak. Combining the two bimorphs in parallel clearly lowers the effective impedance, which in turn lowers the impedance requirement of the load necessary to maximize the power output. However, when the resistive load is relatively large, the power output from two bimorphs is not significantly greater than only one bimorph. The results of using a larger capacitor to smooth the voltage output suggest that the size of the smoothing capacitor affects the amount of power that can be delivered to a resistive load. This is attributed to the non-ideal behavior of the capacitor, which leads to internal losses.

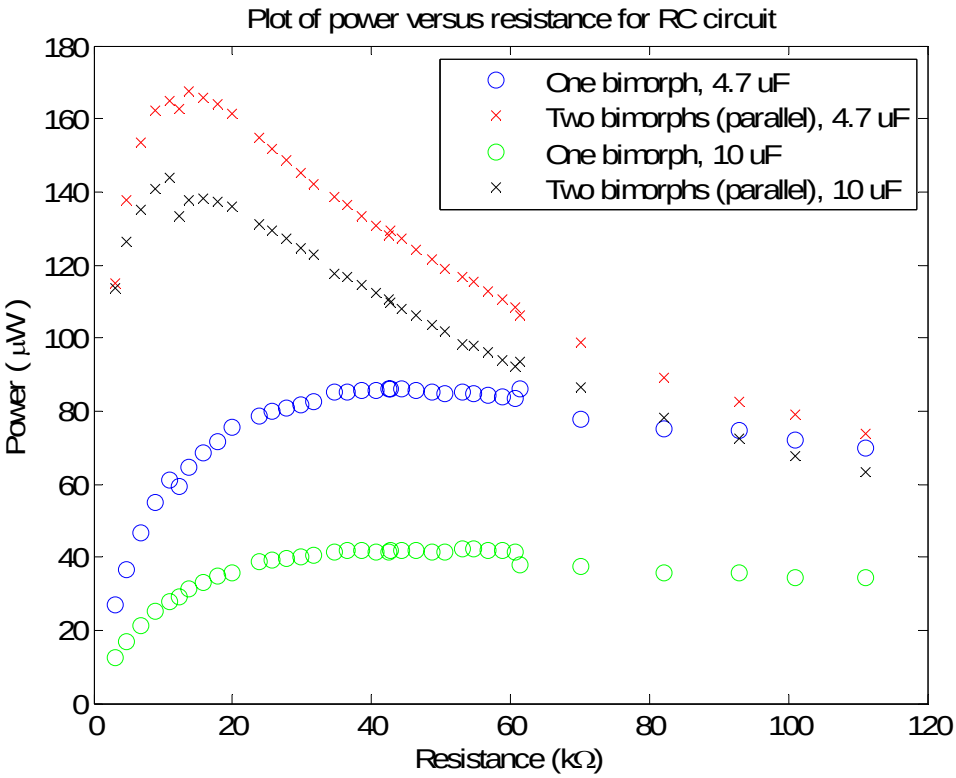

Figure 3.2.10. Plot of power curves for a 4.7 and 10 µF capacitor and various resistor values.

This section analyzes the basic power generation properties of two piezoelectric bimorphs vibrating in tandem. The experimental results confirm the theory that wiring two bimorphs together in parallel both increases the power output and decreases the overall impedance by a factor of two, as can be seen in Figure 3.2.10. The following section examines active fiber composite materials for the purpose of power harvesting.

3.3 Active Fiber Composite Bimorph Modeling and Characterization

A new manufacturing process patented by Advanced Cerametrics, Inc., called Viscose Suspension Spinning Process (VSSP) is used to produce ceramic materials, specifically piezoceramics, in fiber form which possess the desirable electrical properties of piezoelectric materials while eliminating the detrimental properties, such as fracture

and weight, inherent to monolithic piezoceramic designs [1]. These fibers are then suspended in an epoxy matrix and connected using interdigitated electrodes, creating an active fiber composite (AFC) which looks and behaves similar to a macro fiber composite device (MFC). Because of the laminate used to protect the fibers, either a riveting method or silver epoxy must be used to attach electrical leads.

While active fiber composites are often compared to macro fiber composites in terms of flexibility and mechanical properties, the method of construction is vastly different than the process described above. Alternatively, MFCs are manufactured from a diced monolithic piezoceramic patch rather than from an extruded fiber.

3.3.1 Battery Charging using Active Fiber Composite Bimorph

A Hewlett-Packard 6825A Bipolar Power Supply/Amplifier, a Ling Dynamics systems V203 permanent magnet shaker to induce vibrations, a DSPT Siglab 20-42, and a dSPACE data acquisition system were used for experimentation. A bimorph sample, consisting of two active fiber composites (AFCs) super-glued to a thin piece of steel shim sandwiched between them, was used for the power harvesting experiment. Figure 3.3.1 is a photo of the sample, donated for this experiment by Advanced Cerametrics, Incorporated.

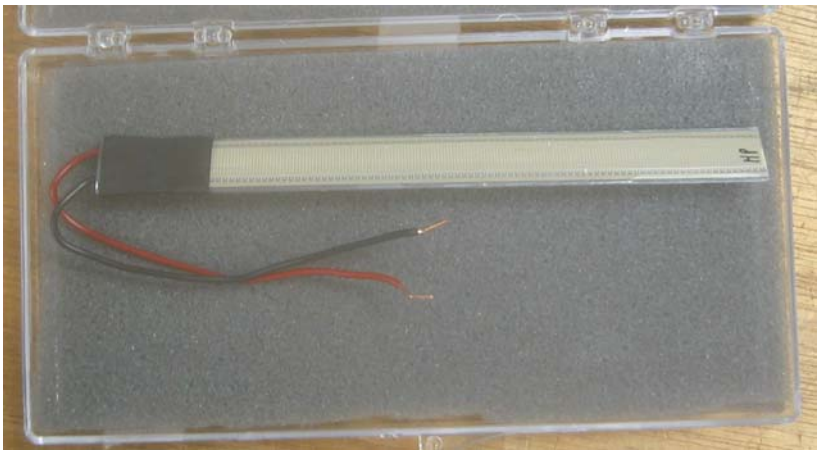

Figure 3.3.1. Photograph of bimorph sample in its protective plastic case.

A small aluminum test fixture was built to secure the sample to the shaker. The charging circuit was constructed on a standard breadboard using a full wave rectifier, a 220 μF capacitor (rated to 160 volts), and the battery to be charged. The first battery to be charged was a Varta brand 40 milliamp hour (mAh) battery, and the second was a GP brand 80 mAh battery. Both batteries were of the nickel metal hydride (NiMH) variety.

Figure 3.3.2. Photograph of AFC attached to the shaker, vibrating at its first natural frequency.

The bonding layer and material properties were not sufficiently known to predict the first natural frequency, so the value had to be determined experimentally. The first step of the analysis involved using the Siglab to perform a sine sweep from 0 to 250 Hertz as the voltage across a 14.837 kΩ resistor was recorded so that power output could be calculated. Figure 3.3.3 illustrates the voltage, current, and power output for the duration of this sweep. From these results, it was determined that the first natural frequency was 25.3 Hertz. The shaker was then set to vibrate at this frequency, which corresponds to the maximum power output from the AFC bimorph. The base input force provided by the shaker was not recorded.

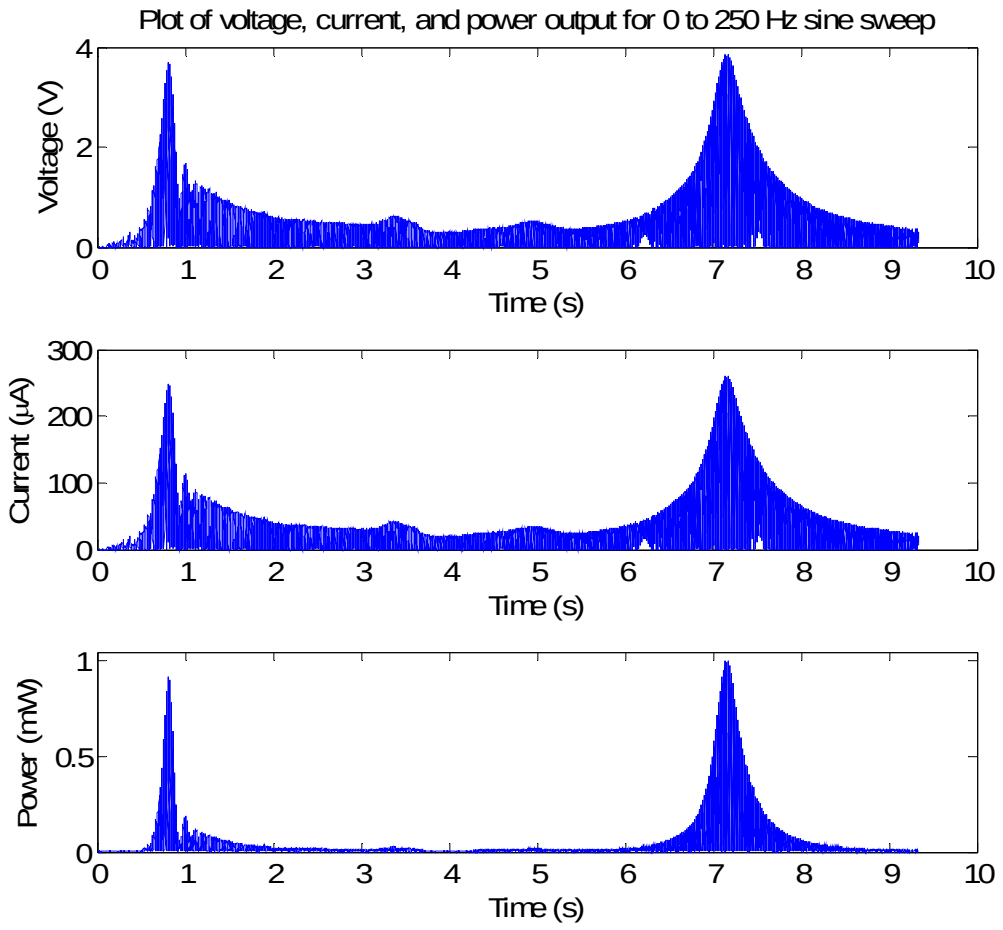

Figure 3.3.3. Voltage, current, and power output from Siglab sine sweep testing.

The red line graphed in Figure 3.3.4 shows the charge on a 40 milliamp-hour (mAh) battery as the AFC bimorph is subjected to vibrations for a duration of five hours. Also shown in Figure 3.3.4 is the charge on an 80 mAh battery under similar conditions, except the vibration level of the shaker has been increased, which accounts for the rapid charging time as compared to the less powerful button battery. This graph is comparable to the expected charge curves of a button battery being replenished at a trickle-charge rate, according to the work published by Sodano et al [68].

Although the AFC bimorph is quite flexible and can withstand severe vibration disturbances which producing an AC voltage large enough to light up a small green nightlight, it can still take two hours to fully charge a standard button battery, or the battery may only be charged up to a very small fraction of its capacity. If the criteria

established by Sodano et al [69] is used, then both batteries are recharged after approximately two hours, when they both attain a voltage of 1.2 volts. If the criteria established in Chapter 2 is used, the batteries regained less than 5% based upon these charging curves. However, it is impossible to test either hypothesis, since these batteries were never reconnected to a load to establish their state of charge.

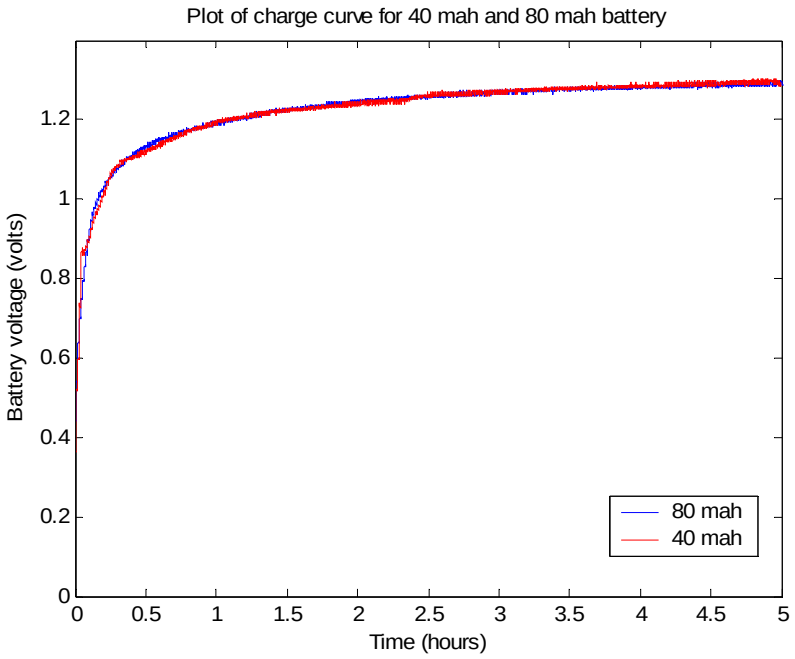

Figure 3.3.4. Plot of a 40 mAh and an 80 mAh battery

The long charge time is attributed to the fact that, much like their macro-fiber composite (MFC) relative, AFCs are plagued with a low current output which hinders the rate at which the battery can charge. Present research in power harvesting using piezoelectric devices has focused on finding an efficient DC-DC converter to step down the voltage and increase the current. However, no device is 100 % efficient, and the losses within available DC-DC converters are too great for them to be useful in most power harvesting circuits.

3.3.2 Active Fiber Composite and Piezo Systems Comparison

While the output of an active fiber composite charges a NiMH battery extremely slowly, the energy could possibly be stored in a capacitor in a more efficient manner. Therefore, it was decided to compare the harvesting capability of an active fiber composite bimorph versus a monolithic piezoelectric bimorph for energy storage in a capacitor. A special base was constructed to accommodate both the Piezo Systems and the Active Fiber bimorphs, as shown in Figure 3.3.5.

Because the devices were different sizes and shapes and hence different natural frequencies, it was deemed unfair to compare both devices at a single frequency. Therefore, frequencies of 30, 60, and 90 Hertz were chosen for testing. The output of each bimorph was fed through a full bridge rectifier and used to charge up a 1000 μF capacitor from zero initial voltage and the results are plotted in Figure 3.3.6. For all three cases, the monolithic bimorph performed better in comparison to the active fiber composite, not only in the rate of charging but also in the maximum voltage obtained. For the 30 Hertz case though, the voltage obtained is not significantly different between the bimorphs, suggesting that the active fiber composite bimorph performs better at lower frequencies. However, as was seen in the previous section, the natural frequency of any bimorph can be tuned by attaching a mass to the tip of the device.

Figure 3.3.5. Photograph of test mount for AFC and PS monolithic bimorphs.

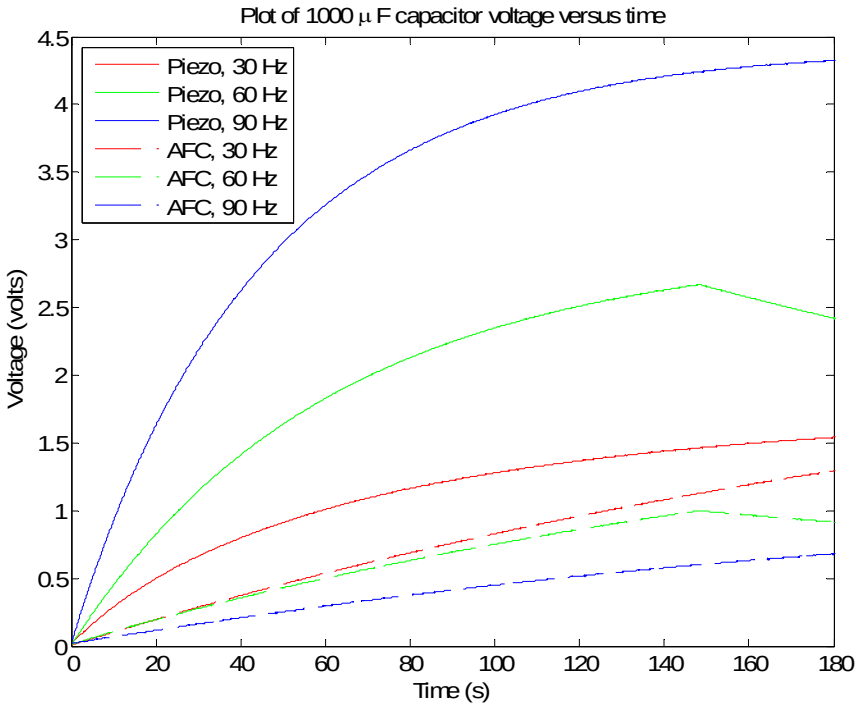

Figure 3.3.6. Capacitor voltage plots for AFC and PS bimorphs for various input frequencies.

At all three frequencies tested, the monolithic bimorph charged a 1000 μF capacitor to a higher voltage and faster than the active fiber composite bimorph. Again, this is due to the interdigitated electrodes which increase the voltage but lower the current output of active fiber composites, which in turn slows down the rate at which the capacitor can be charged.

3.4 Macro Fiber Composite Harvesting

While it was established by Sodano [70] that macro fiber composite (MFC) devices are incapable of recharging a battery due to low current output, the only coefficient tested was the d_{33} coefficient. This section explores the possibility of using MFCs utilizing the d_{31} coefficient to harvest ambient energy. The theory behind using

MFCs in the d_{31} mode is that the poled capacitance of such a device at 1 kHz is 4.6 nF/cm^2. In comparison, a similar d_{33} device at the same frequency has a poled capacitance of 0.42 nF/cm^2, which is an order of ten smaller than its d_{31} counterpart. Additionally, MFCs utilizing the d_{31} coefficient do not have interdigitated electrodes, but rather a grid of a positive electrode on one side and a grid of a negative electrode on the other. This has the effect of lowering the overall voltage output in comparison to conventional MFCs, but increases the overall current output.

The MFC output was fed through a full bridge rectifier and, using the special resistor box mentioned earlier in the chapter, the voltage across each resistance value was measured. Figure 3.4.1 is a photograph of the MFC bimorph constructed in the lab. The brass substrate used was 10.41 mm x 3.3 mm x 0.254 mm, and the MFC patches were adhered using thin cyanoacrylate adhesive. For the set of tests performed, the patches were wired in parallel so that the overall impedance would decrease and so the current would increase. From open circuit measurements of the voltage output of the device, the first natural frequency of the bimorph was determined to be 23.5 Hertz.

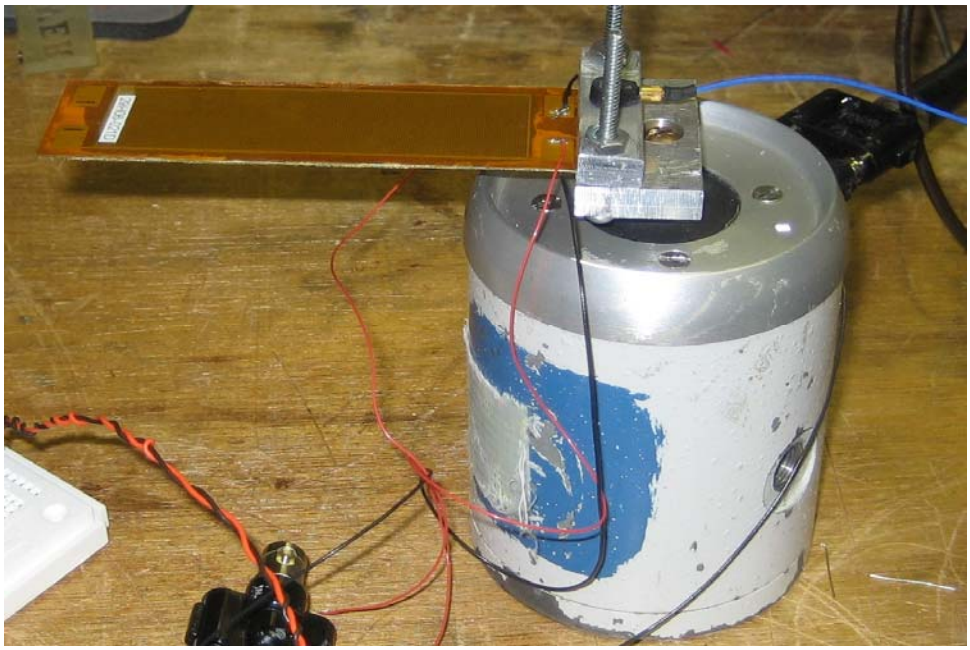

Figure 3.4.1. Photograph of MFC bimorph constructed in the laboratory.

Figure 3.4.2 is a plot of the results in comparison to those obtained using the monolithic Piezo Systems, Inc. bimorph. It is important to note that the MFC bimorph was driven at a frequency of 23.5 Hertz, while the PS bimorph was driven at 99.8 Hertz. Furthermore, the PS is in a series configuration, while the MFC bimorph is wired in parallel. Nevertheless, the MFC device performed much better than the monolithic bimorph in delivering power to a resistor after the signal was sent through a full bridge rectifier.

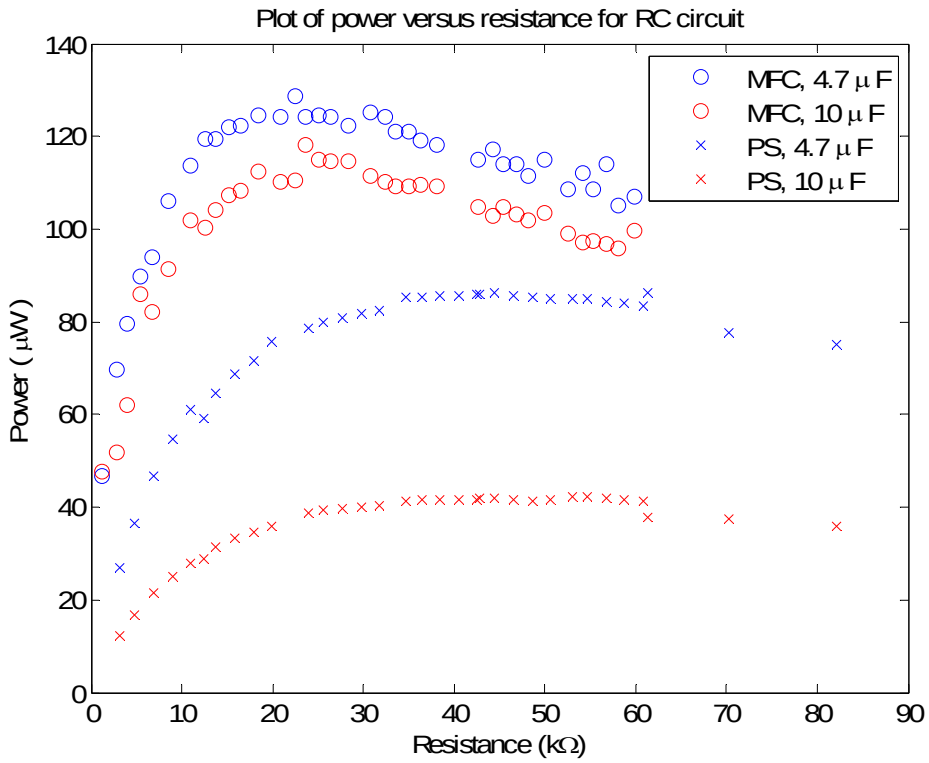

Figure 3.4.2. Power curves for monolithic and macro fiber composite bimorphs versus resistance.

As a further comparison, the Piezo Systems bimorph, the active fiber composite bimorph, and the macro fiber composite bimorph were mounted to a Ling Dynamic Shaker using a single mount. A photograph of the setup is shown in Figure 3.4.3. Each output was sent through a full bridge rectifier and then used to charge a 100 μF capacitor. A plot of these charging results is provided in Figure 3.4.4. For each frequency, either one or two of the bimorphs is omitted because the power output was less than 5 μJ over the sampled time. This plot demonstrates the dependence of the energy output for each bimorph on the imput frequency. The MFC bimorph stores energy at a faster rate than

the PS bimorph at the beginning, but ultimately stores less energy than the PS bimorph at 22 Hz, which seems to contradict the results presented in Figure 3.4.2. However, the MFC bimorph is wired in parallel while the PS bimorph is wired in series. Therefore, while the MFC produces a lot of current to charge the capacitor faster, it cannot output a voltage as high as the PS bimorph, and cannot charge the capacitor up to a voltage as high as the PS bimorph, resulting in less stored energy.

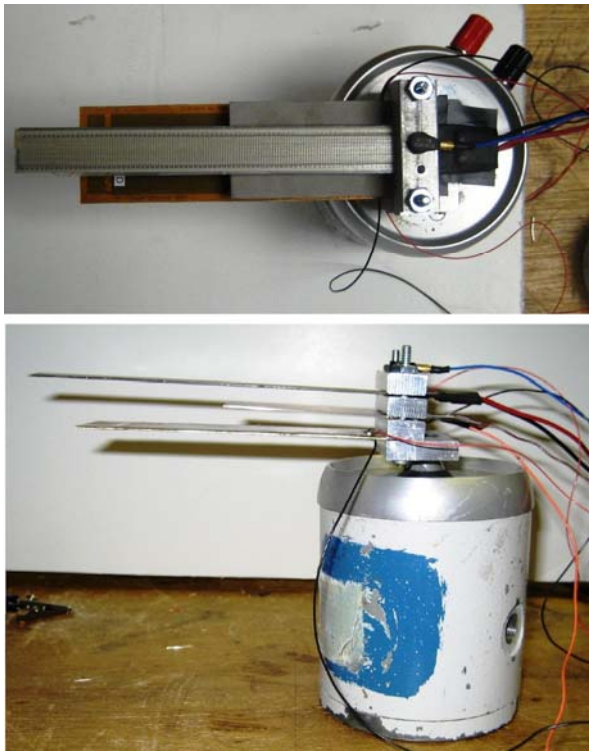

Figure 3.4.3. Photograph of AFC, PS, and MFC bimorphs mounted to an electrodynamic shaker.

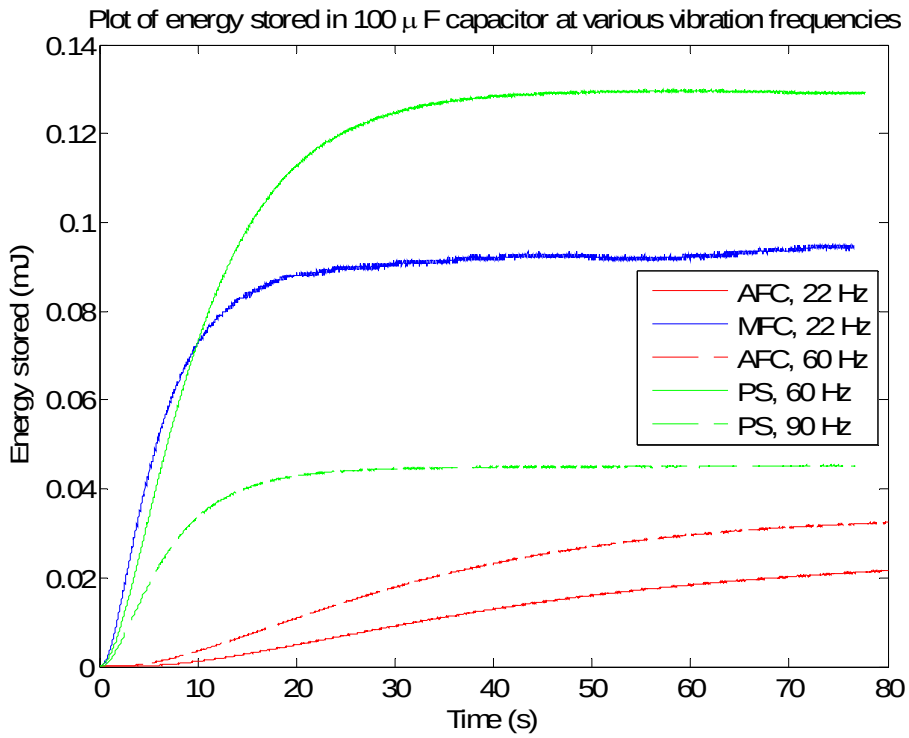

Figure 3.4.4. Plots of energy stored in 100 µF capacitors using AFC, MFC, and PS bimorphs at three different input frequencies.

3.5 Multiple Bimorph Harvesting System

A decade ago, portable devices such as cell phones were massive, energy hungry creatures that were more of a status symbol than a convenience. Now, the cell phone has become as ubiquitous as a wristwatch and is pushing the limits of available battery technology to shrink the power supply to as small as possible. Lithium ion has become the rechargeable battery of choice for most military and commercial portable devices, but they still cannot go for more than a few days in most applications without needing to be replenished. Therefore, innovative new techniques to recharge or power these devices are being investigated. One such technique is to harvest the necessary power on-the-go from ambient sources, specifically from vibrations involved in the everyday actions of an active human being, using what has been termed a "mobile energy harvesting" (MEH) unit.

3.5.1 Mobile Harvesting - Motivation

This section presents an experimental investigation into the feasibility of mobile energy harvesting using devices that can be worn by humans during everyday activity. This particular device uses two piezoelectric bimorphs which will be discussed in greater detail in subsequent sections. The device is designed to be "minimally parasitic", meaning that it can harvest moderate amounts of energy from human walking without noticeably fatiguing or adding a significant amount of mass loading to the person carrying it.

In terms of wearable energy harvesting devices that employ piezoelectric materials, only a few groups have presented useful research on the topic relevant to the proposed mobile energy harvester. Kymissis et al. (1998) researched the concept of using PDVF and piezoceramics as well as rotary magnetic generators to harvest energy inside of a shoe. The resulting energy measured was roughly 1 milliJoule (mJ) per step for a PVDF and 2 mJ per step for a PZT unimorph device. In 2004, Starner et al [2] analyzed the various sources of power available from human processes. While footfalls are one of the processes, research to date has focused on a device that mounts in the shoe. Nothing presented has posed a device to harvest energy related to the accelerations experienced at the waist level during human gait. Most recently, in 2005, Rome [3] developed an energy harvesting backpack which is capable of generating up to 7 watts of power from average walking. However, the system is not designed to be minimally parasitic, and the amount of input required for such generation often causes fatigue in the human subject, which is counter to the goal of developing such devices. Nevertheless, his calculations are ultimately based on the movement of the hips which are translated to the vertical displacement of the backpack, indicating that the energy available for our proposed harvester is a significant amount, provided the harvested energy is moderate.

3.5.2 Mobile Energy Harvester Theory and Construction

According to Ng and Liao [53], assuming that a piezoelectric bimorph is experiencing a sinusoidal vibration of frequency ω, the voltage source output is equal to the open circuit voltage

$$V_s(t) = V_o \sin(\omega t) \tag{3.5.1}$$

where V_o is the peak open circuit voltage. Using the voltage divider rule, the voltage generated across a load impedance R_L is

$$V_{RL}(t) = \frac{Z_R(s)}{Z_T(s)} V_s(t) \tag{3.5.2}$$

where Z_R and Z_T are the impedance of the resistor and the total impedance of the circuit, respectively. Combining the above two equations, we obtain

$$V_{RL}(t) = \frac{V_o}{\sqrt{\left(1 + \left(R_p / R_L\right)\right)^2 + \left(1/\omega C_p R_L\right)^2}} \sin\left(\omega t + \theta\right) \tag{3.5.3}$$

where

$$\theta = \tan^{-1}\left[\frac{1}{\left(R_p + R_L\right)\omega C_p}\right] \tag{3.5.4}$$

The average power delivered to an impedance load can be found using

$$\left\langle P \right\rangle = \frac{V_{RL(rms)}^2}{Z_L} \tag{3.5.5}$$

Where $V_{RL(rms)}$ is the root mean square (rms) value of V_{RL}. The optimal load impedance can be obtained by taking $\partial\left\langle P \right\rangle / \partial\left\langle Z_L \right\rangle = 0$,

$$Z_L = \frac{\sqrt{1 + \left(\omega C_p R_p\right)^2}}{\omega C_p} \tag{3.5.6}$$

If we assume an ideal piezoelectric model, the internal resistance $R_p = 0$, so the average power output and the optimal load impedance become

$$\langle P \rangle = \frac{V_0^2}{2Z_L\left[1+\left(1/\omega C_p Z_L\right)^2\right]} \quad \textbf{3.5.7}$$

$$Z_L = \frac{1}{\omega C_p} \quad \textbf{3.5.8}$$

Furthermore, assuming that we can use the tip mass to tune the vibration frequency such that $\omega = \omega_n$, then this equation becomes

$$Z_L = \frac{1}{\omega_n C_p} \quad \textbf{3.5.9}$$

Knowing this frequency, we can predict the load impedance that will maximize the power output.

The experimental mobile energy harvesting (MEH) unit consists of two piezoelectric actuators (QP45W) mounted in a clamped-free cantilever configuration inside of a protective case 13.5 x 6.5 x 5.5 cm, as shown in Figure 3.5.1. A tip mass, consisting of a small bolt and several nuts and washers, has been added to the end of each actuator to tune the natural frequency of each harvester closer to that of human walking, around 1 or 2 Hertz. This unit is unique in that the outputs are connected in parallel so that the current output of each actuator adds while the voltage output remains the same. Additionally, connecting the actuators in parallel reduces the overall impedance of the device, which reduces the matching load impedance that is required to maximize the power output. However, for this configuration, it is crucial to consider the polarity of the piezoelectric patches involved as well as the phase of the vibrations for each patch. Wiring the device incorrectly or vibrating the devices out of phase of one another could lead to a cancellation of the overall voltage and current outputs.

The output of the devices is fed through to the outside of the case to a full bridge rectifier. Also on the outside of the unit, a crossbow 3-axis accelerometer is mounted in such a way to measure the vertical, longitudinal, and side-to-side vibrations experienced by the actuators mounted inside.

Figure 3.5.1. Photographs of experimental MEH unit and test subject.

3.5.3 Battery Recharging Experimentation

A small, Panasonic Vanadium Pentoxide Lithium rechargeable battery with a nominal voltage of 3 volts and a 7.0 milliamp-hour capacity was chosen for testing. For control purposes, two batteries were utilized in case one of the batteries was flawed. These rechargeable batteries are slightly different than those mentioned in Chapter 2, as their nominal voltage is lower due to different internal chemistry. However, this chemistry is much more sensitive to the charging rate and to over-charging or over-discharging. It was selected because it was the smallest lithium rechargeable type commercially available at the time of these experiments.

Figure 3.5.2. Photograph of Li-ion battery next to a dime for size comparison.

The batteries were discharged overnight with a 1.5 volt LED, and a baseline was initially recorded. Next, the first battery was connected to the mobile energy harvesting circuitry, and the device was worn by a test subject during a brief 10 minute walk around the campus of Virginia Tech. Some inclines and stairs were encountered during the walk, but the overall path was over flat, paved terrain or grass. Upon returning to the lab, both batteries were immediately connected to an LED. The process was repeated for the second lithium ion battery, following the exact same path and approximately the same pace as the first experiment. The resulting charge and discharge curves are shown in four separate regimes in Figure 3.5.3. Regimes (1) and (3) correspond to the test walks to charge the first and second battery, respectively. Regime (2) shows that the first battery was capable of lighting a small red LED for a few minutes. Regime (4) shows that the second battery was also recharged enough to light an LED. The horizontal line at 1.5 volts represents the LED cutoff voltage. When the supplied voltage is below this line, the LED no longer emits light. The voltage rebound in regimes (2) and (4) is due to removing the LED connection from the battery terminals.

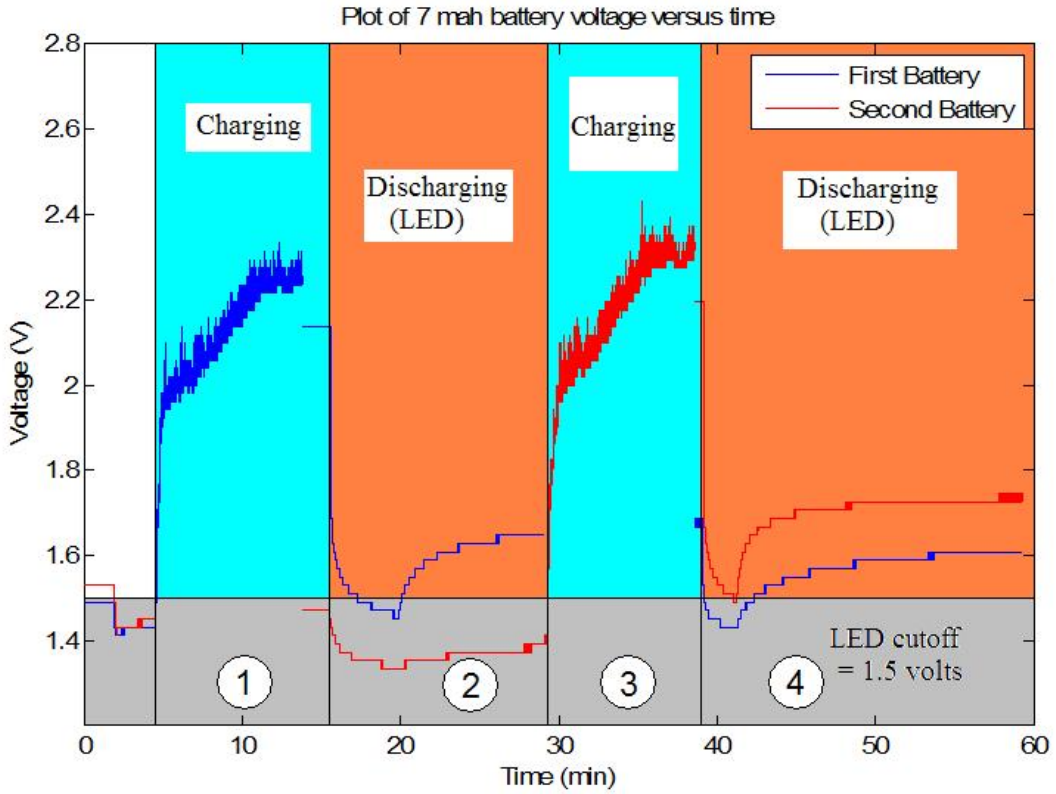

Figure 3.5.3. Charge and discharge curves for each battery during experimentation.

While the battery was not recharged to its nominal capacity of 3 volts, the energy stored from the brief walk was enough to power a small LED for a few minutes. Additionally, the process is shown to be repeatable, as each battery was recharged to sufficiently power an LED. This suggests that by wiring the bimorphs in parallel, their current output is increased to a sufficient level to recharge a battery at least partially, supporting the assertion made in Section 2.4.2. However, the current output is still relatively low, and recharging the batteries to 100% capacity would require several hours of walking with the mobile energy harvester.

3.5.4 Capacitor Charging Experimentation

As introduced in Chapter 2, the simplest of energy harvesting circuits is a capacitor connected to the output of the full bridge rectifier, such that the voltage generated builds up on the capacitor and increases the energy stored within. For testing the energy storage characteristics of capacitors, six different capacitance values were chosen, provided in Table 3.5.1.

Table 3.5.1. Capacitance values used for MEH testing.

Printed capacitance (μF)	Measured capacitance (μF)
33	37.5
220	234
690	695
1000	1041
2000	2020
3300	3070

Figure 3.5.4 is a schematic of the equipment used for testing the charging characteristics of capacitors. In the previous experiment, testing involved attaching the device to a human subject, as shown previously. However, it was of concern that a human subject may not be able to repeat the exact same gait and walking pattern for each charging case. For this experiment, it was crucial to recreate the same input for each capacitor being charged. Therefore, a simulation was devised to create a uniform input to the mobile harvester for capacitor comparison purposes. A step input (amplitude of step) corresponding to 0.85 Hertz was used, which corresponds to the impact experienced at the hip by a human subject during a typical walking stride. The signal was fed through an amplifier and sent to an electromagnetic shaker, and the voltage across the capacitor was measured by the dSpace unit.

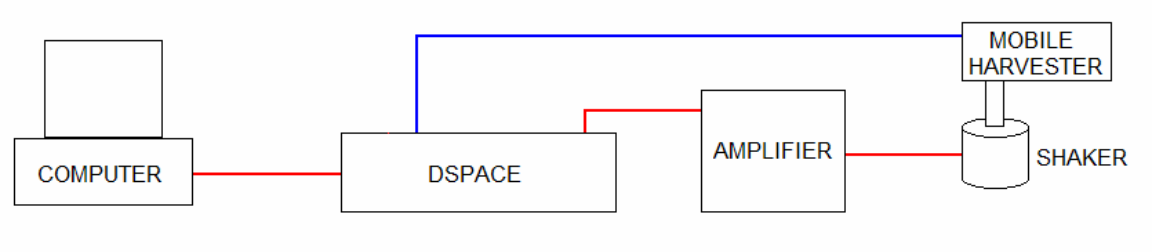

Figure 3.5.4. Diagram of experimental setup for mobile energy harvester.

According to the plots shown in Figure 3.5.5, if one wanted to harvest the maximum amount of energy in a 70 second interval of time, then a 2000 μF capacitor would be best suited for the application. On the other hand, if the interval of time is increased to 140 seconds, then a 3300 μF capacitor becomes the best choice. By specifying the duty cycle of the device to be powered, the optimum capacitance can be chosen for the application.

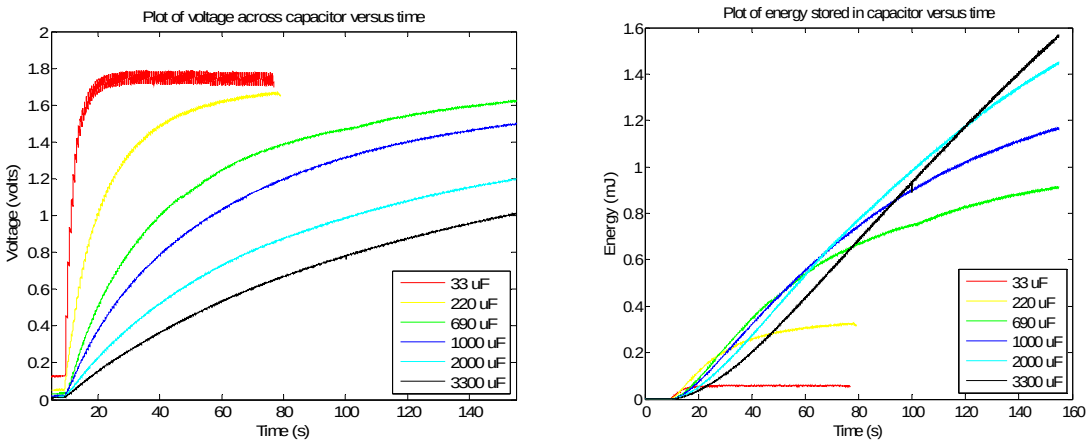

Figure 3.5.5. **Plots of voltage and stored energy, respectively, for six different capacitors.**

From Figure 3.5.6, it appears that as the capacitance increases, the rate of energy storage increases asymptotically towards an upper limit. It can also be seen that given a specified amount of time, a specific capacitance value can be selected to maximize the rate of energy storage. The general trend is that the longer amount of time available to harvest energy, the larger the storage capacitor should be sized.

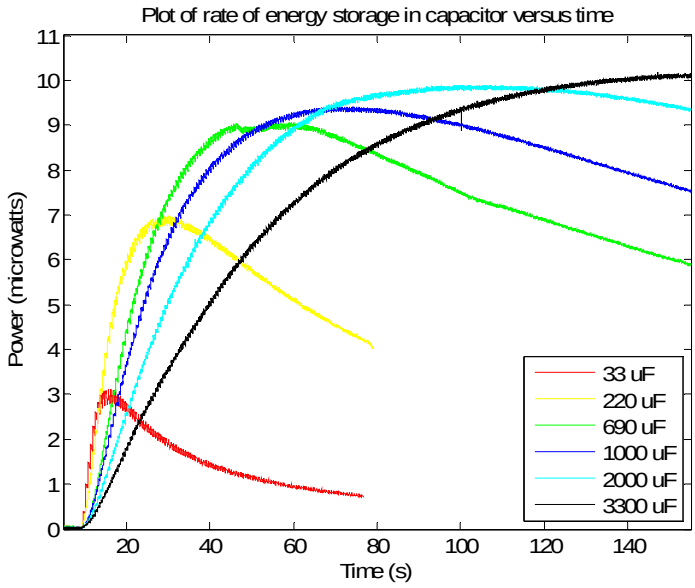

Figure 3.5.6. Plots of rate of energy storage (power) in various capacitor sizes versus time.

While the input energy from the piezoelectric harvester is constant, the amount of energy stored begins to level off and the rate of energy stored in the capacitor starts to decrease. This is explained by the equilibrium point reached when the voltage on each capacitor is significantly large. The energy loss or dissipation from a capacitor is related to the voltage by

$$E_{loss} = \frac{1}{2} C\left(V_i^2 - V_f^2\right) \qquad \textbf{3.5.10}$$

where E_{loss} is the energy lost, C is the capacitance, V_i is the initial voltage on the capacitor and V_f is the final voltage on the capacitor. From this equation, it is evident that as the voltage on the capacitor gets larger and larger, the amount of energy lost through leakage becomes greater and greater, countering the energy being input into the capacitor.

Figure 3.5.7 shows real storage capacitors are not ideal, and there is a voltage leakage due to internal resistive losses. Therefore, it is also crucial to consider the amount of time the storage device will be idle, neither delivering energy to a load nor absorbing from an ambient source. For example, while the 33 µF capacitor charged to a voltage that was approximately 1.4 times greater than that of the 2000 µF capacitor, its voltage quickly decayed to below one volt within 8 seconds of halting the energy input, while the 3300 µF capacitor maintained a voltage of over one volt for 150 seconds of standby time.

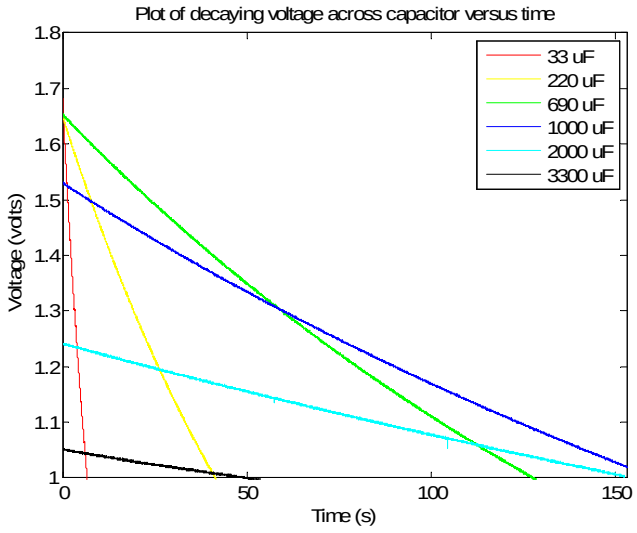

Figure 3.5.7. Plots of voltage decay after charging source has been removed.

These results confirm that the mobile energy harvester is capable of storing the harvested electrical energy in electrolytic capacitors of various sizes, although the leakage effects of the storage devices cannot be neglected.

3.5.5 Conclusions and Future Work

The feasibility of charging a small lithium ion battery and several micro- to milli-Farad capacitors using vibrations associated with walking has been investigated. The first experiment confirmed that a lithium ion battery can be successfully recharged, although the length of time that the energy was harvested was not sufficient to recharge a battery to full capacity. The second experiment demonstrated that the rate of energy stored in a capacitor varied between 3 and 10 microwatts and that the amount of energy that could be stored within a particular timeframe of walking could be maximized by correctly sizing a storage capacitor. Overall, this section confirms that a hip-mounted device employing piezoelectric materials is a viable method of harvesting ambient energy from human walking. Further investigations will be performed into shrinking the overall size of the device and increasing the amount of energy extracted.

Chapter 4 – Thermoelectric Generators

4.1 Electrical Modeling of Thermoelectric Materials

The ability to convert thermal energy into electrical energy is facilitated by a special material property known as the Seebeck effect. The Seebeck effect is a phenomenon that occurs when a voltage (V) is induced in proportion to an applied temperature gradient (ΔT) related by

$$V = \alpha \Delta T \qquad \textbf{4.1.1}$$

where α is the Seebeck coefficient. This relationship is exploited most often for the purpose of temperature measurements, but can also be used on a larger scale to develop a high enough voltage and current output to run different devices and sensors or even to charge a small battery [73].

A thermoelectric generator (TEG) is easily modeled as a DC voltage source in series with an internal resistance, as can be seen in Figure 4.1.1. The power delivered is maximized when the load resistance or impedance is equal to the internal resistance of the TEG. For the case when R_{load} is a battery or a capacitor being charged, a diode must be included in this circuit between the generator and the load to prevent a backflow of energy from the battery to the thermoelectric generator when ambient energy is not being harvested.

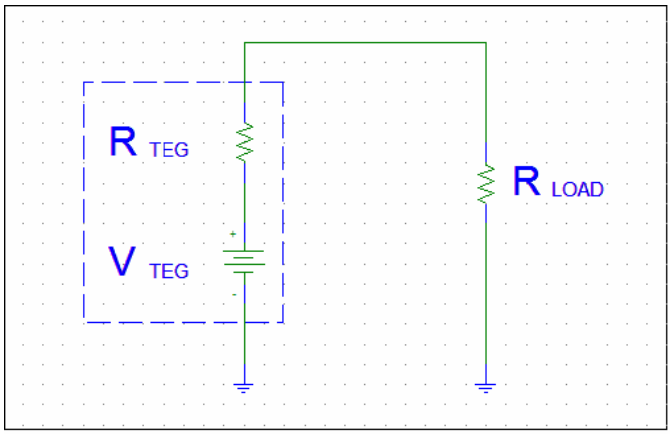

Figure 4.1.1. Electrical equivalent model of a thermoelectric generator device.

The calculated power output P_i based on the "ideal" model shown in Figure 4.1.2 is

$$P_i = \frac{(2\alpha\Delta T_o)^2}{4R_{TEG}} \quad \textbf{4.1.2}$$

Where α is the Seebeck coefficient, ΔT_o is the temperature difference across the thermoelements, and R_{TEG} is the total series electrical resistance, given by

$$R_{TEG} = 2n\rho\left(\frac{L_o}{A_o}\right) \quad \textbf{4.1.3}$$

Where ρ is the electrical resistivity, n is the number of thermoelement pairs, and L_o / A_o is the ratio of the thermoelement length to cross sectional area.

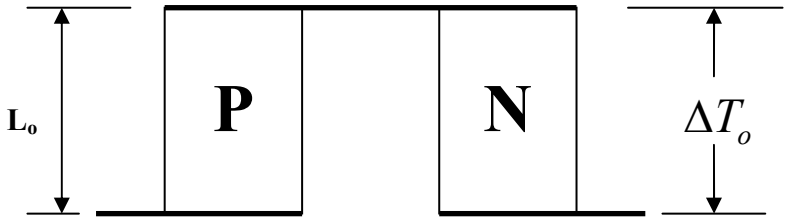

Figure 4.1.2. Schematic of ideal Peltier device (adapted from [64].)

The thermocouple shown in Figure 4.1.2 consists of a "P" branch which has a positive Seebeck coefficient, α, and an "N" branch with a negative α, joined by a thin metal interconnect with a very low α, typically assumed to be zero [56]. For bulk thermoelectric generator materials based on bismuth telluride (Bi_2Te_3) at 300 K, the n-type material has a Seebeck coefficient of -202 μV/K and the p-type material has a Seebeck coefficient of 214 μV/K [86].

4.2 Battery Recharging Using Ambient Thermal Gradients from Automotive Exhaust

With improvements in production of bulk thermoelectric materials and relatively low operating temperatures, TEGs are being investigated for automotive applications.

The internal combustion engine in automobiles is highly inefficient, and much of the energy is transformed into waste heat which dissipates to the environment. According to Yang [89], from 100% of energy produced by an internal combustion engine, 40% of the energy generated is dissipated through exhaust. If even a small fraction of this energy could be reclaimed, it could be used to run electronics and reduce the electrical loading on the engine.

This investigation seeks to determine the feasibility of using waste heat from a common, personal-use vehicle to recharge a nickel metal hydride battery. The vehicle chosen was a late model Saturn Ion, and the mounting location was the bottom of the catalytic converter, shown in Figure 4.2.1. Using an infrared, non-contact thermometer, the outside temperature of the catalytic converter at idling conditions was measured to be 155 ^{o}C. The measurement device was held approximately 1 ft away from the heat source, so the measurement should be a reasonably accurate prediction of the catalytic converter temperature.

Figure 4.2.1. Photograph of automobile and mounting location of TEG device.

4.2.1 Thermoelectric Generator Device Characterization

The first objective was to size and characterize a device to harvest power. Commercially available Melcor ® high temperature thermoelectric coolers, capable of operating in environments up to +225 ^{o}C, were chosen as the harvesting device. Four of the devices, which measured 3 cm x 3 cm x 0.36 cm, were connected electrically in series such that their voltage outputs would add. High temperature silicon gasket material was

injected into each TEG to decrease heat leakage between the two ceramic faces. To improve and ensure heat transfer, a flat aluminum plate was mounted to the hot side of the generators and an aluminum fin heat sink was attached to draw heat away on the cold side.

Figure 4.2.2 is a plot of ΔT versus time on the left y-axis and the TEG voltage versus time on the right y-axis. As can be seen from the near overlap from simply scaling the axes, the relationship between ΔT and voltage is fairly linear. The linear fit in Figure 4.2.3 confirms this assumption, although the relationship deviates from a straight line at very small temperature differentials.

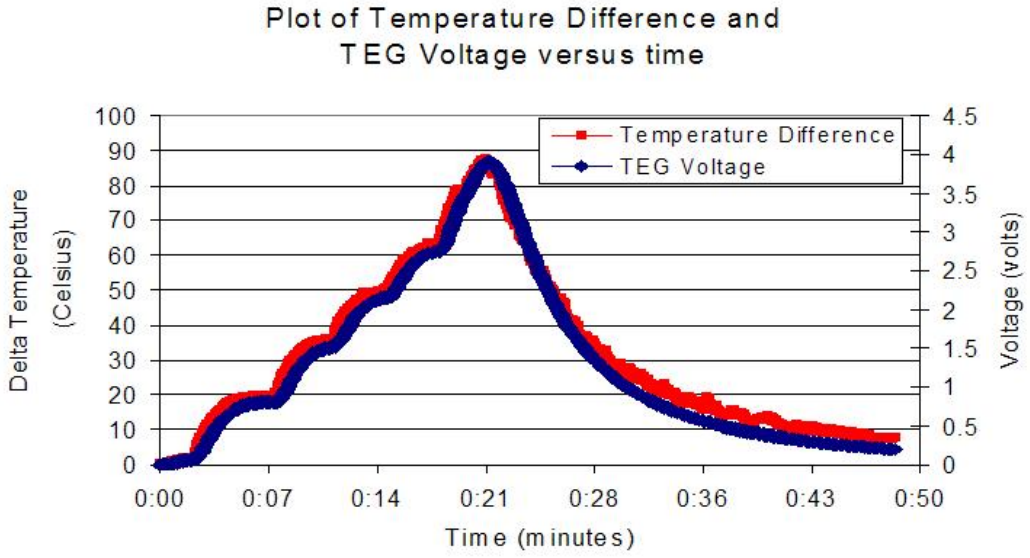

Figure 4.2.2. Plot of ΔT on left y-axis and plot of TEG voltage on right y-axis versus time.

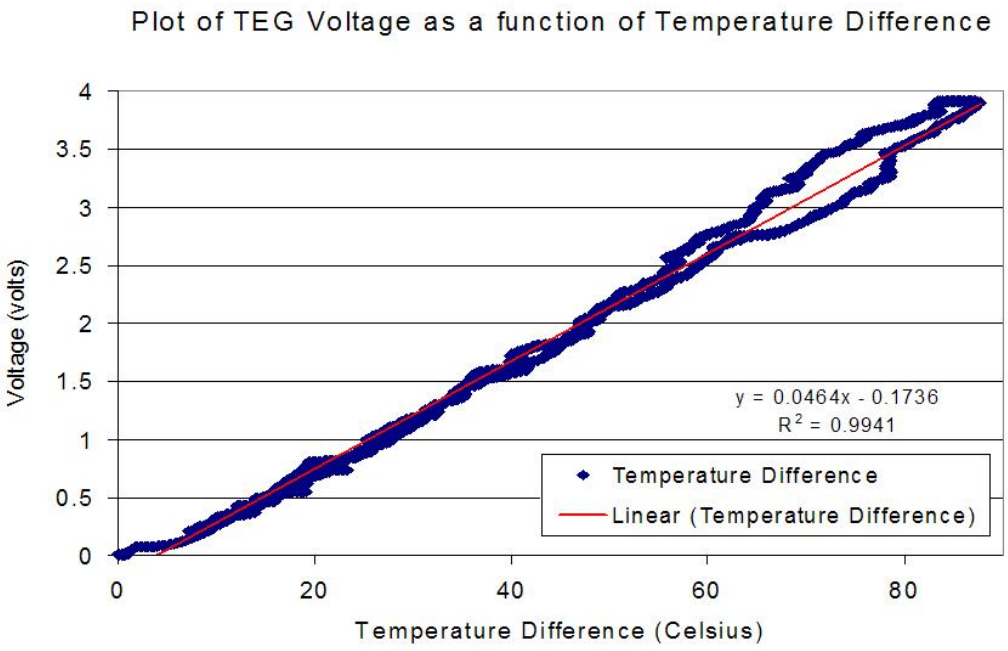

Figure 4.2.3. Plot of TEG output voltage as a function of ΔT.

4.2.2 Automotive Harvesting Experimentation

Due to manufacturing limitations, thermoelectric generators are constructed with flat profiles. However, the surface of the catalytic converter is rounded, so an aluminum interface adapter was constructed. Figure 4.2.4 is a rendition of the entire harvesting device, including the heat sink to dissipate heat from the cold side of the thermoelectric generators. Thermal grease was used between the thermoelectric devices and each aluminum block to increase thermal conductivity. Since typical permanent magnets or two part epoxies would fail at such high temperatures, a piece of wire was wrapped around the device and the exhaust pipe several times and twisted with pliers to hold the TEG device flush against the hot metal surface for the greatest amount of thermal transfer.

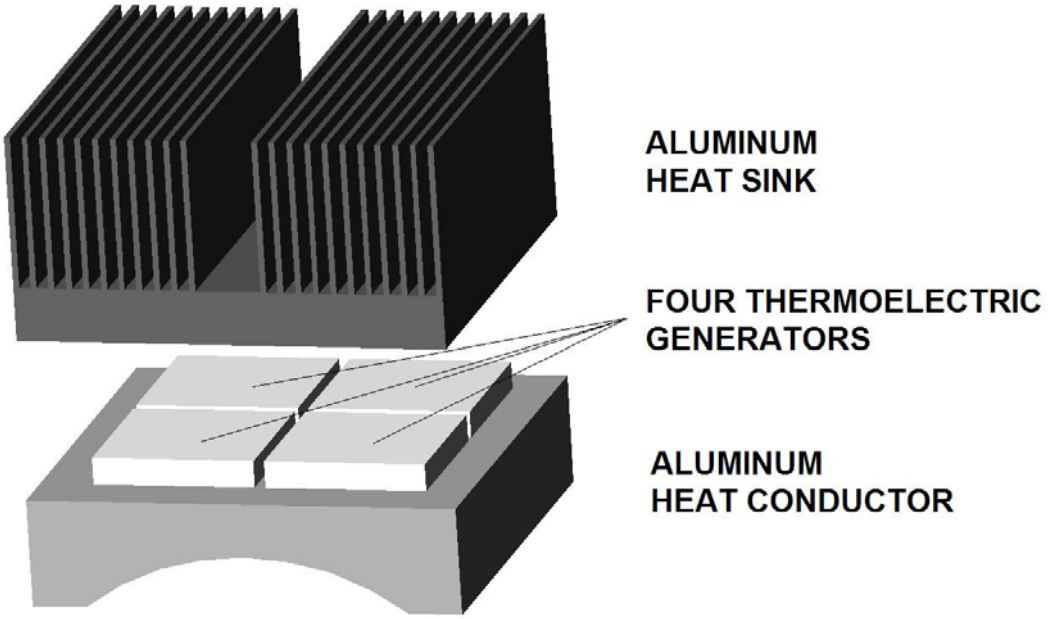

Figure 4.2.4. AutoCAD drawing of the thermoelectric generator device, including heat sink and aluminum piece to adapt to vehicle exhaust system.

A ReadyDaq data acquisition system capable of measuring 0-5 volt inputs was used for recording data. The first experiment involved turning the car on and letting it idle for 20 minutes and then turning it off, while the second experiment involved a short drive around the town of Blacksburg, Virginia, with speeds ranging from 25 to 65 miles per hour. The reason for using a smaller resistor for the experiment where the car was running is that the voltage limit of the data acquisition system is 5 volts. The results of both experiments are plotted in Figure 4.2.5.

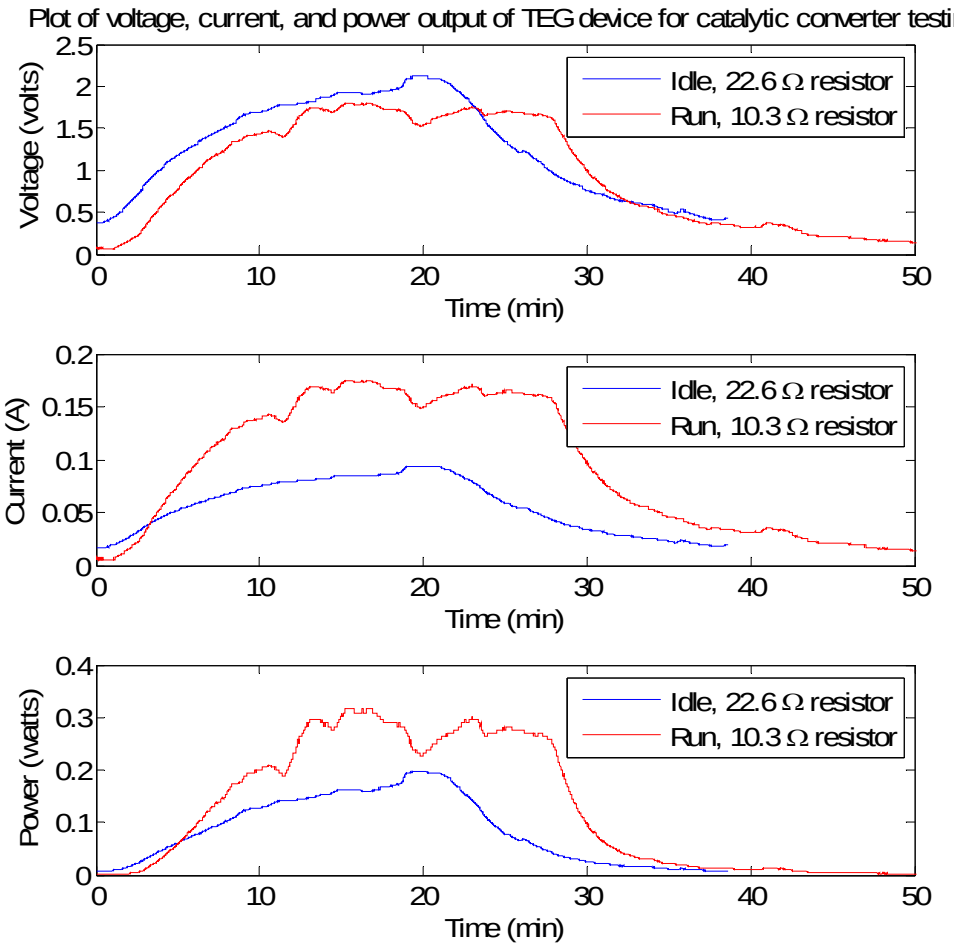

Figure 4.2.5. Plot of the TEG voltage, current, and power output versus time during automotive testing.

The maximum power output was 198.4 mW during idling conditions and 316 mW during the road testing. Additionally, across the 10.3 Ω resistor, the voltage was greater than 1.5 volts and the current was about 150 mA under normal operating conditions, suggesting that the device could be used to recharge a moderately sized NiMH battery. Therefore, two more tests were performed to explore the possibility of recharging batteries using the thermal gradient from the automobile. The same data acquisition system as before was used, and the car was driven on similar roads as before for 15 to 30 minutes. As can be seen in Figure 4.2.6, the system successfully recharged both a 80 mAh and a 300 mAh battery.

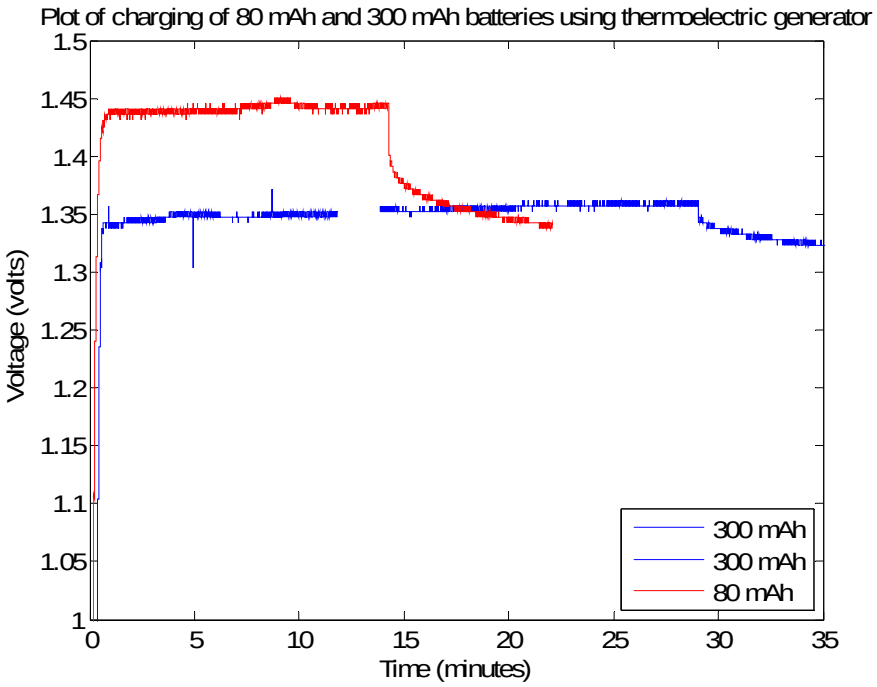

Figure 4.2.6. Voltage versus time for 80 and 300 mAh NiMH batteries charged using TEG device.

The results presented here confirm that automotive exhaust thermal gradients can be used with low temperature thermoelectric generators to produce up to 314 milliwatts of power during typical highway driving. Furthermore, it was shown that the electrical power generated could successfully recharge an 80 and a 300 mAh nickel metal hydride battery.

4.3 Innovative Charging Circuit Using Electronic Switches

Most devices on the market today have switched to using lithium ion batteries as their power source, which have a nominal voltage of 3.6 volts and a full charge voltage of 4.2 volts. However, thermoelectric generators are characterized by their high current, low voltage output. As many newer electronic devices are designed to operate at a higher voltage, several thermoelectric generators must be put together in series just to step up

the voltage output to a useable level. Linking four standard thermoelectric devices from Melcor® in series, a temperature difference of approximately 85°C is required to generate an open circuit voltage of 4.0 volts. Therefore, it would take a device three times the size of the present device to charge a lithium ion battery.

As an alternative, an innovative charging circuit for NiMH batteries has been proposed. Nickel Metal Hydride (NiMH) batteries, in contrast to lithium ion batteries, have a nominal voltage of 1.2 volts and a 1.5 volt full charge voltage. The proposed concept uses an innovative charging circuit that would allow the thermoelectric device to charge three NiMH batteries in parallel at a voltage of 1.5 volts, shown in Figure 4.3.1. Figure 4.3.2 is a photograph of the four relays to be used for the device. They are Omron G6HK-2-5-VDC double-coiled latching relays with two sets of switches. Each relay measures 1.4 cm x 0.85 cm and stands 0.5 cm tall from the breadboard.

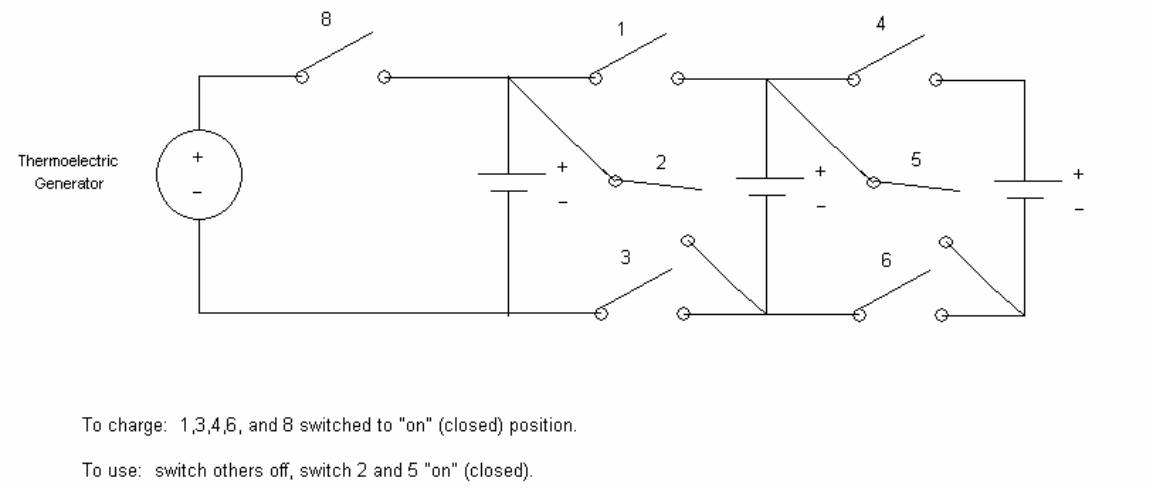

Figure 4.3.1. Electrical Schematic of switching circuit.

To charge the batteries, switches 1, 3, 4, 6, and 8 are switched on. A “delta voltage” algorithm would be employed to determine when the batteries had been recharged to a satisfactory level. Once each battery reached this voltage, the previously mentioned switches turn to their off position and 2 and 5 move to their on position to

connect the batteries in series, providing a 3.9 volt power source that would interface with devices designed to operate at the voltage of a Li-ion cell. Once the voltage of the series of NiMH batteries dropped below 3.3 volts, the circuitry would once again connect the batteries in parallel and reconnect to the charging device.

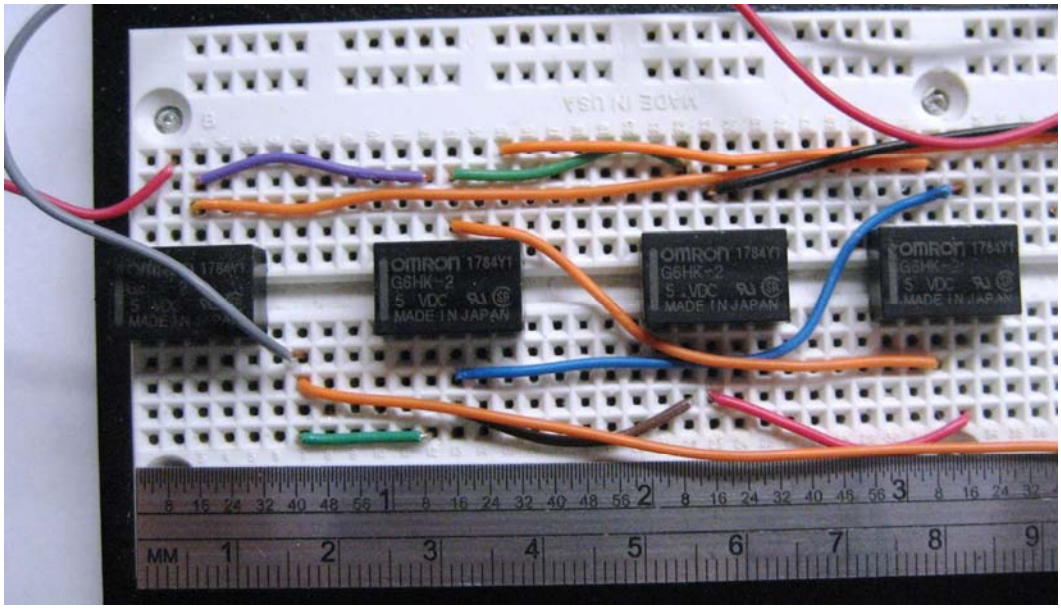

Figure 4.3.2. Photograph of switching circuit.

While the circuit was built and tested, a simpler but less sophisticated algorithm of measuring only the voltage output was employed, leading to unexpected and undesirable switching between charging and discharging configurations. Instead of developing a more advanced algorithm suited to battery charging, research into a low power DC/DC converter was performed, as described in the following section.

4.4 Low Power DC/DC Converter for Thermoelectric Charging of Lithium Ion Batteries

As stated previously, even four commercially available generators linked in series experiencing a ΔT of 30 ^{o}C can only reach a maximum voltage output of 1.5 volts. This is large enough to recharge a 1.2 volt battery, but most present day electronics run off of

a lithium ion battery, rated at 3.6 volts. As an alternative, a high efficiency DC-DC converter could be used to modify the output to produce a larger voltage.

The device chosen for experimentation was a National Semiconductor evaluation board for LM2621, a low input voltage, step-up DC-DC converter, shown in Figure 4.4.1. Without the special red, green and black banana plug connectors, the board would be much smaller, about 1.5 cm x 1.7 cm x 0.4 cm.

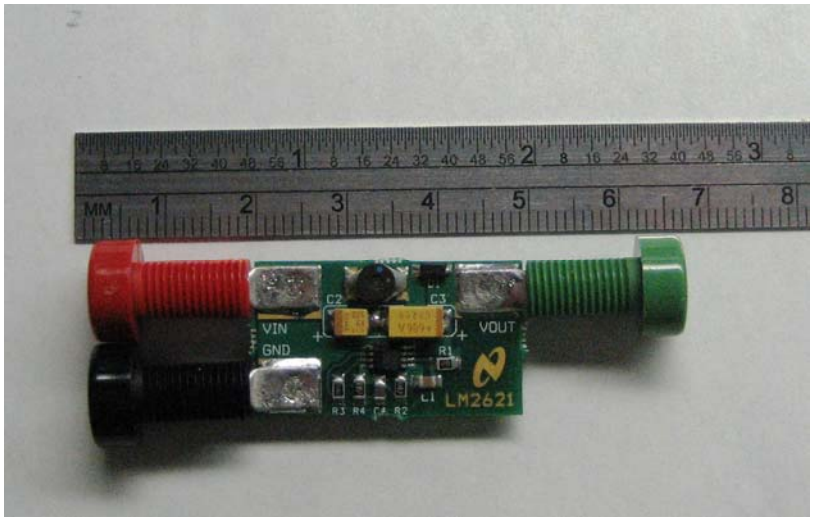

Figure 4.4.1. Photograph of LM2621 evaluation board.

For the first trial, the input and output voltages were measured and plotted, shown in Figure 4.4.2. While the exact temperature differential was not measured, it is estimated that the TEG generates approximately 1.5 volts when the ΔT is about 35 ^{o}C, as predicted by Figure 4.2.3 from earlier in this chapter. When the input of the converter reaches 1.21 volts at 450 seconds, the output of the converter increases to an average value of 4.88 volts. In reality, the output oscillates between 4.84 and 4.92 volts. Between 600 and 700 seconds, a 460 ohm resistor was attached across the DC/DC converter output. In the region between approximately 800 and 1100 seconds, the DC/DC converter was disconnected to analyze the output of the TEG configuration alone. Overall, the DC/DC converter proved successful in stepping up the TEG output voltage, justifying further experimentation.

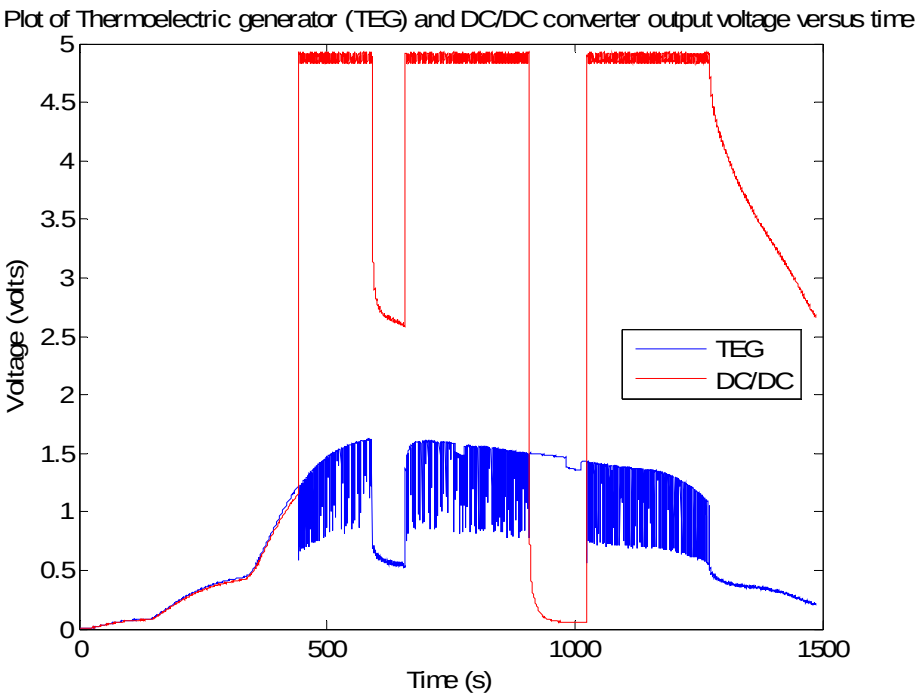

Figure 4.4.2. Plot of input and output voltages of DC/DC converter test board.

The objective of further testing was to characterize the DC/DC converter. Figure 4.4.3 is a plot representing the output of the DC/DC converter as a function of the temperature difference. It appears that for voltage differences greater than 30 degrees Celsius, the DC/DC converter will operate correctly. Figure 4.4.4 demonstrates the benefits of the DC/DC converter. For a steady ΔT of between 30 and 35 ^{o}C, a 1 Farad capacitor can only charge up to 1.39 volts, regardless of the amount of time it is allowed to charge. For the same ΔT, the output of the DC/DC converter can charge the same capacitor up to 3.15 volts, as can be seen in Figure 4.4.4. Theoretically, given enough time, the DC/DC converter could charge any size capacitor up to its maximum output of 4.88 volts.

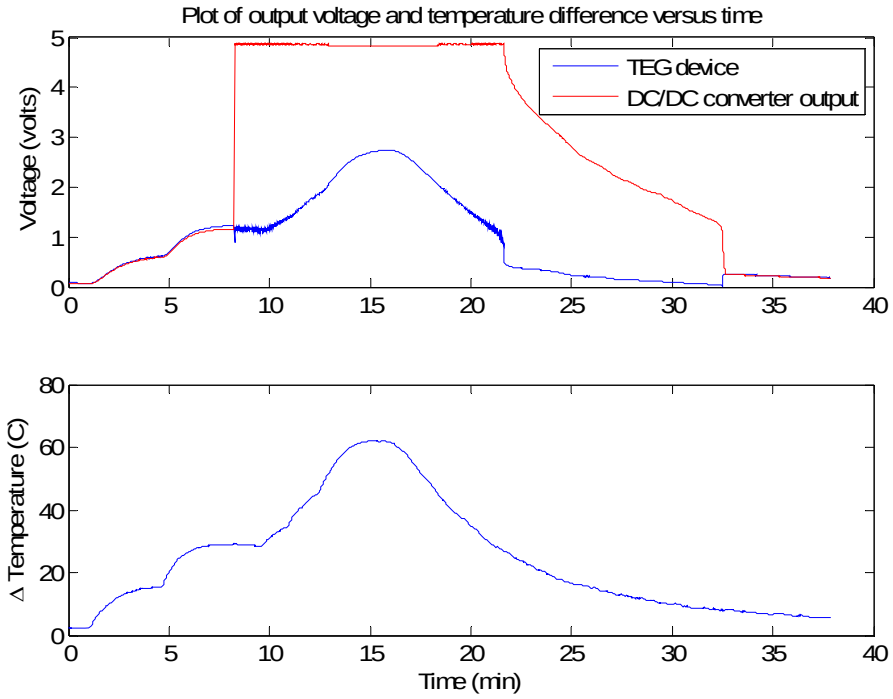

Figure 4.4.3. Plot of input and output voltages of DC/DC converter and ΔT of TEG device.

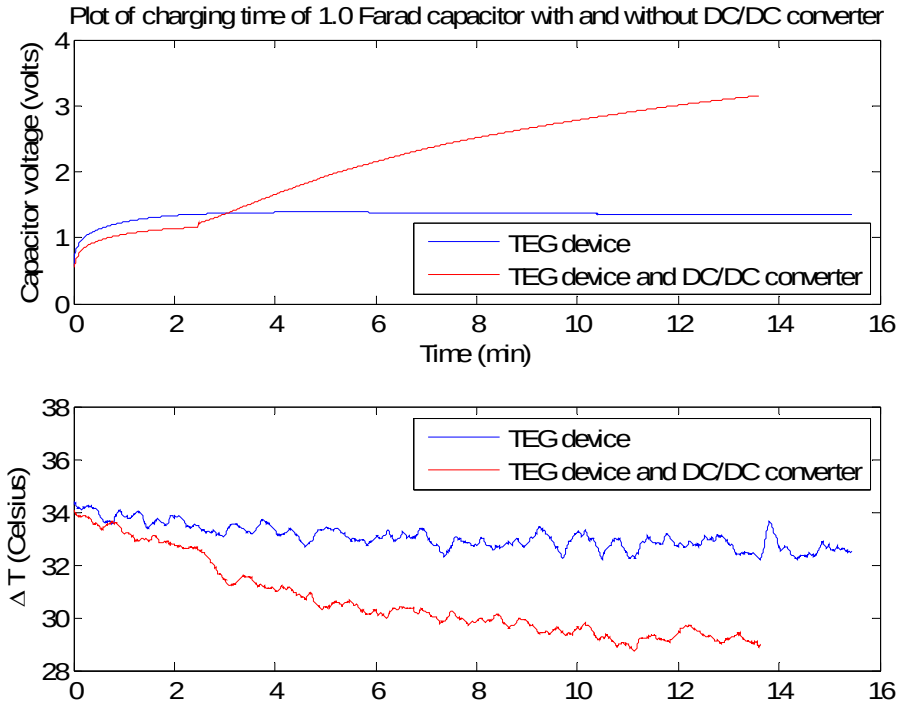

Figure 4.4.4. Plot of capacitor voltage and ΔT for charging using the TEG with and without the DC/DC converter.

These results reveal that a low power DC/DC converter is capable of self starting using the electrical power generated from a thermoelectric generator. The DC/DC converter can start with input voltages as low as 1.25 volts and output up to 4.88 volts. The thermoelectric device used previously in the automotive exhaust testing can supply a sufficient input voltage when it experiences a ΔT of at least 30 ^{o}C. The converter output can then be used to charge a supercapacitor to a voltage up to two times higher than the direct output of the generator.

4.5 Switching Circuit versus DC/DC Converter Comparison

The switching circuit design requires a mechanical switching when the batteries reach a predetermined voltage, which requires additional circuitry to sense this voltage threshold. The DC/DC converter, on the other hand, is self starting, meaning that the output automatically increases to a higher voltage when the input from the thermoelectric reaches a minimum threshold. This action does not require sensing of the input voltage.

Additionally, the switching circuit will always require a voltage of greater than 1.5 volts to recharge the individual NiMH cells, while the voltage input requirements for DC/DC converters continues to drop to levels of 0.3 volts and lower [19]. For space constrained designs with short duty cycles, such as for wireless sensor applications, the DC/DC converter design allows for less thermocouple models and smaller electronics to achieve a high voltage. Finally, while the switching circuit is still only in the preliminary stages and only introduced as a concept in early 2002, the DC/DC converter for such applications has been thoroughly studied since at least the early 1990s, and is already at the commercial production stage.

In applications where supercapacitors are not powerful enough and lithium ion safety issues are a concern, then the NiMH switching circuit would provide a safe alternative solution. However, in order for the circuit to work correctly, a more sophisticated algorithm would be needed, which may consume too much power to justify the switching circuit. In such a situation, it may be easier to have switches that simply change position after a preset amount of time.

Chapter 5 – Hybrid Generator Concept

In this chapter, two other transducer types, photovoltaic and electromagnetic, are introduced and electrically modeled. Next, a comparison of the experimental results from previous chapters to results found in literature is presented, as well as a discussion of the relative power densities of all four transducer types is discussed.

The final section of this chapter proposes a hybrid generator device. A hybrid generator is defined as a single device that uses a combination of transducer types to harvest energy from either one or multiple ambient energy sources. The device proposed utilizes both piezoelectric and electromagnetic transducers to harvest from ambient vibration energy, which falls under the definition of a hybrid device.

5.1 Electrical Modeling of Photovoltaic Materials

A photovoltaic cell can be considered as a two terminal electronic device which conducts like a diode in the dark and generates a photovoltage when charged by the sun or some other solar source [52]. First-order solar cell modeling shows that the current generated by a solar cell can be described by

$$I = I_{sc} - I_0\left(e^{\frac{V}{V_T}} - 1\right) \tag{5.1.1}$$

where I_{sc} and I_0 are related to the current densities J_{sc} and J_0, respectively, by

$$\begin{aligned} I_{sc} &= AJ_{sc} \\ I_0 &= AJ_0 \end{aligned} \tag{5.1.2}$$

where A is the area of the photovoltaic device, J_{sc} is the short circuit current density and J_0 is the dark current density. For circuit simulation purposes, a solar cell is therefore most often modeled as a current source with a value of I_{sc} in parallel with a diode, as shown in Figure 5.1.1 [14]. The reason for modeling as a current generator is due to the

fact that, for all but the largest loads, the current draw is independent of the load resistance [52].

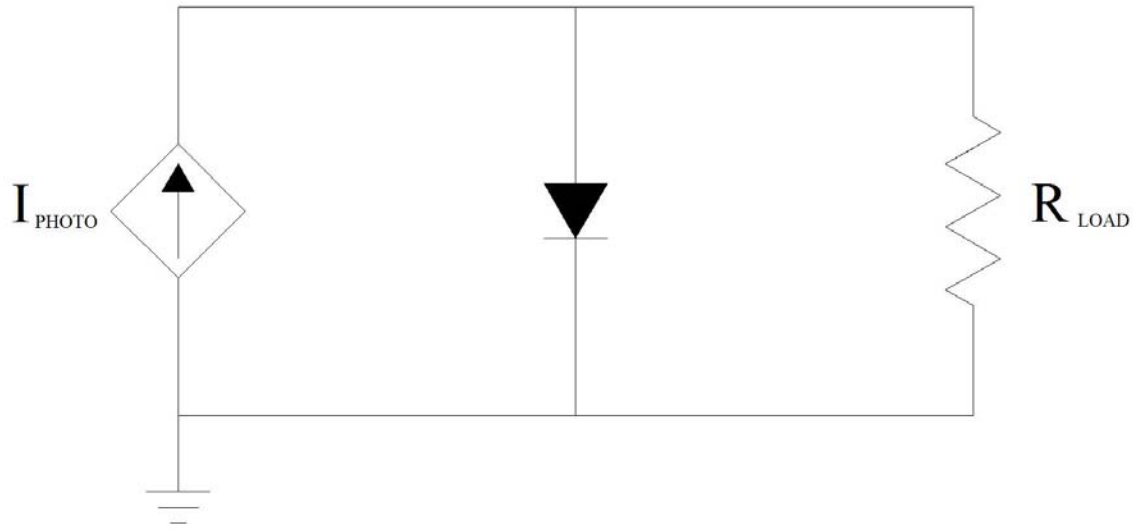

Figure 5.1.1. Electrical model of a solar cell as a current source in parallel with a diode with a load resistance attached.

It must be taken into account that the internal resistance of solar cells is not a constant, but rather a function of solar source intensity and the current draw [16]. And unlike batteries, whose internal resistance ranges from about 0.7 to 1.2 ohms, solar cells have a much wider internal resistance range of 10 to 10,000 ohms [16].

5.2 Electrical Modeling of Electromagnetic Generator

An electromagnetic generator can be modeled in a similar manner to that of a piezoelectric generator, except the internal impedance is inductive rather than capacitive in nature. Therefore, it is modeled as an AC voltage source in series with an inductor and a resistor, as shown in Figure 5.2.1. The losses incurred internally are often referred to as a back electromotive force (EMF), although in actuality it is not a force but a potential voltage difference.

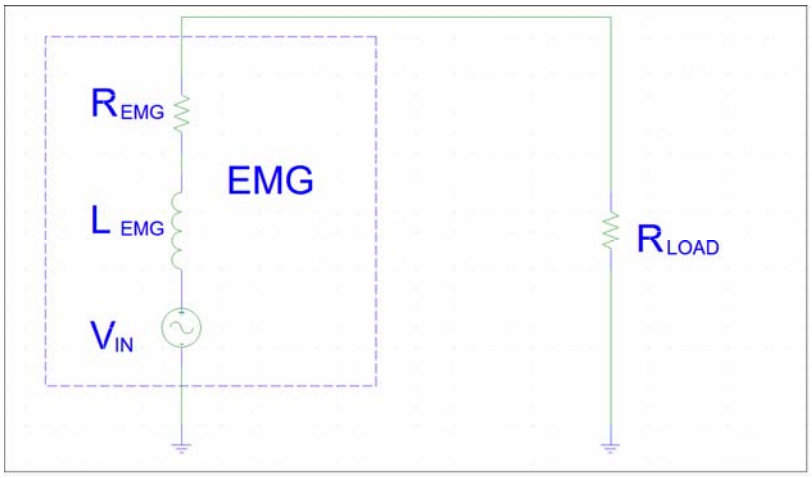

Figure 5.2.1. Electrical Schematic of electromagnetic generator attached to a load.

Since this type of generator, like a piezoelectric one, produces an AC voltage output, the signal must first be sent through a rectifying circuit as described in Chapter 2 before it can be useful for most applications. A more detailed derivation of the equations will be provided in the following sections of this chapter.

5.3 Comparison of Harvesting Techniques

Table 5.3.1 provides power density values obtained experimentally during laboratory testing. The power is calculated per area rather than volume or mass because the available density values reported in literature are reported in this manner. However, for accurate predictions of device sizes for small scale applications, a density in terms of volume or mass rather than area would be more useful.

Table 5.3.1. Comparison of power density based on experimentation.

Harvesting Method	Current Output Range	Voltage Output Range	Power Output Range
Piezoelectric Active area = 17.4625 cm^2	10 – 100 µA	1 – 10 V	3 – 7 $\mu W/cm^2$
Thermoelectric ($\Delta T = 30\ ^oC$) Active area = 36 cm^2	10 – 25 mA	0.1 – 1.0 V	86 – 225 $\mu W/cm^2$

The piezoelectric power density is fairly low in comparison to the 200 μW per cm^2 reported by Torres et al [81], which is attributable to a lower amplitude vibration level and to operation at frequencies other than resonance. The thermoelectric power density appears to be much higher than those reported by Torres et al [81], but since the temperature gradient is three times larger, and power scales up as a function of the square of the temperature gradient, then these values fall within accepted levels. No experimental data was obtained for solar cells, but Torres et al [81] reports widely varying power density values of between 10 μW to 15 mW per cm^2, depending upon an indoor or outdoor light source.

5.4 Piezoelectric and Electromagnetic Hybrid Generator

As mentioned in Chapter 3, most piezoelectric energy scavenging devices utilize a "proof mass" to tune the cantilever beam to a desired frequency. While it does help to increase strain in the piezoelectric material, the proof mass adds useless mass to the energy harvesting device, which lowers the energy density of the device when all factors are considered. This mass could be utilized to further harvest power from the environment using electromagnetic coupling to scavenge power from a moving magnet.

The test setup is shown in Figure 5.4.1. Not shown is the dSpace data acquisition system used to record the voltage outputs and the base acceleration. The device utilizes the piezoelectric patches and the magnet – copper coil system harvest energy from vibrations provided by the electrodynamic shaker.

Experimentally, the first natural frequency of the bimorph was determined to be 27.5 Hertz. The piezoelectric bimorph weighs approximately 10.3 grams with an active area mass of 9.1 grams and the magnet weighs 26.1 grams. According to the equations for a cantilever beam with a tip mass from Chapter 3, the first natural frequency is predicted to be 31.26 Hertz, resulting in a 12.0 % error. The copper coils, which are separate from the vibrating device, weigh about 80 grams.

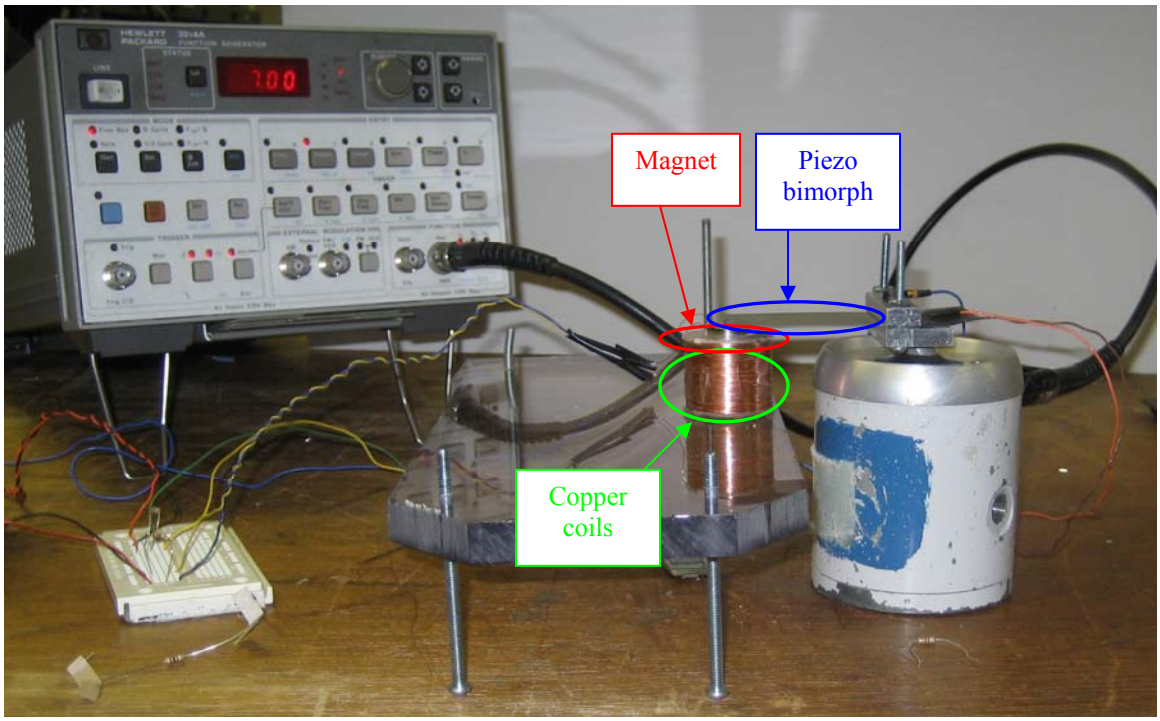

Figure 5.4.1. Photograph of electromagnetic-piezoelectric harvester hybrid test setup.

Figure 5.4.2 is a plot of the power output of both the piezoelectric bimorph and the electromagnetic harvester as a function of the electromagnetic load resistance. The green points are the piezoelectrically generated power, the blue points represent the electromagnetically generated power, and the red points are the total power harvested. The power output is relatively low because the base acceleration measured was only ± 0.2 g during the course of experimentation.

When the load resistance is too small, neither system harvests much energy. However, as the load resistance is increased, a characteristic power curve is observed, with an optimal load resistance somewhere between 115 and 125 ohms. From the data concerning the piezoelectric harvester section of the device, the power output across the 47 kΩ resistor asymptotically approaches a power output of approximately 60 μW as the load condition of the electromagnetic system approaches an open circuit condition. When the coils are completely removed, the piezoelectric with the magnetic tip mass generated 84.28 μW of power.

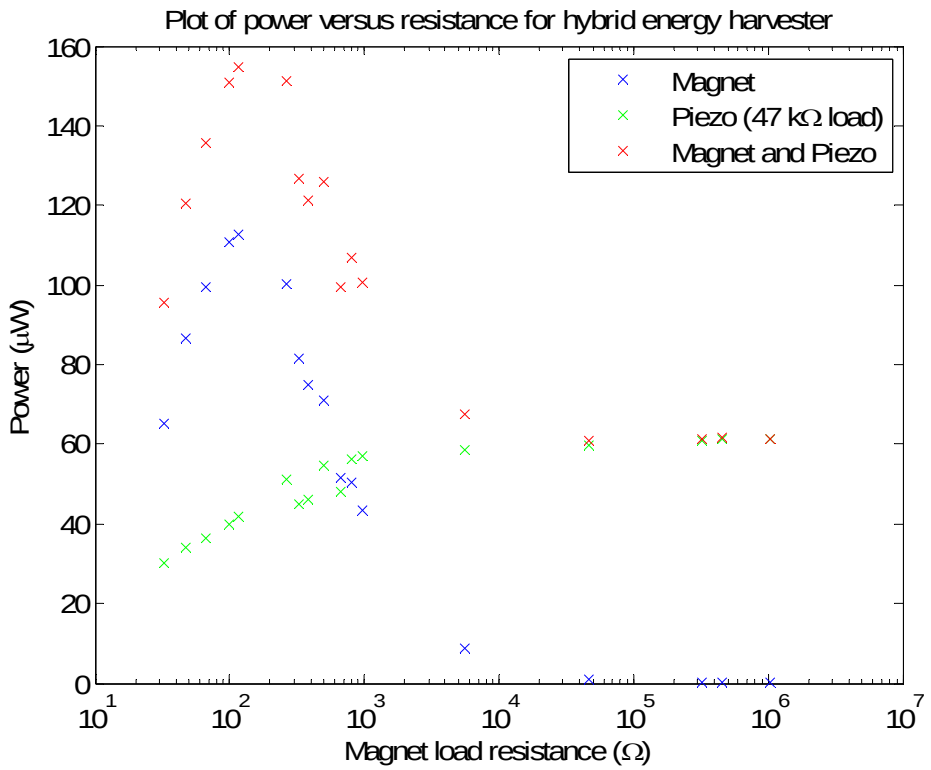

Figure 5.4.2. Plot of power output versus electromagnetic load resistance for both harvesting techniques.

By themselves, the electromagnetic harvester can harvest a maximum of 112.87 μW and the piezoelectric harvester can harvest a maximum of 84.28 μW of power. Together, they can harvest a maximum of 154.9 μW under optimal conditions, an increase of 137.2% over the electromagnetic harvester alone and 183.8% over the piezoelectric harvester alone.

Chapter 6 – Conclusions

6.1 Brief Summary of Thesis

Chapter 2 introduces the electronic components and storage devices involved in rectifying the alternating voltages produced by piezoelectric and electromagnetic transducers. While active electronic components are an area of ongoing research, the majority of the chapter is limited to the scope of passive components relevant to successfully storing harvested energy. The most recent advances in battery and capacitor storage technology are presented with specific focus on supercapacitors. An investigation into the effectiveness of battery charging by piezoelectric devices is included which suggests that the microamp level output of small piezoelectric transducers is insufficient to recharge a battery within a reasonable time frame. Despite technological advances, however, the best supercapacitors are still at least an order of magnitude smaller than batteries in terms of energy density, although they have a relatively high power density in comparison to batteries.

Chapter 3 presents a piezoelectric harvester model as a voltage source in series with an internal capacitance and resistance. Specifically, a simple model of a cantilever bimorph is introduced and parametrically studied to determine the effects of a proof mass on the first natural frequency of the bimorph. The model is verified using a Piezo Systems, Inc. T226-A4-503X with good agreement with experimental results. The bimorph is then tested at its first natural frequency to examine the power output as a function of the load resistance. By combining two devices in parallel, it is observed that the power output roughly doubles and the optimal load resistance is halved, which verifies the first electrical model introduced. In comparison to the Piezo Systems bimorph, which is a monolithic device, Chapter 3 also explores the possibility of energy harvesting using active fiber composites and macro fiber composites (MFC). Active fiber composites are similar to macro fiber composites, except that the fibers are extruded rather than sliced from a monolithic piezoceramic. The benefit is that it is easier to

produce, but the interdigitated electrodes used increase the voltage output at the sacrifice of current output, leading to poor battery charging capability. Macro fiber composites have previously been examined for their d_{33} coefficient, but new developments have led to MFCs which utilize the d_{31} coefficient, which are examined in this chapter in comparison to the monolithic and active fiber bimorphs. Testing reveals that MFC bimorphs perform the best at lower frequencies in comparison to the other two, but the power output virtually drops to nothing at higher frequencies. The chapter concludes by analyzing a novel new approach to harvest energy from human walking by using a device known as a "mobile energy harvester", or MEH. The MEH is constructed using two Piezo Systems bimorphs mounted in a cantilever configuration and wired in parallel to increase the overall current output and lower the optimal load resistance. Experimental results verify that the harvester is capable of partially recharging a very small, 3.0 volt, 7 mAh lithium ion battery. Further testing reveals that an optimal load capacitance can be determined by specifying the window of time in which the MEH operates.

Chapter 4 explores a basic electrical model of a thermoelectric generator (TEG) as a voltage source in series with an internal resistance. The model shows that the voltage output should increase linearly with an increasing temperature difference and the power should therefore increase quadratically. A functional generator is constructed using four commercially available thermoelectric generators from Melcor ® and a large aluminum heat sink to dissipate heat from the cold side. Several experiments are performed to verify the linear relationship between the voltage output and temperature gradient, and then the device is attached to the outside of an automotive exhaust system to determine the feasibility of battery recharging. Testing confirmed a maximum power output of 198.4 mW during idling and 316 mW during road testing and verified that both an 80 and 300 mAh battery were recharged from the thermal gradients. Because of the low voltage output of thermoelectric generator, the latter half of the chapter explores the possibility of stepping up the voltage output either through a switching circuit or a DC/DC converter. The switching circuit concept involves charging three nickel metal hydride batteries in parallel up to 1.5 volts and then switching to a series configuration to produce a 4.5 volt output. The DC/DC converter steps up any TEG voltage output greater than 1.2 volts up to about 4.82 volts. The chapter concludes by comparing the two voltage amplification

methods, noting that the switching circuit is beneficial in theory, but hard to implement in real life applications, as the circuit only senses the voltage and not the state of charge of the battery. However, when lithium ion batteries are not a charging option, then the switching circuit in tandem with nickel metal hydride batteries would be advantageous over the DC/DC converter.

Chapter 5 examines two well established electrical models for photovoltaic and electromagnetic transducers, and presents a table of an overall comparison of energy density per square centimeter of surface area. A second table of experimental results during the course of preparing this thesis shows good agreement with the first table, adding to its validity. The chapter proceeds with experimental results from a hybrid energy harvester based on both electromagnetic and piezoelectric transducers. The concept arises from the fact that the proof mass often used for piezoelectric harvesters is typically a useless mass. The hybrid device introduced would replace the proof mass with a permanent magnet. Together, both systems can harvest a maximum of 154.9 μW under optimal conditions, which represents an increase of 137.2% over the electromagnetic harvester alone and 183.8% over the piezoelectric harvester alone.

6.2 Contributions

Much of the present research in energy harvesting has focused on improved rectifying and conditioning circuits to maximize the power output of piezoelectric devices. What has been lacking is an investigation into the basic storage devices, specifically in comparison to one another. This research has shown that while batteries have higher energy density than supercapacitors, they are not always an attractive alternative to energy storage since their minimum charge current requirements prohibit their recharging at a reasonable rate. Such information is crucial for designing practical energy harvesting devices that function in real world situations.

While piezoelectric bimorphs have been studied extensively, new materials such as active fiber composites and macro fiber composites which utilize the d_{31} coefficient have yet to be examined for their power harvesting capabilities. This research serves as an introduction to a basic comparison of the different types of materials and their

harvesting capabilities in relation to one another and to a standard monolithic bimorph that has commonly been used in literature for piezoceramic bimorph characterization. Furthermore, this research presents the first piezoelectric energy harvesting device that links two bimorphs together in parallel to increase current output and lower the optimal load resistance, the mobile energy harvester (MEH). The device uses a minimal parasitic harvesting approach to generate energy from vibrations experienced at the waist level of a walking human subject. Such a device was able to recharge a small battery and several capacitors, demonstrating its usefulness for harvesting applications.

Likewise, thermoelectric generators (TEGs) have been researched for several decades, but recent advancements of TEGs capable of operating in lower temperature regimes (20 – 200 ^{o}C) has spurred interest in their use for energy harvesting using smaller thermal gradients. The research presented here proposes a novel new concept of using thermal gradients from automobile exhaust for battery recharging. Previously classified as "waste heat", the thermal energy present in the exhaust gases of an internal combustion engine can be harvested to reclaim energy that is typically wasted through dissipation into the environment. However, TEGs operating at such low gradients do not generate a very high voltage output, so two methods of stepping up the voltage are presented. The first, a switching circuit for use in charging batteries, is a novel concept for stepping up the voltage output through varying the configuration of the rechargeable batteries. The second, a DC/DC converter, is not as novel, although recent improvements in efficiency and lower input voltage requirements make them attractive for use with TEGs. While the results show that the DC/DC is advantageous, research into both methods is essential to further the advancement of small scale and small thermal gradient harvesting devices.

To the contribution of energy density comparison values, the experiments performed for harvesting studies in previous chapters proves to fall within the range of numerical values found in literature, providing further validation of such numbers. For the advancement of research into hybrid or multiple energy domain harvesting, theoretical calculations performed indicate that the proof mass currently used for piezoelectric harvesters, which increases strain at the expense of added weight, could be replaced with commercially available permanent magnets to harvest further energy from

the vibrations through electromagnetic means. Such a device would harvest energy on the same order of magnitude from both transducer methods, effectively increasing the overall power density of the harvesting device.

6.3 Future Work

Portable electronic devices and wireless sensors have shrunk in size to unprecedented levels, but the batteries or capacitors that supply power still dominate the bulk of the device size. Therefore, it is crucial to better understand how to store energy from harvesting devices in the most efficient manner possible. Future work should look at storing energy in improved supercapacitor designs and in thin film lithium ion batteries, which have much smaller size ratings as low as 4.0 volts, 0.7 mAh and therefore would be more compatible with the smaller current output of piezoelectric devices.

Likewise, methods of increasing the current output of piezoelectric harvesters are important. The research presented shows that the current output can be increased by connecting piezoelectric devices in parallel, but further research is needed to understand the effects of out of phase vibration and different input amplitudes for such devices. Additionally, future work should involve shrinking the overall size of devices such as the mobile energy harvester and studying the physiology of the human gait to possibly improve the mounting location of the harvester to maximize the harvested energy. In terms of multiple bimorph harvesting, it would be beneficial to research the effects of out of phase and unequal frequency vibration effects on the power output of piezoelectric harvesters containing multiple bimorphs.

While the concept of recharging batteries using energy harvested from thermal gradients available from automobile exhaust has been proven to be feasible, further research should be performed to optimize the location and size of the thermoelectric device used. With better interface with the source heat and integration with existing electronics on the car, it may be possible to generate enough energy to replace the conventional alternator, increasing the power output of the engine to other systems.

The greatest opportunity for future work lies in the development of multiple energy domain harvesters, or hybrid harvesters. Issues such as the interface between multiple power sources must be addressed, as well as energy storage devices to accommodate varying power inputs. Furthermore, methods to shrink such a hybrid device down to a portable level should be investigated, or possibly a method of incorporating it with the mobile energy harvester proposed in Chapter 3.

Bibliography

[1] http://www.advancedcerametrics.com/files/File/articles/ACIs_Fiber_Technology.pdf

[2] http://www.advancedphotonix.com/ap_products/pdfs/PDV-P7002.pdf

[3] http://www.digibattery.com/

[4] http://www.infinitepowersolutions.com/

[5] http://www.kjmagnetics.com/

[6] http://www.nimh-direct.co.uk/site/Cell%20chemistry/battery_primer.asp

[7] http://www.piezo.com/tech4history.html

[8] http://www.smart-material.com/Smart-choice.php?from=Products

[9] Allen, J. and Smits, A. "Energy Harvesting Eel," *Journal of Fluids and Structures*, Vol. 15, pp. 629-40, 2001.

[10] Anton, S. and Sodano, H., "A Review of Power Harvesting Using Piezoelectric Materials (2003-2006)," *Smart Materials and Structures,* 2007 (in press).

[11] Blatt, F. J., Schroeder, P. A., Foiles, C. L. and Greig, D. Thermoelectric Power of Materials. Plenum Press: New York, 1976.

[12] Blevins, R. D. Formulas for Natural Frerquency and Mode Shape. Robert E. Krieger Publishing Company: New York, 1979.

[13] Bottner, H., Chen, G. and Venkatasubramanian, R., "Aspects of Thin-Film Superlattice Thermoelectric Materials, Devices, and Applications," *MRS Bulletin-Materials Research Society*, Vol. 31, No. 3, pp. 199-205, 2006.

[14] Castaner, L. and Silvestre, S. Modelling Photovoltaic Systems using PSPICE. John Wiley & Sons: Hoboken, NJ, 2002.

[15] Catchpole, K. R. and Green, M. A. "Third generation photovoltaics," *2002 Conference on Optoelectronic and Microelectronic Materials and Devices,* pp. 59-64, 2002.

[16] Chou, P. H., Li, D. and Kim, S. "Maximizing Efficiency of Solar-Powered Systems by Load Matching," *ISLPED*, August 9-11, 2004.

[17] Cope, R. C. and Podrazhansky, Y. "The art of battery charging," *IEEE, Fourteenth Annual Battery Conference on Applications and Advances*, January 12-15, 1999, pp. 233-235.

[18] Damaschke, J. M., "Design of a Low-Input voltage converter for thermoelectric generator," *IEEE Transactions on Industry Applications,* Vol. 33, Issue 5, pp. 1203-1207, Sept/Oct 1997.

[19] Damaschke, J. M., "Design of a low-input-voltage converter for Thermoelectric Generator," *IEEE Transactions on Industry Applications*, Vol. 33, Issue 5, pp. 1203-1207, Sep/Oct 1997.

[20] Davis, S. "Basics of Design: Battery Power Management," Supplement to *Electronic Design*, June 7, 2004.

[21] Deeley, P. M. Electrolytic capacitors. Recorder Press: Plainfield, New Jersey, 1938.

[22] Dell, R.M. and Rand, D. A. J. Understanding Batteries. Royal Society of Chemistry: Cambridge, 2001.

[23] Douseki, T., Yoshida, Y., Utsunomiya, F., Itoh, N. and Hama, N. "A Batteryless Wireless System Uses Ambient Heat with a Reversible-Power-Source Compatible CMOS/SOI DC-DC Converter," *IEEE International Solid-State Circuits Conference*, Session 22, Paper 22.2, 2003.

[24] Dudney, N. J. "Solid-state thin-film rechargeable batteries," *Materials Science and Engineering B,* 116 (2005), pp. 245-249.

[25] Dudney, N. J. and Jang, Y. I. "Analysis of thin-film lithium batteries with cathodes of 50 nm to 4 μm thick $LiCoO_2$," *J. Power Sources*, 119-121, pp. 300-304, 2003.

[26] duToit, N. and Wardle, B., "Experimental Verification of Models for Microfabricated Piezoelectric Energy Harvesters," *Proceedings of 47th AIAA/ASME/ASCE/AHS/ASC Structures, Structural Dynamics, and Materials Conference*, Newport, RI, May 2006.

[27] El-hami, M., Jones, P. G., James, E., Beeby, S. P., White, N. M., Brown, A. D. and Hill, M., "Design and fabrication of a new vibration based electromechanical generator," *Sensors and Actuators*, A, 92, pp. 335-342, 2001.

[28] Elvin, N. G., Elvin, A. A. and Spector, M. "A Self-powered Mechanical Strain Energy Sensor," *Smart Materials and Structures*, Vol. 10, pp. 293-299, 2001.

[29] Elliot, R. S. Electromagnetics: History, Theory, and Applications. IEEE Press: Piscataway, 1993.

[30] Erturk, A. and Inman, D. J. "Mechanical Considerations for Modeling of Vibration-Based Energy Harvesters," (To be published in the) *Proceedings of the ASME 2007 IDETC/CIE 2007,* Sept. 4-7, Las Vegas, Nevada, 2007.

[31] Gautschi, G. Piezoelectric Sensorics. Springer-Verlag: Berlin Heidelberg, 2002.

[32] Goldfarb, M. and Lowell, D.J. "On the Efficiency of Electric Power Generation With Piezoelectric Ceramic," *Journal of Dynamic Systems, Measurement, and Control*, September 1999, Vol. 121, pp. 566-571.

[33] Halper, M. S. and Ellenbogen, J. C. "Supercapacitors: A Brief Overview," MITRE, McLean, Virginia, March 2006.

[34] Hambley, A. R. Electronics (2nd Edition). Prentice Hall: Saddle River, NJ, 1999.

[35] Hausler, E. and Stein, E., 1984. "Implantable Physiological Power Supply with PVDF Film," *Ferroelectrics*, Vol. 60, 277-282.

[36] IEEE Standard, IEEE Standards on Piezoelectricity, ANSI/IEEE Standard, The Institude of Electrical and Electronic Engineers, New York, 1988.

[37] Inman, D. J. Engineering Vibration, Second Edition. Prentice-Hall, 2001.

[38] Jansen, A. J. and Stevels, A. L. N. "Human Power, a Sustainable Option for Electronics," *Proc. of IEEE Int. Symposium on Electronics and the Environment*, pp. 215-218, 1999.

[39] Kiehne, H. A. Battery Technology Handbook. Marcel Dekker: New York, 2003.

[40] Kiely, J. J., Morgan, D. V. and Rowe, D. M., "Low cost miniature thermoelectric generator," *Electronics Letters*, 27, pp. 2332-2334, 1991.

[41] Kimura, M, 1998, "Piezoelectric Generation Device," US Patent Number 5,801,475.

[42] Kingman, R., Rowland, C. and Popescu, S. "An experimental observation of Faraday's law of induction," *American Journal of Physics,* Vol 70, pp. 595-598, June 2002.

[43] Kymissis, J., Kendall, C., Paradiso, J. and Gershenfeld, N., "Parasitic Power Harvesting in Shoes," *Proceedings of the Second IEEE International Conference on Wearable Computing, (ISWC)*, IEEE Computer Society Press, October 1998, pp. 132-139.

[44] Kymissis, J., Kendall, C., Paradiso, J. and Gershenfeld, N., "Parasitic Power Harvesting in Shoes," *Proceedings of the Second IEEE International Conference on Wearable Computing, (ISWC)*, IEEE Computer Society Press, October 1998, pp. 132-139.

[45] Lee, J. B., Chen, Z., Allen, M. G., Rohatgi, A. and Arya, R. "A Miniaturized High-Voltage Solar Cell Array as an Electrostatic MEMS Power Supply," *Journal of Microelectromechanical Systems*, Vol 4, No 3, pp. 102-108, 1995.

[46] Lesieutre, G. A., Ottman, G. K. and Hofmann, H. F., 2004. "Damping as a result of piezoelectric energy harvesting," *Journal of Sound and Vibration,* Vol. 269**,** 991-1001.

[47] Linden, D. and Reddy, T. B. Handbook of Batteries. McGraw-Hill Professional: New York, 2002.

[48] Mah, O. "Fundamentals of Photovoltaic Materials," National Solar Power Research Institute, Inc., 1998.

[49] Meninger, S., Mur-Miranda, J. O., Amirtharajah, R., Chandrakasan, A. and Lang, J. H., "Vibration-to-Electric Energy Conversion," *IEEE Transactions on Very Large Scale Integration (VLSI) Systems, Vol. 9, Issue 1, pp. 64-76, 2001*.

[50] Myers, R. L. The Basics of Physics. Greenwood Press: Westport, Conn., 2006.

[51] Nazri, G. and Pistoia, G. Lithium Batteries: Science and Technology. Kluwer Academic Publishers: Boston, 2004.

[52] Nelson, J. Physics of Solar Cells. Imperial College Press: London, 2003.

[53] Ng, T. H. and Liao, W. H., "Sensitivity Analysis and Energy Harvesting for a Self-Powered Piezoelectric Sensor," *Journal of Intelligent Material Systems and Structures*, Vol. 16, No. 10, pp. 785-797, 2005.

[54] Nolas, G. S., Poon, J. and Kanatzidis, M., "Recent Developments in Bulk Thermoelectric Materials," *MRS Bulletin- Materials Research Society*, Vol. 31, No. 3, pp. 199-205, 2006.

[55] Nolas, G. S., Sharp, J. and Goldsmid, H. J. Thermoelectrics: Basic Principles and New Materials Developments. Springer: New York, 2001.

[56] Nolas, G. S., Sharp, J. and Goldsmid, H. J. Thermoelectrics: Basic Principles and New Material Developments. Springer-Verlag: Berlin, 2001.

[57] Ottman G K, Hofmann H F and Lesieutre G A 2002 Optimized piezoelectric energy harvesting circuit using step-down converter in discontinuous conduction mode *Proc. of IEEE's 33rd Annual Power Electronics Specialists Conf. (Cairns, Queensland, Australia, June 23-27)* **4** 1988-94.

[58] Ramsay, M. J. and Clark, W. W. "Piezoelectric Energy Harvesting for Bio MEMS Applications," *Proceedings of the SPIE 8th Annual Smart Materials and Structures Conference*, Newport Beach, CA, Vol. 4332-2001, pp. 429-438, 2001.

[59] Raghunathan, V., Kansal, A., Hsu, J., Friedman, J. and Srivastava, M., "Design Considerations for Solar Energy Harvesting Wireless Embedded Systems," *IEEE International Conference on Information Processing in Sensor Networks*, Los Angeles, CA, No. 64, April 2005.

[60] Rizzoni, G. Principles and Applications of Electrical Engineering (Third Edition). McGraw-Hill: Boston, MA 2000.

[61] Rome, L. C., Flynn, L., Goldmann, E. M. and Yoo, T. D. "Generating electricity while walking with loads." *Science,* September 2005, Vol 309:1725-1728.

[62] Rothwell, Edward and Cloud, Michael. Electromagnetics. CRC Press: Boca Raton, 2001.

[63] Roundy, S., Wright, P. K., and Rabaey, J. M. Energy Scavenging for Wireless Sensor Networks. Kluwer Academic Publishers: Norwell, 2004.

[64] Rowe, D.M. CRC Handbook of Thermoelectrics. CRC Press: Boca Raton, 1994.

[65] Sasaki, K., Osaki, Y., Okazaki, J., Hosaka, H. and Itao, K. "Vibration-based automatic power-generation system," *Microsyst Technol*, pp. 965-969, 2005.

[66] Schmidt, V.H. "Piezoelectric Energy Conversion in Windmills," *Ultrasonics Symposium*, vol. 2, pp. 897-904, October 1992.

[67] Sodano, H. A., Park, G. and Inman, D. J., "A review of power harvesting using piezoelectric materials," *Shock and Vibration Digest, Vol.* **36,** pp. 197-206, 2004.

[68] Sodano, H.A., Park, G. and Inman, D.J., 2005b, "Comparison of Piezoelectric Energy Harvesting Devices," Journal of Intelligent Material Systems and Structures, 16(10): 799-807.

[69] Sodano H A, Park G and Inman D J 2004c Estimation of electric charge output for piezoelectric energy harvesting *Strain* 40 49-58.

[70] Sodano, H. A. *Macro-fiber composite Thesis for Sensing, Actuation, and Power Generation*. Master's Thesis, Virginia Tech, 2003.

[71] Sodano, H. A., Simmers, G. E., Dereux, R. and Inman, D. J., "Recharging Batteries using Energy Harvested from Thermal Gradients," *Journal of Intelligent Material Systems and Structures*, Vol. 18, pp. 3-10, January 2007.

[72] Sodano, H. A., Park, G., Leo, D. J. and Inman, D. J. "Use of piezoelectric energy harvesting devices for charging batteries. Proceedings of SPIE, 2003, Vol. 5050, pp. 101 – 108.

[73] Sorrell, C. C., Sugihara, S. and Nowotny, J. Materials for energy conversion devices. CRC Press: Boca Raton, FL, 2005.

[74] Stark, I. and Stordeur, M. "New Micro Thermoelectric Devices Based on Bismuth Telluride-Type Thin Solid Films," *18th International Conference on Thermoelectrics*, pp. 465-472, 1999.

[75] Starner, T. "Human-powered Wearable Computing," *IBM Systems Journal*, Vol. 36, Nos. 3 & 4, pp. 618-629, 1996.

[76] Starner, T., Paradiso, J.A., "Human Generated Power for Mobile Electronics," in Piguet, C. (ed), Low power Electronics, CRC Press, 2004, Chapter 45, pp. 45-1 – 45-35.

[77] Starner, T., Paradiso, J.A., "Human Generated Power for Mobile Electronics," in Piguet, C. (ed), Low power Electronics, CRC Press, 2004, Chapter 45, pp. 45-1 – 45-35.

[78] Stephens, N. G. 2006, "On energy harvesting from ambient vibration," *Journal of Sound and Vibration,* **293**, 409-25.

[79] Sterken, T., Baert, K., Puers, R. and Borghs, S. "Power Extraction from Ambient Vibration," *Proceedings of SeSens (Workshop on Semiconductor Sensors)*, 2002, November 29: Veldhoven, the Netherlands, pp. 680-683.

[80] Stordeur, M. and Stark, I. "Low power Thermoelectric Generator – Self-sufficient Energy Supply for Micro Systems," *16th International Conference on Thermoelectrics*, pp. 575-577, 1997.

[81] Torres, E. O. and Rincon-Mora, G. A., "Long Lasting, Self-Sustaining, and Energy-Harvesting System-in-Package (SiP) Wireless Micro-Sensor Solution," *Intl. Conf. on Energy, Environment, and Disasters (INCEED)*, Charlotte, NC, July 2005.

[82] Umeda, M, Nakamura, K. and Ueha, S. "Analysis of the Transformation of Mechanical Impact Energy to Electric Energy Using Piezoelectric Vibrator," *Japan Journal of Applied Physics*, Volume 35, Part 1, No. 5B, pp. 3267-3273, May 1996.

[83] Umeda, M., Nakamura, K. and Ueha, S. "Energy Storage Characteristics of a Piezo-generator Using Impact Vibration," *Japan Journal of Applied Physics,* Vol. 36, Part 1, No. 5B, pp. 3146-3151, May 1997.

[84] Voigt, T., Ritter, H. and Schiller, J., "Utilizing Solar Power in Wireless Sensor Networks," *Proceedings of the 28th Annual IEEE International Conference on Local Computer Networks*, Issue 20-24, pp. 416-422, Oct. 2003.

[85] Wang, Q. M. and Cross, L. E. "Performance analysis of piezoelectric cantilever bending actuators," *Ferroelectrics*, 1998, Vol 215, pp 187-213.

[86] Wang, H., Porter, W. D. and Sharp, J., "Thermal Conductivity Measurements of Bulk Thermoelectric Materials," *24th International Conference on Thermoelectrics*, pp. 91-94, June 2005.

[87] Williams, C. B. and Yates, R. B., 1995, "Analysis of a micro-electric generator for Microsystems," *Transducers 95/Eurosensors IX,* pp. 369-72.

[88] Wu, C. "Analysis of Waste-Heat Thermoelectric Power Generators," *Applied Thermal Engineering*, Vol. 16, No 1., pp. 63-69, 1996.

[89] Yang, J. and Caillat, T., "Thermoelectric Materials for Space and Automotive Power Generation," *MRS Bulletin- Materials Research Society*, Vol. 31, No. 3, pp. 199-205, 2006.

[90] Zhang, C., Najafi, C., Bernal, L. P. and Washabaugh, P., "An integrated combustor-thermoelectric micro power generator," *Twelfth IEEE Int. Conf. On Solid-State Sensors and Actuators (Trandsucers '01)*, Munich, Germany, June 2001.

Vita

Justin Farmer was born on May 19, 1981 to Bill and Rita Farmer in Salem, Virginia. In 1999, Justin graduated from Salem High School with an International Baccalaureate Diploma. That fall, he began his undergraduate studies at Virginia Tech.

In January of 2001, he began an internship with Norfolk Southern in Roanoke, Virginia which lasted through May. He then resumed his studies at Virginia Tech in the summer and decided to pursue a bachelor's degree in Mechanical Engineering. Concurrently, in June of 2001, he began an internship with Luna Innovations in Blacksburg, Virginia, which he held until he completed his B.S. in the spring of 2004.

Early in the first semester of his senior year, in the fall of 2003, Justin's father was diagnosed with multiple myeloma, a rare blood cancer of the plasma cells. Unsure of what to do after graduating, his father and coworkers at Luna convinced him to pursue his Masters degree. In the fall of 2004, under the supervision of Dr. Daniel Inman, he began coursework and research towards a Masters degree in Mechanical Engineering. Initially working with David Neal on the morphing wing project, a research position in the field of power harvesting led Justin to focus his thesis research on that topic. Following his father's death in early November of 2005, Justin withdrew from school for the rest of the semester to help his mother with legal and financial matters. In the spring of 2006, he resumed his coursework and research and completed his thesis in May 2007.

Permanent Address:

1115 Cape Ann Court

Salem, VA 24153